

Charge Order in $\text{Ir}_{1-x}\text{Pt}_x\text{Te}_2$ and High-Energy Magnetic Excitations in $\text{La}_{2-x}\text{Sr}_x\text{CuO}_4$

Dissertation

zur

Erlangung der naturwissenschaftlichen Doktorwürde
(Dr. sc. nat.)

vorgelegt der

Mathematisch-naturwissenschaftlichen Fakultät

der

Universität Zürich

von

Oleh Ivashko

aus

der Ukraine

Promotionskommission

Prof. Dr. Johan Chang (Vorsitz)

Dr. Benoît Fauqué

Prof. Dr. Christof Aegerter

Zürich, 2018

Abstract

This thesis is based on synchrotron-based experiments on two different systems: $\text{Ir}_{1-x}\text{Pt}_x\text{Te}_2$ and $\text{La}_{2-x}\text{Sr}_x\text{CuO}_4$. Both hard x-ray diffraction (XRD) and resonant inelastic x-ray scattering (RIXS) techniques were adopted to study charge order superstructure reflections and magnetic (and charge) excitations respectively.

The evolution of charge order in $\text{Ir}_{1-x}\text{Pt}_x\text{Te}_2$ has been tracked as a function of doping and hydrostatic pressure. A previous resistivity study of $x = 0.05$ sample evidenced a suppression of superconductivity upon application of pressure. It was found that this suppression is directly related to the appearance of charge order, which is preempted by the structural transition. This allows us to conclude that a prerequisite for the charge order in $\text{Ir}_{1-x}\text{Pt}_x\text{Te}_2$ system is the structural transition from hexagonal to monoclinic symmetries. Furthermore, a model for the interplay between the charge order and superconductivity is proposed.

In $\text{La}_{2-x}\text{Sr}_x\text{CuO}_4$ systems high-energy magnetic excitations were studied by means of resonant inelastic x-ray scattering. The experiments were performed both on the bulk $x = 0.12$ compound and on thin films of La_2CuO_4 grown on several substrates. The $\text{La}_{2-x}\text{Sr}_x\text{CuO}_4$ with $x = 0.12$ sample evidenced a strong anisotropy of the spin excitations along the Brillouin zone. A fit to the magnetic-excitation dispersion, by means of a Hubbard model at strong coupling, concluded to a ratio of $-t'/t \approx 0.4$. This is in strong contrast with the angle resolved photoemission study evidenced $-t'/t = 0.15$. To account for this discrepancy, a two-band model is considered, where in addition to the $d_{x^2-y^2}$ also the d_{z^2} band is taken into account. Since the hybridization between these two bands is directly related to the structural parameters, thin films of La_2CuO_4 were grown epitaxially on several substrates, resulting in different strain values. As a consequence, the in-plane compressive sample presents a stronger anisotropy of the magnon dispersion and a bigger on-site Coulomb interaction U , with respect to the most tensile sample. By fitting the dispersion, with the Hubbard model, higher values of hopping integral t and antiferromagnetic exchange interaction J_{eff} are obtained for the compressive sample. In view of these discoveries, a projection on the optimally doped system is made.

Contents

Abstract	iii
1 Introduction	1
2 Experimental Methodology	9
2.1 Sample Preparation	9
2.2 Hard X-ray Diffraction	11
2.2.1 Pressure Cell	12
2.3 Resonant Inelastic X-ray Scattering	12
2.3.1 RIXS on Cuprates	15
3 Theoretical Background	17
3.1 XRD Structure Factor	17
3.2 RIXS Cross Section	18
3.3 Hubbard Model	20
4 Charge Order & Superconductivity in $\text{Ir}_{1-x}\text{Pt}_x\text{Te}_2$	25
4.1 State of the Art	26
4.2 Resistivity Measurements	27
4.3 Hard X-ray Scattering Experiment	29
4.4 Discussion & Conclusions	32
5 Damped Spin Excitations in $\text{La}_{2-x}\text{Sr}_x\text{CuO}_4$	37
5.1 State of the Art	38
5.2 Results: Paramagnons in $\text{La}_{2-x}\text{Sr}_x\text{CuO}_4$	43
5.3 Discussion & Conclusions	47
6 Magnetic & Charge Excitations in La_2CuO_4 Thin Films	53
6.1 RIXS Study of La_2CuO_4 Thin Films	55
6.2 Discussion & Conclusions	62
7 Conclusions	67

A XRD Studies of $\text{Pr}_4\text{Fe}_2\text{As}_2\text{Te}_{0.88}\text{O}_4$	69
Bibliography	73
List of Publications	85
Acknowledgements	89
Curriculum Vitae	91

List of Figures

1.1	Schematic representations of the crystal structure of TMDCs	2
1.2	Crystal structure and phase diagram of BaFe_2As_2	3
1.3	T_c as a function of lattice parameters in Fe-based compounds	4
1.4	Low-energy ($\pi\pi$) spin excitations in $\text{BaFe}_{2-x}\text{Co}_x\text{As}_2$ and $\text{La}_{2-x}\text{Sr}_x\text{CuO}_4$.	5
1.5	Stripe order in nickelates and cuprates	6
1.6	Charge-transfer and Mott insulating ground state	7
2.1	Laue diffraction pattern for $\text{La}_{2-x}\text{Sr}_x\text{CuO}_4$ with $x = 0.12$ and $\text{Ir}_{1-x}\text{Pt}_x\text{Te}_2$ with $x = 0.05$ samples.	10
2.2	Pressure cell and pressure calibration	11
2.3	RIXS endstation at SLS and resolution improvements at Cu L_3 edge . . .	13
2.4	Schematic representation of RIXS process	14
2.5	Excitations in cuprates observable by RIXS	15
2.6	RIXS spectra for $\text{La}_{2-x}\text{Sr}_x\text{CuO}_4$ system	16
3.1	Phase diagram of metal-insulator transition as a function of filling	21
3.2	Analytical <i>vs.</i> approximated solutions for zone-boundary dispersion E_{ZB} .	22
4.1	Crystal structure of IrTe_2	26
4.2	Phase diagram of Pt and Pd substituted IrTe_2	27
4.3	Resistivity measurements of $\text{Ir}_{1-x}\text{Pt}_x\text{Te}_2$	28
4.4	Hard x-ray diffraction measurements of $\text{Ir}_{1-x}\text{Pt}_x\text{Te}_2$	30
4.5	Charge-order model for $\text{Ir}_{1-x}\text{Pt}_x\text{Te}_2$	31
4.6	Proposed p <i>vs.</i> T <i>vs.</i> x phase diagram for $\text{Ir}_{1-x}\text{Pt}_x\text{Te}_2$	33
4.7	Resistivity curves, as a function of hydrostatic pressure, of $\text{Ir}_{1-x}\text{Pt}_x\text{Te}_2$ with $x = 0.05$	34
5.1	T_c as a function of discovery year for several superconducting compounds	38
5.2	Cuprates phase diagram	39
5.3	ARPES Fermi surface of $\text{La}_{2-x}\text{Sr}_x\text{CuO}_4$	40
5.4	Magnetic-excitation dispersion in cuprates	42
5.5	Color maps of intensity of RIXS spectra of $\text{La}_{2-x}\text{Sr}_x\text{CuO}_4$ with $x = 0.12$.	43
5.6	Raw RIXS spectra of $\text{La}_{2-x}\text{Sr}_x\text{CuO}_4$ with $x = 0.12$	45

5.7	Magnetic-excitation dispersion for $\text{La}_{2-x}\text{Sr}_x\text{CuO}_4$ with $x = 0.12$	46
5.8	Magnetic-excitation dispersion for $\text{Bi}_2\text{Sr}_{0.99}\text{La}_{1.1}\text{CuO}_{4+\delta}$	47
5.9	Measured <i>vs.</i> predicted zone-boundary dispersions	48
5.10	<i>dd</i> excitations for La_2CuO_4 and $\text{La}_{2-x}\text{Sr}_x\text{CuO}_4$ with $x = 0.12$	49
5.11	DFT for $\text{La}_{2-x}\text{Sr}_x\text{CuO}_4$ system	50
6.1	Antiferromagnetism and spin fluctuations <i>vs.</i> T_c for several compounds . .	54
6.2	T_c as a function of pressure in cuprates	55
6.3	X-ray diffraction patterns of La_2CuO_4 thin films	56
6.4	XAS and RIXS spectra of La_2CuO_4 thin films	57
6.5	Magnetic-excitation dispersion of LCO/STO and LCO/LSAO	58
6.6	Magnetic-excitation dispersion of LCO/LSAO, LCO/NGO and LCO/LSAT	60
6.7	Experimental and theoretical parameters for La_2CuO_4 thin films	61
6.8	DFT of the oxygen <i>p</i> bands as a function of strain	62
6.9	Normalized magnetic-excitation dispersion of thin films	63
A.1	Crystal structure of $\text{Pr}_4\text{Fe}_2\text{As}_2\text{Te}_{0.88}\text{O}_4$	70
A.2	Characteristic temperature scales of $\text{Pr}_4\text{Fe}_2\text{As}_2\text{Te}_{0.88}\text{O}_4$	71

List of Tables

5.1	Fit parameters for the magnetic-excitation dispersion of LCO, LSCO with $x = 0.12$ and Bi2201	46
6.1	Thickness and lattice parameters of $\text{La}_{2-x}\text{Sr}_x\text{CuO}_4$ thin films	56
6.2	Fit and theoretical parameters for the magnetic-excitation dispersion of La_2CuO_4 thin films	59
6.3	Lattice parameters and T_c for optimally doped $\text{La}_{2-x}\text{Sr}_x\text{CuO}_4$ thin films grown on several substrates	64

Chapter 1

Introduction

Unconventional superconductivity presents one of the great challenges in modern condensed matter physics [1]. It was discovered in many systems like in organic materials [2], cuprates [3], heavy fermions [4] and pnictides [5]. For each of the different systems, several pairing mechanisms were proposed but, to date, no general consensus has been obtained. Furthermore, these superconducting compounds, present rich phase diagrams, where competing orders occur. Recently, superconductivity was observed in “magic-angle” twisted graphene [6]. As a function electrostatic doping two superconducting domes, on both sides of a Mott insulating phase, are obtained and a metallic state is present outside of these regions. As we will see later, this resembles the electron- and hole-doped phase diagram of cuprates, although this material has a hexagonal structural symmetry like the transition-metal dichalcogenides (TMDC). Here, a brief introduction on different layered systems is provided with comparison to the $\text{Ir}_{1-x}\text{Pt}_x\text{Te}_2$ and $\text{La}_{2-x}\text{Sr}_x\text{CuO}_4$ systems studied in this thesis.

Let us start with TMDCs, which attracted a considerable attention in the last years due to their robustness and interesting fundamental physics like superconductivity (SC) and charge density wave (CDW) [7]. The structure of these materials is formed by a transition-metal in between two chalcogen atomic planes. This structure is then repeated in a layered manner as shown in Fig. 1.1. Depending on the stacking, one can obtain a trigonal prismatic ($2H$) or an octahedral ($1T$) coordination. In the $2H$ phase an ABA (chalcogen-metal-chalcogen) stacking is found, while the $1T$ phase presents an ABC stacking. Some of these materials, present also a distorted octahedral structure denominated by $1T'$ (Fig. 1.1). Even though the $2H$ and $1T$ phases are similar, they present important differences. For example, in the widely studied $2H$ - MoS_2 compound, due to the spin-orbit coupling, a splitting of the valence band is present [8]. The interesting thing is that at the high-symmetry K and K' points, this splitting is

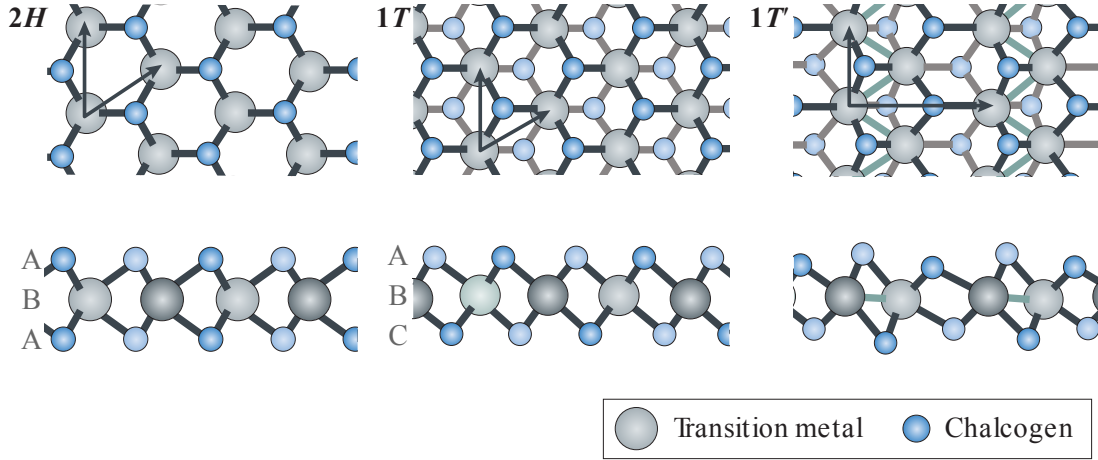


FIGURE 1.1: Schematic representations of the crystal structure of TMDCs. As shown, the trigonal prismatic $2H$ and the octahedral $1T$ phases have an ABA and ABC out-of-plane stacking respectively. The distorted $1T'$ phase is also shown. The arrows in the upper part are the lattice vectors for each system. Adapted from Ref. [7].

characterized by an opposite spin polarization of the bands. On the other hand, the octahedral-coordination compound $1T$ -TaS₂, is peculiar since it can be driven from a CDW to a SC phase by application of hydrostatic pressure [9]. These systems, indeed, present a different interplay between CDW and SC. Besides some exceptions, in the $2H$ phases, generally superconductivity coexists with CDW even at low temperature [7]. In $1T$ systems, instead, the superconductivity emerges once the charge-density-wave is melted by means of pressure or chemical doping.

To describe the formation of CDW in TMDC, a nesting of the Fermi surface, has been proposed. Within this mechanism, parallel sections of the Fermi surface can be connected by a wave vector corresponding to the modulation vector Q_{CDW} of the CDW. However, no clear evidence has been identified with angle-resolved photoemission spectroscopy (ARPES) studies. As regards for superconductivity, which is not exceeding 10 K, it presents interesting characteristics. For example, in IrTe₂ it is observed a competition between the low-temperature structural distorted phase and superconductivity which emerges upon Pt or Pd dopings [10, 11]. This interplay has not been clearly identified. On more general grounds, in TMDCs it is believed that superconductivity persists in a two-dimensional limit. Evidence of Kosterlitz–Thouless type 2D SC was found, for example, in the $2H$ phase of NbSe₂ [12]. As we will see later, the physics of these systems will be relevant in Chapter 4.

Since also a cuprate system is studied in this work, an analogy with the physics of other layered systems is useful. While, cuprates are introduced in more detail in the next Chapters 5 and 6, here a description of the Fe-based superconductors is given. Despite Fe has been thought to be detrimental for superconductivity, because of its localized

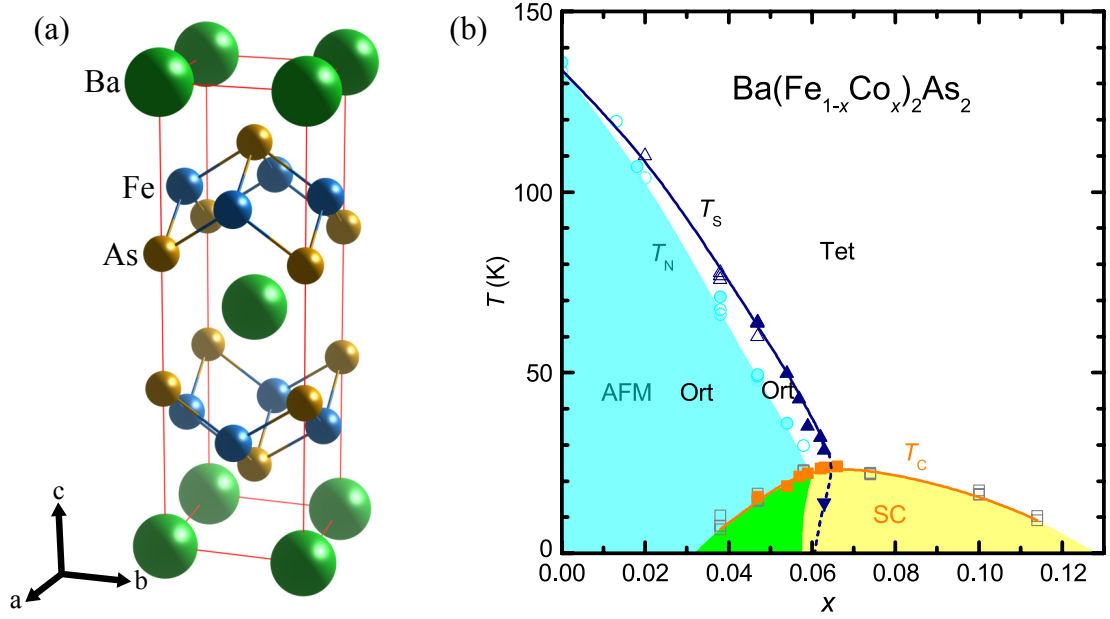


FIGURE 1.2: The unit cell of BaFe₂As₂ is schematically shown in (a). Figure created with *VESTA* [13]. In (b), the phase diagram for Co doped BaFe₂As₂, is illustrated. Both antiferromagnetic (AFM) and superconducting (SC) domes are shown, as much as, the coexistent region (green area). In addition the orthorhombic (Ort) to tetragonal (Tet) structural phase transition is tracked as a function of doping with the characteristic temperature T_s . Adapted from Ref. [14].

magnetic moment, many compounds have been shown to be superconducting [5]. In addition, Fe itself becomes SC with $T_c = 1.8$ K under application of 200 kbar [15]. All these compounds can be grouped in iron pnictides and iron chalcogenides families, having two-dimensional planes of Fe-pnictide/-chalcogenide tetrahedra [see Fig. 1.2(a)]. A further division can be made according to the lattice structure: 1111 as LaFeAsO ($T_c = 10$ K [16]), 122 as BaFe₂As₂ ($T_c = 22$ K with Co doping on Fe site [17]) for which a phase diagram is shown in Fig. 1.2(b), 122* as K_{0.8}Fe₂As₂ ($T_c = 30$ K [18]), 111 as LiFeAs ($T_c = 16$ K [19]), 11 as FeSe ($T_c \approx 8$ K [20]) and 21311 as Sr₂VO₃FeAs ($T_c = 37.2$ K [21]). Recently, a new compound Pr₄Fe₂As₂Te_{0.88}O₄ has joined the family with a 42214 structure (see Appendix A). The crystal structure itself is important since it has a direct impact on the superconducting transition temperature T_c . This is confirmed by the hydrostatic-pressure experiments, which evidenced a significant effect on T_c . Indeed, as can be seen in Fig. 1.3(a), a lower in-plane lattice parameter a is favorable for superconductivity. Another example comes from FeSe that has a $T_c \approx 8 - 13$ K at ambient pressure, which enhances up to 37 K at 70 kbar [22]. An about twofold increase has been observed for LaFeAsO at ~ 120 kbar with $T_c = 21$ K [16]. The related LaFeAsO_{1-x}F_x compound (with $x = 0.11$) shows an increase from 26 to 43 K under 40 kbar of hydrostatic pressure [23]. These remarkable pressure-driven phenomena have led to the conclusion that, the angle α of the Fe-pnictide/-chalcogenide tetrahedra [see Fig. 1.3(b)], as much as the the height of pnictide/chalcogen, are intimately related

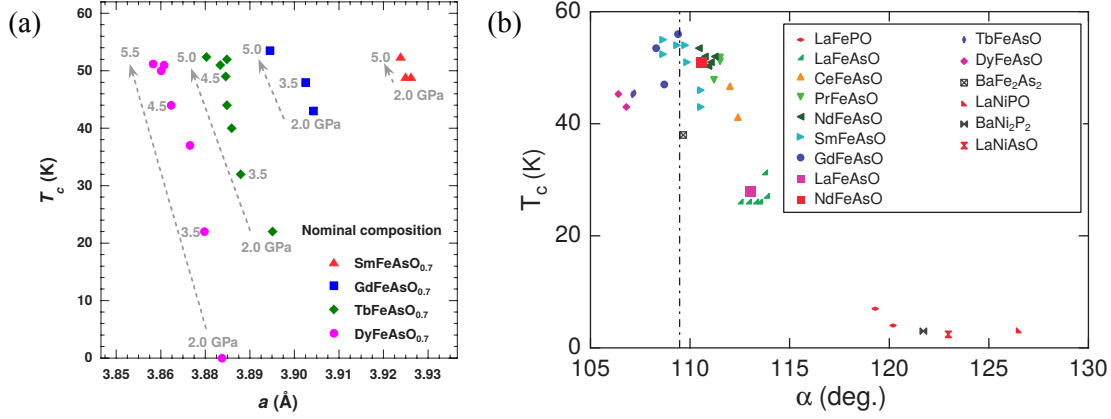


FIGURE 1.3: (a) Superconducting transition temperature T_c , as a function of in-plane lattice parameter a , for hydrostatic pressures and compositions as indicated. Adapted from Ref. [29]. (b) T_c vs. As-Fe-As bond angle α for compounds as indicated in the inset. Vertical dashed line indicates $\alpha = 109.47^\circ$, which is the angle for a regular tetrahedra. Adapted from Ref. [30].

to T_c in the Fe-based superconductors. As can be seen in Fig 1.3, the optimal α for superconductivity, reveals to be close to the undistorted-tetrahedra value of 109.47° . The relevance of the structural parameters is further supported by thin films experiments. Indeed, it was shown that the bulk T_c of FeSe can be enhanced up to 65 K [24], or even 109 K [25], if one unit cell is grown on SrTiO_3 substrate. Consequently, a search for methods optimizing T_c in Fe-based superconductors is of main importance. One of these consists in *chemical pressure*, substituting large atoms with smaller ones. For example, $\text{LaO}_{1-x}\text{F}_x\text{FeAs}$ has a T_c of 26 K, which is enhanced to 43 K by substituting the large La ion with a smaller Sm one [26]. These structural effects on T_c find similarities with the cuprates. In fact, hydrostatic pressure [27] and strain (in thin films) [28] can be used to increase T_c (see Chapter 6 for further detail).

The similarities with cuprates, lay also in the presence of magnetism within the phase diagram [see Fig. 1.2(b)]. Although, Fe-based compounds have significant differences with cuprates. In fact, the first main difference is the absence of an insulating state [5]. Nevertheless, due to the 3d Fe electrons, a magnetic phase is either close to or coexistent with superconductivity [Fig. 1.2(b)]. There are also exceptions, as for LiFeAs and FeSe which have no long-range magnetic order, as a function of doping. Although, in FeSe an enhancement of spin-fluctuations [31] and the appearance of long-range magnetic state [32] is observed upon application of hydrostatic pressures. In 1111 and 122 systems, the spin density wave (SDW) onset temperature coincides (or it is in the vicinity) with the structural transition. In cuprates, on the other hand, the spin density wave is gradually suppressed by the superconductivity in the underdoped region [33]. Even though, a long-range spin order is suppressed in both systems, with inelastic neutron scattering (INS) experiments, a spin-fluctuation resonance and a spin gap has been found

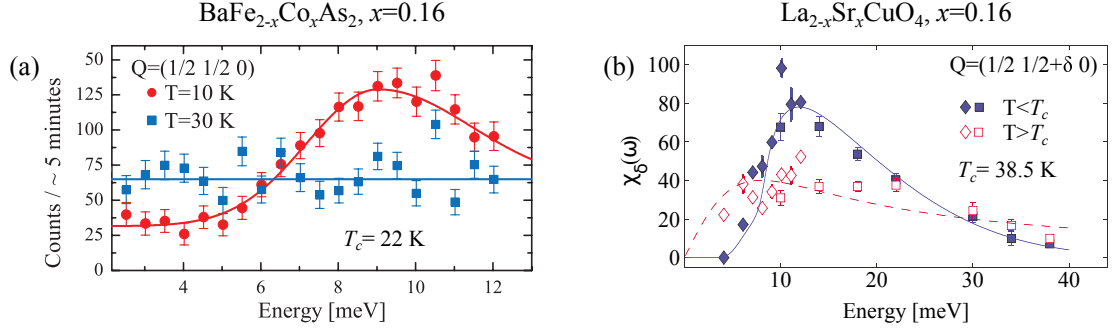


FIGURE 1.4: Low-energy spin excitations at, or in the vicinity of, the antiferromagnetic Brillouin zone center (π, π) , for $\text{BaFe}_{2-x}\text{Co}_x\text{As}_2$ (a) and $\text{La}_{2-x}\text{Sr}_x\text{CuO}_4$ (b). Upon entering in the superconducting regime a gap opens and a resonance appears for both compounds. Adapted from Refs. [34] and [35] respectively.

for $T < T_c$ (see Fig. 1.4), both in several Fe-based and cuprate compounds [5, 33]. Due to this relevance of the Fe^{3+} (Cu^{3+}) magnetic moment, a spin-fluctuation superconducting-pairing mechanism has been proposed [1].

Another comparison between Fe- and Cu-based superconductors can be made with respect to the Fermi surface topology. Several cuprate families have a fairly constant Fermi surface as a function of doping, consisting of Fermi arcs, with strong hole-like $d_{x^2-y^2}$ character, centered around the high-symmetry (π, π) point [36]. On the other hand, a strong variation of the Fermi-surface topology is detected for different Fe-based systems [5]. Systematically, hole and electron pockets are found, and it is thought that the Fermi surface is of main importance for the superconducting properties of these compounds. While for cuprates, a d -wave symmetry of the superconducting gap [37, 38] has found a general agreement, for Fe-based systems there is no common consensus on this topic. It is however agreed that it has “primarily” an s -wave symmetry, but a debate [39, 40] of whether it has an s_{+-} [41] (which is favorable for the spin-fluctuation pairing mechanism) or s_{++} [42] symmetry is still on-going. Although, a pure s -wave symmetry is excluded, due to indications of sign change of the gap [43] (consequent of the presence of both electron and hole pockets), supporting the unconventional nature for superconductivity.

To continue on the relevance of spin excitations in cuprates and to introduce the stripe ordering, an additional analogy comes from the nickelates which have La_2NiO_4 (LNO) as the parent compound. As for La_2CuO_4 , it is possible to dope LNO both by substitution x (as in $\text{La}_{2-x}\text{Sr}_x\text{NiO}_4$) or oxygen intercalation δ ($\text{La}_2\text{NiO}_{4+\delta}$) [33]. At zero doping, LNO is a charge-transfer insulator with a gap of about 4 eV, as evidenced from optical conductivity studies [45]. Upon doping the system with Sr, no metallic state is formed, but only a mid-gap peak is observed. The latter is growing in intensity with increasing doping while remaining at the same energy [45]. Due to the absence of a

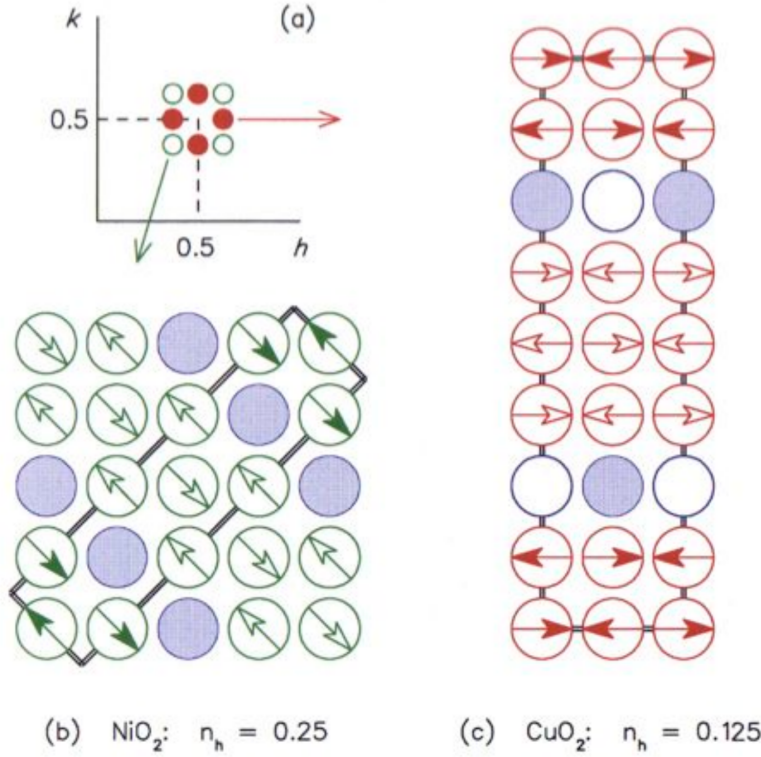


FIGURE 1.5: Schematic representation (in real space) of the stripe order observed in nickelates (b) and cuprates (c) with the respective alignment of the spins and the hole concentration. In (a) are shown the resulting orientations of the superlattice peaks in the reciprocal space. Adapted from Ref. [44].

metallic state, also no superconductivity has been observed in LNO systems. Nevertheless, similarly to the cuprates [33], it presents stripe order upon oxygen and strontium dopings. While similar, the two stripe order present different orientations, as schematically shown in Fig. 1.5. As regards for oxygen doping, only particular δ values are allowed, corresponding to regular orderings of the excess oxygen. Indeed, as for δ -doped La_2CuO_4 [46], different stage orderings are observed [47]. For the most doped system (with $\delta = \frac{2}{15}$), a three-dimensional oxygen ordering is formed. This, allows the formation of a stripe order, where charge and spin modulations are intimately related to each other (Fig. 1.5). At this doping, the structure of the stripes is changing with temperature, and for $T > 110$ K no spin ordering is detected [48]. On the other hand, the charge order persists at even higher temperatures with an exponentially decreasing intensity of the related x-ray scattering satellites. Upon Sr doping, a similar picture is found [49]. As a function of doping, the ordering temperatures for the charge order are higher than the respective for the spin (and thus stripe) order, having a maximum transition temperatures around $x = \frac{1}{3}$ [49]. For even higher dopings, the stripe order melts and a checkerboard charge order is found for $x = \frac{1}{2}$ [49]. Thus, as for the cuprates [33], the charge order results to be more robust. Consistently, for $\text{YBa}_2\text{Cu}_3\text{O}_{6+\delta}$ no stripe order is found at any doping. Besides these similarities, a remarkable difference is observed if

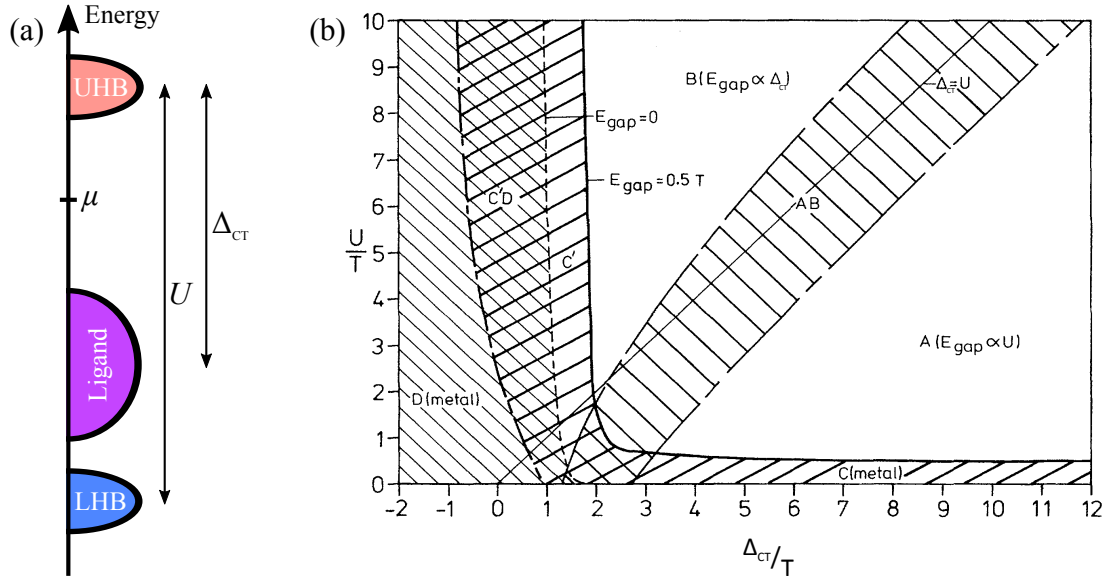


FIGURE 1.6: In (a) is illustrated schematically a charge transfer insulator. The upper (UHB) and lower (LHB) Hubbard bands are split in energy according to the on-site Coulomb interaction U , while the charge transfer gap Δ_{CT} is defined between the UHB and the band originated from the ligand (oxygen in the case of cuprates). A phase diagram U vs. Δ_{CT} , normalized to the first-neighbor hopping term (T), is presented in (b). Depending on the particular ratio between these two quantities, one can obtain a metal (C and D), a Mott insulator (A) or a charge-transfer insulator (B). Figure (b) is adapted from Ref. [50].

looking at spin excitations. In fact, as we will see in Chapter 5, stripe order is thought to be responsible for the hour-glass dispersion. Although, for LNO system, the dispersion of the spin excitations converges monotonically to the commensurate reciprocal-space position. These observations put under doubt the relation between the stripe order and hour-glass spin excitations.

To end this introduction Chapter, a few words has to be spent on the pressure effect on Coulomb interaction U which will be relevant in Chapter 6. In particular, we concentrate on the Mott and charge-transfer insulating phases. As shown in Fig. 1.6(a), a Mott gap between the upper (UHB) and lower (LHB) Hubbard bands is directly related to the on-site Coulomb interaction U . In a similar way we can define a charge-transfer gap Δ_{CT} between the UHB and the lower lying ligand band. If $\Delta_{CT} > U$ a Mott insulator is obtained, otherwise it is a charge-transfer insulator as in Fig. 1.6(a) [50, 51]. In order to quantify the Coulomb interaction, we can consider the ratio between U and the bandwidth W as a relevant parameter. Since the latter is related to the hopping integral t , the effective ratio which we will consider is U/t . When this ratio is high enough, the system becomes an insulator as shown in Fig. 1.6(b). Reducing U/t , for example by means of pressure, a metalization can occur, as it was observed in organic salts [52] and NiS_2 [53]. A pressure-induced metalization was predicted also for the solid hydrogen in 1935 by E. Wigner and H. B. Huntington [54]. This prediction has a direct relevance

for the high- T_c phonon-mediated superconductivity in solid hydrogen, since a metallic phase is a prerequisite for the latter. Although, due to the extreme pressures required for this phenomena (≈ 3.6 Mbar) [54], an experimental evidence has still to be carried out. So far, the record for the conventional superconductivity has been observed for H_3S under ≈ 1.5 Mbar with $T_c = 203$ K [55] and, more recently, for lanthanum hydride with $T_c = 215$ K at 1.5 Mbar [56] and $T_c \approx 260$ K at 1.9 Mbar [57].

From a theoretical point of view, a dependence of U is considered only for *high* pressures (of the order of Mbar) and it is considered constant in the moderate (kbar) limits [58]. Although, considering only a static limit ($\omega = 0$) can be already a crude approximation [59], it has been shown that even small distortions of the lattice can have a dramatic effect on U [58]. A detailed balance between the orbital overlap and the effective screening of Coulomb interaction, can produce an increase or decrease of U , having thus an important effect on the ratio U/t . This has a direct relevance for epitaxial thin films, where strain induced effects can be observed.

This thesis is organized as follows. Chapters 2 and 3 present an overview of experimental and theoretical methodologies adopted in this thesis. Following, three chapters present and discuss the experimental results obtained by means of synchrotron radiation. In Chapter 4 the interplay of charge order and superconductivity in $\text{Ir}_{1-x}\text{Pt}_x\text{Te}_2$ systems is presented as a function of hydrostatic pressure. Chapter 5 evidences the relevance of the d_{z^2} band on the magnetic-excitation spectrum in $\text{La}_{2-x}\text{Sr}_x\text{CuO}_4$ with $x = 0.12$. Strain induced effects on the magnons in thin films of La_2CuO_4 are discussed in Chapter 6. Each experimental Chapter starts with a relevant (for the experiment) introduction on the system. Conclusive remarks are presented in Chapter 7.

Chapter 2

Experimental Methodology

This Chapter introduces the experimental methods adopted in this study. I first explain how the samples were prepared for the synchrotron based experiments. Following, the pressure cell used in the hard x-ray diffraction (XRD) studies is presented. This Chapter will end by illustrating the state of the art of resonant inelastic x-ray scattering (RIXS) technique in cuprate systems. Theoretical insights about XRD and RIXS are presented in the following Chapter 3.

2.1 Sample Preparation

Sample preparation is important in order to conduct a successful experiment. This regards both the preparation of a clean surface and the identification of crystal axis orientation. Two types of samples has been studied: bulk crystals with $1 \times 1 \times 0.5 \text{ mm}^3$ dimensions and thin films with a surface of $5 \times 5 \text{ mm}^2$ and about 10–20 nm of thickness.

For hard x-ray measurements (100 keV) only an approximate orientation of the crystal axis is required. In fact, the sample is carefully aligned on the allowed Bragg peaks. In addition, surface quality is not influencing the results since hard x-rays probe mainly the bulk characteristics. Nevertheless, due to a transmission geometry, the dimension of the samples has to be restrained in order to avoid signal attenuation.

As regards for RIXS, we used soft x-rays ($\sim 1 \text{ keV}$), thus the surface roughness is important for a good quality data. In fact, approximately few tens of nanometers are probed and this penetration length depends on the angle between the beam and the normal to the surface. In our case we, studied both bulk and thin film samples. For the latter, no special preparation is needed since the surface is already flat (on atomic scale). For bulk crystals instead, a top-post cleaving technique has to be used. This consists of

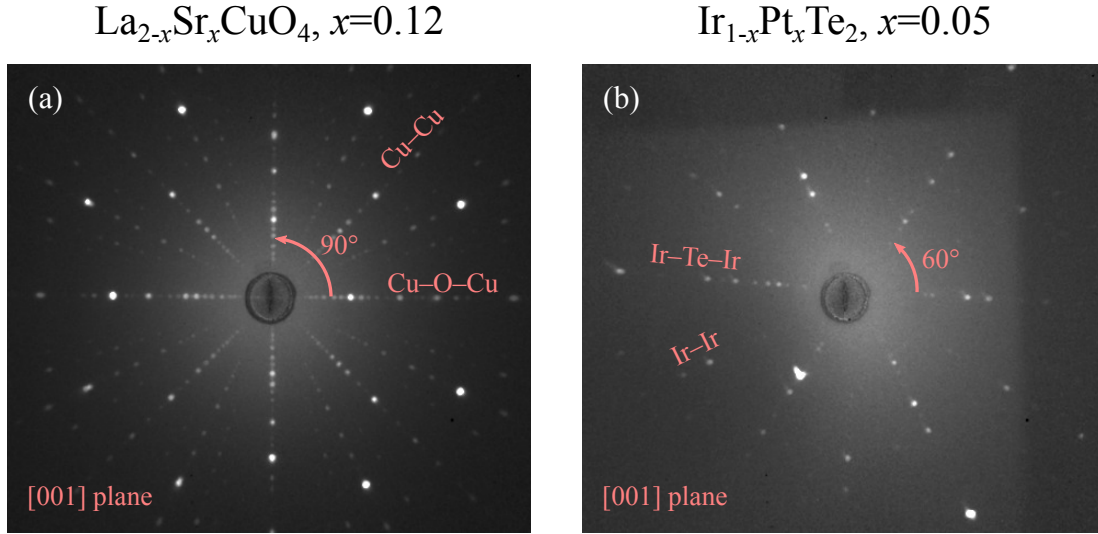


FIGURE 2.1: Laue diffraction pattern for $\text{La}_{2-x}\text{Sr}_x\text{CuO}_4$ with $x = 0.12$ (a) and $\text{Ir}_{1-x}\text{Pt}_x\text{Te}_2$ with $x = 0.05$ (b) samples. Crystal bond directions are indicated in the [001].

fixing, a metallic pin on top of the samples, assuring to cover the whole surface. As glue, we used EPO-TEK® E4110 silver epoxy from EPOXY TECHNOLOGY. Afterwards the sample is fixed to the sample-holder and loaded inside the ultra-high vacuum chamber. Once the temperature is stable the pin (on top of the sample) is removed cleaving the sample in two pieces and leaving a flat and contamination-free surface. This method works well only on layered systems.

As already mentioned, the samples have to be aligned before the experiment. To this end, we used a commercial Laue X-Ray Imaging System from Photonic Science. An x-ray beam is focused on the sample and the diffracted signal is detected by a two-dimensional screen in backscattering geometry. Since the incident beam is *white*, several layers fulfill the Bragg condition and thus, multiple peaks are visible at the same time. By rotating the sample, high-symmetry planes are found and crystal axis identified. In Fig. 2.1(a) is shown a typical Laue pattern for $\text{La}_{2-x}\text{Sr}_x\text{CuO}_4$ system. Crystal axes can be identified thanks to the higher-order reflections. Indeed, these reflections are closer to the Cu–Cu than to the Cu–O–Cu bond direction. In this way the (110) and (100) = (010) crystal axis are found respectively. We can also observe [Fig. 2.1(a)] that the pattern has a four-fold symmetry, as expected for a tetragonal [001] plane. On the other hand, a six-fold rotational symmetry is present for $\text{Ir}_{1-x}\text{Pt}_x\text{Te}_2$ with $x = 0.05$ sample [Fig. 2.1(b)]. This confirms the trigonal high-temperature structure for this compound (see Chapter 4 for further details).

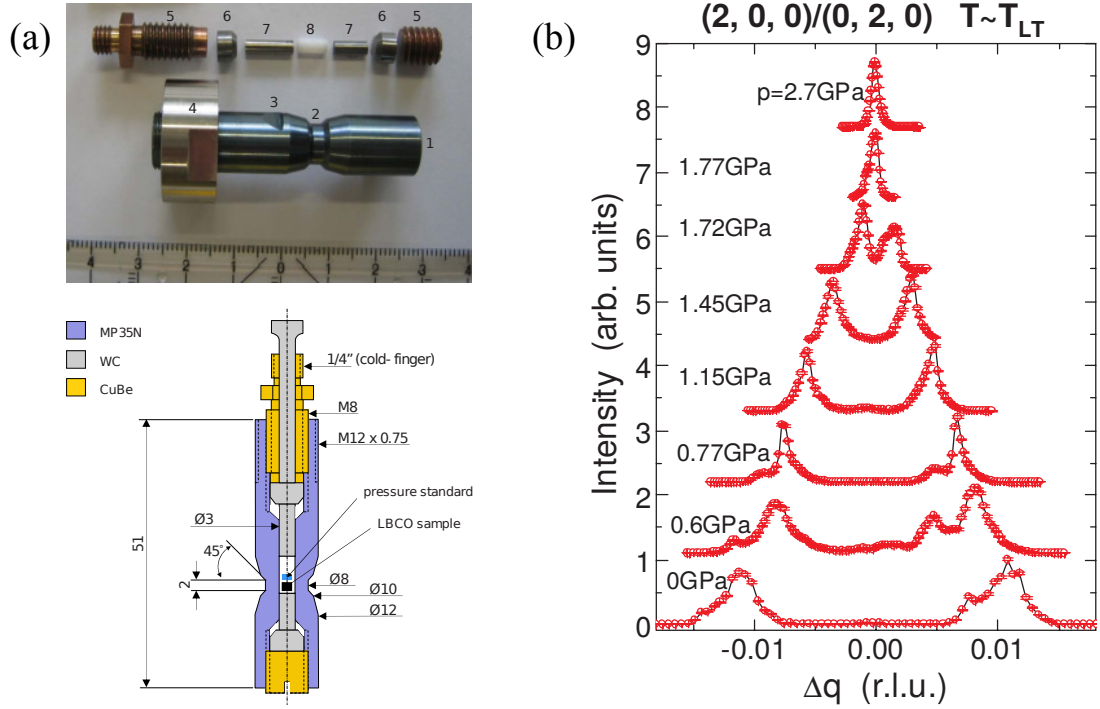


FIGURE 2.2: In (a) is shown the clamp-type pressure cell used during the experiments. Top: picture of the cell with all the different components, from which we see the Teflon cup (8) and the x-ray window (2). Bottom: schematic representation of the pressure cell with the dimensions indicated in millimeters. Splitting of the (200) (or equivalently (020)) Bragg peak for $\text{La}_{2-x}\text{Ba}_x\text{CuO}_4$ with $x = 0.125$, as a function of hydrostatic pressure is shown in (b). Adapted from Refs. [60] and [61] respectively.

2.2 Hard X-ray Diffraction

The first diffraction pattern was observed by Max von Laue and collaborators in (1912) using x rays. In fact, since the interatomic distances are of the order of 1 \AA , wavelengths of the same magnitude are necessary. For a 100 keV x-ray beam, indeed, a $\lambda \sim 0.12 \text{ \AA}$ wavelength is obtained. In 1913 Bragg formulated a geometrical description to explain the diffraction pattern of a crystal. He considered planes of atoms separated regularly by a distance d . The incoming light is then reflected specularly by each plane. A diffraction pattern occurs only if a constructive interference is obtained. Thus, the phase difference between the beams must be equal to an integer number of λ . The Bragg law reads as:

$$n\lambda = 2d \sin\left(\frac{2\theta}{2}\right) \quad \text{with } n \text{ integer} \quad (2.1)$$

where 2θ is the scattering angle between the incident and reflected beams. The distance d between the planes can be expressed in terms of lattice constants. For example, for a Bravais lattice with a tetragonal symmetry one finds that:

$$\frac{1}{d^2} = \frac{h^2 + k^2}{a^2} + \frac{l^2}{c^2}, \quad (2.2)$$

being h, k and l the Miller indexes of the system. In this way, knowing the scattering angle 2θ and the wavelength of the incident beam, it is possible to obtain the lattice constants a , b and c of the crystal.

2.2.1 Pressure Cell

Hard x-ray measurements were performed at P07 beamline [62] in PETRAIII in DESY. Hydrostatic pressures were applied with a clamp-type pressure cell [60] [see Fig. 2.2(a)]. This cell is specifically designed to study weak reflections (i.e. CDWs) in transmission geometry using 100 keV x rays. The sample is loaded in a Teflon cup, filled with DAPHNE oil as transmitting medium, which is in turn inserted inside the pressure cell. The chamber of this device is made of MP35N material. With an inner diameter of 3 mm loads of about 2300 kg are allowed before reaching the deformation limit of the material.

In order to track the nominal value of the pressure, $\text{La}_{2-x}\text{Ba}_x\text{CuO}_4$ with $x = 0.125$ crystal was loaded inside the cell together with the sample. Due to a crystal symmetry breaking, i.e. the occurrence of orthorhombicity, it was possible to estimate the pressure by the splitting of the (200) or (020) reflections [61]. Both reflections are present at the same time, since the orthorhombic domains coexist in the crystal. This splitting decreases with applied pressure to a point where only one peak is detected at about 17.7 kbar [see Fig. 2.2(b)]. These *pressure-calibration* measurements were performed at 60 K.

2.3 Resonant Inelastic X-ray Scattering

Resonant inelastic x-ray scattering (RIXS) experiments were performed at the ADDRESS beamline [63] in Swiss Light Source (SLS). A picture of the instrument is shown in Fig. 2.3(a). This technique is a *photon in – photon out* synchrotron based technique. Its main principle lies in tuning the incident photon energy to an absorption edge of the sample. As we will see in Chapter 3, this enhances the scattering process and, in addition, allows element sensitivity. Besides charge, it is also possible to observe spin excitations, making this technique complementary to inelastic neutron scattering (INS). The two main differences with INS are that, small samples can be probed, due to a stronger interaction of x-rays with matter [64], and that it allows measurements close to the incident beam position. Nevertheless, a few limitations have to be pointed out. For soft (~ 1 keV) RIXS, which is relevant to this study, the energy loss resolution (~ 100 meV at Cu L_3 edge [65]) is big if compared to a typical INS experiment ($\sim 1 - 10$ meV [66]). In

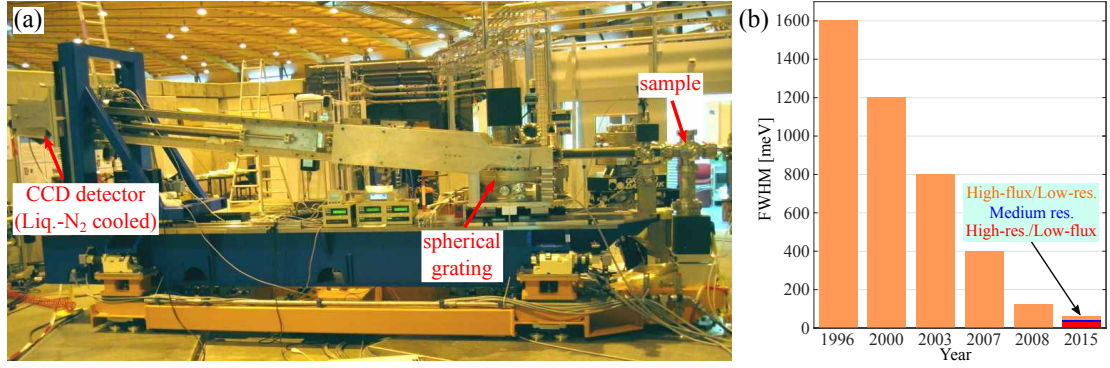


FIGURE 2.3: (a) Photo of the RIXS endstation at SLS. Sample vacuum chamber, spherical grating (allowing the photon-energy differentiation) and the CCD detector are indicated. Adapted from www.psi.ch/sls/address. (b) Enhancement of RIXS resolution at Cu L_3 edge through years. In chronological order, the reported resolution refers to BLBB at the Photon Factory [70], I511 – 3 at MAXII [71], AXES (ID08) at ESRF [72], AXES (ID08) at ESRF [73], SAXES (ADDRESS) at SLS [74] and ERIXS (ID32) at ESRF [67].

addition, due to the scattering geometry, a limited reciprocal space can be studied, which is usually contained to the first Brillouin zone. This is because in RIXS experiments, the scattering angle 2θ is fixed and only reflection-scattering geometry is possible (for soft x-rays). As a consequence, the reciprocal space is limited when the scattered beam becomes parallel to the surface of the sample. Nevertheless, the RIXS resolution has increased considerably over the years, as shown in Fig. 2.3(b). Currently a resolution of ~ 35 meV can be achieved with ERIXS spectrometer at ESRF [67], at the cost of reducing the flux and thus increasing the acquisition time. For this thesis, AXES spectrometer at SLS [68] was used. Although, a resolutions of about 120 meV was already achievable in 2008, new improvements to the spectrometer has been applied over the years. One of these, consists in utilizing three CCDs, at the detector stage, instead of a single one [69]. This allows to reduce the acquisition time since a better statistics is available. Furthermore, a single-photon counting software is adopted [69], which allows to separate each pixel in four sub-pixels, thus improving the resolution of the instrument.

The process of RIXS can be described in a two-step model (Fig. 2.4). A core electron absorbs the incident photon with momentum $\hbar\mathbf{k}_{in}$ and energy $\hbar\omega_{in}$ and gets promoted to the unoccupied band. The system is now in a highly excited state. A de-excitation occurs in a time scale of 1 fs. This second step can create an elastic scattering, where the excited electron decays back to the original state and emits a photon with energy $\hbar\omega_{out} = \hbar\omega_{in}$ and momentum $|\hbar\mathbf{k}_{out}| = |\hbar\mathbf{k}_{in}|$. On the other hand, an excitation can be created in the system, and thus the outgoing photon will be characterized by $\hbar\omega_{out} < \hbar\omega_{in}$ and

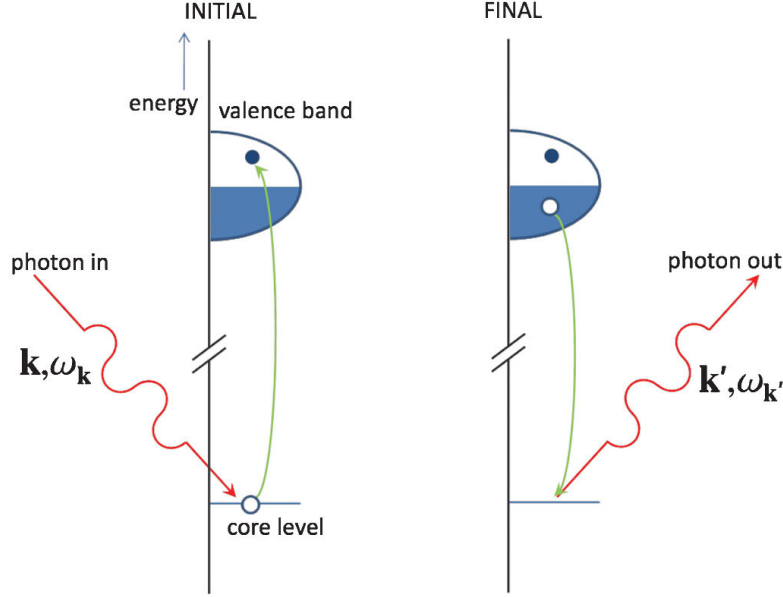


FIGURE 2.4: Schematic representation of RIXS process. Figure adapted from [75].

$|\hbar\mathbf{k}_{out}| < |\hbar\mathbf{k}_{in}|$. From this we can write the following conservation equations:

$$\begin{aligned}\hbar\omega_{in} &= \hbar\omega_{out} + E_{loss} \\ \hbar\mathbf{k}_{in} &= \hbar\mathbf{k}_{out} + \hbar\mathbf{q}^{exc}\end{aligned}\tag{2.3}$$

where E_{loss} and $\hbar\mathbf{q}^{exc}$ are the energy and momentum transfer of the created excitation. Note that E_{loss} is small compared to the incident energy of the photon (~ 1 eV to ~ 1 keV). In this way it results that $\hbar\omega_{in} \approx \hbar\omega_{out}$ and consequently $\hbar\mathbf{k}_{in} \approx \hbar\mathbf{k}_{out}$ since $|\hbar\mathbf{k}_{out}| = \frac{\hbar\omega_{out}}{c}$ and $|\hbar\mathbf{k}_{in}| = \frac{\hbar\omega_{in}}{c}$. In this way, with a reasonable degree of accuracy, we can assume the momentum transfer of the excitation \mathbf{q}^{exc} to be equal to the respective \mathbf{q} of the elastic scattering (of the same spectra). Within our studies the scattering angle 2θ was always fixed and equal to 130° . By geometrical construction one obtains:

$$\begin{aligned}\mathbf{q} &= 2\mathbf{k}_{in} \cos \frac{2\theta}{2} \\ \mathbf{q}_{//} &= \mathbf{q} \sin \delta_s\end{aligned}\tag{2.4}$$

where $\mathbf{q}_{//}$ is the parallel (to the surface) component of the transfer vector and δ_s the angle from the specular condition. The specular condition is defined as the geometry at which the angle between the incident and outgoing beams is the same with respect to the normal to the surface of the sample. Also note that, in our case, only the parallel component of \mathbf{q} is relevant, since the considered systems are quasi two-dimensional.

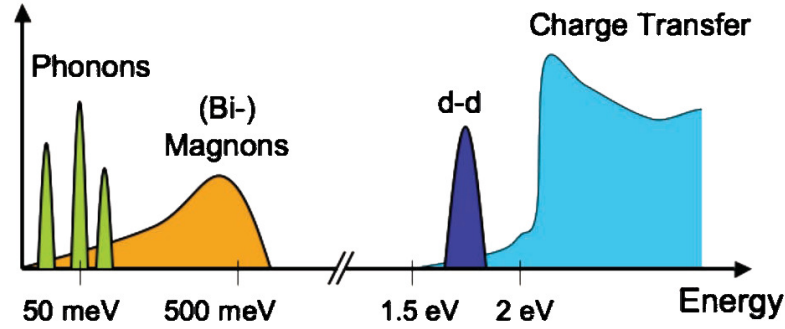


FIGURE 2.5: Schematic representation of the RIXS observable excitations in cuprates. Adapted from [75].

2.3.1 RIXS on Cuprates

The possible excitations (in cuprates), that can be observed with RIXS, are schematically represented in Fig. 2.5. The first excitation, that can be seen at about 50 meV, corresponds to lattice vibrations. While phonons can give interesting information, their observation is still limited by the resolution of the instrument. To date, even with the highest resolution available, the phonon spectral weight is usually overlapped with the elastic line. Thus the, resulting information, depends strongly on the elastic-line subtraction. At higher energy loss, magnetic excitations can be observed. For cuprates, these correspond to single-flip excitations that are at about 300 meV. In addition, a small bi-magnon signal can be observed, corresponding to a double-spin flip excitation.

At higher energies (1 – 2 eV) dd excitations are present (Fig. 2.5). These correspond to the transitions of the electron inside the $3d$ band. In cuprates, the highest lying band has $d_{x^2-y^2}$ symmetry which, with the $d_{3x^2-z^2}$ -symmetry band, forms the so-called e_g states. The remaining d_{xy} , d_{xz} and d_{yz} bands are grouped in the t_{2g} states. The e_g and t_{2g} states are formed due to the crystal-field splitting of the out-of-plane elongated CuO_6 octahedra. Thus the dd excitations result from the transition between the $d_{x^2-y^2}$ and the remaining bands. In this way information about the crystal-field splitting can be obtained from RIXS spectra. Unfortunately, due to intrinsic broadening, it is complicated to distinguish clearly each contribution. To overcome this problem, polarization analysis can be performed and results compared to the theoretical-predicted cross section [76]. Nevertheless, since this signal is the less momentum dependent feature of the spectra, it is used to normalize the intensity of the data.

At even higher energy loss, charge transfer excitations can be observed (Fig. 2.5). These correspond to the excitations involving the oxygen p_x and p_y bands and are typically extremely broad at Cu L_3 edge. Additionally, a progressive decay of the signal, at higher energies, complicates the analysis.

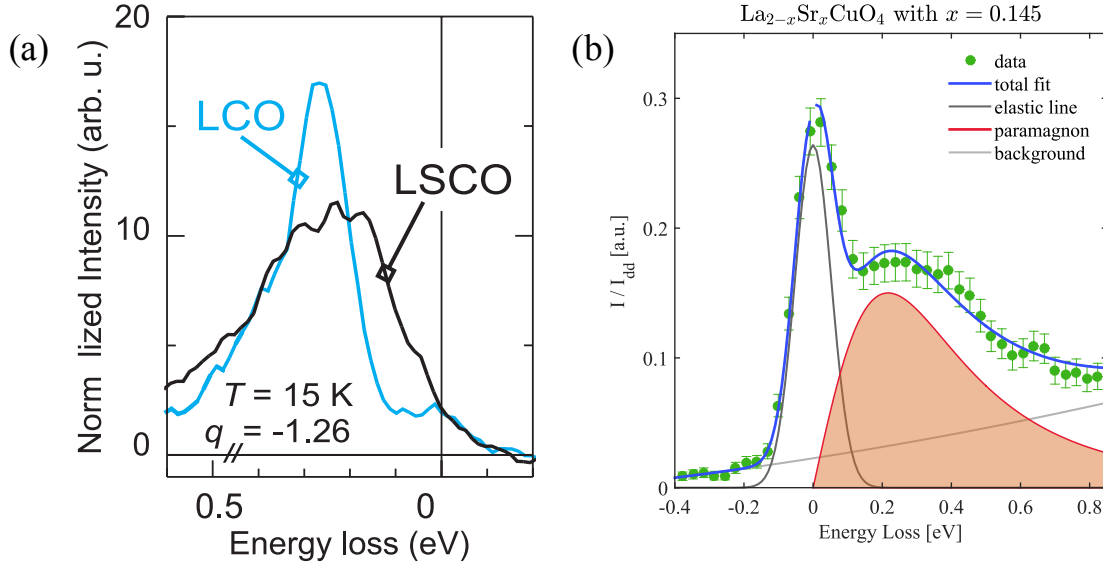


FIGURE 2.6: (a) RIXS spectra, at Cu L_3 edge, for $\text{La}_{2-x}\text{Sr}_x\text{CuO}_4$ (LCO) and La_2CuO_4 (LSCO) as indicated. Temperature and momenta transfer (expressed in $1/a$ units) are shown in the lower part. Figure adapted from [80]. (b) RIXS spectra for $\text{La}_{2-x}\text{Sr}_x\text{CuO}_4$ ($x = 0.145$) with the respective fit (solid blue line) composed of elastic line and background (solid gray lines), and paramagnon excitation (red area) modeled using Eq. 2.5

Let us come back to the magnetic excitations. In Fig. 2.6(a) it is shown a typical spectra for the doped $\text{La}_{2-x}\text{Sr}_x\text{CuO}_4$ (LSCO) system, which is compared to La_2CuO_4 (LCO). We can observe that LCO presents a clear defined peak while LSCO is characterized by a broad line-shape. This is because in LSCO system there is no long-range antiferromagnetic order and the mobile carriers damp the magnetic excitations. To extract the magnon energy and its linewidth, a fit to the data has to be performed. While for LCO a Lorentzian function reasonably describes the experimental data, for LSCO another functionality is needed. A common way to fit the damped magnetic excitations (paramagnons) is to use a response function for a damped harmonic oscillator [77–79]:

$$\begin{aligned}\chi''(\omega) &= \chi_0'' \frac{\gamma\omega}{(\omega^2 - \omega_0^2) + \omega^2\gamma^2} \\ &= \frac{\chi_0''\gamma/2}{2\omega_1} \left[\frac{1}{(\omega - \omega_1)^2 + (\gamma/2)^2} - \frac{1}{(\omega + \omega_1)^2 + (\gamma/2)^2} \right]\end{aligned}\quad (2.5)$$

where the damping coefficient can be expressed as $\gamma/2 = \sqrt{\omega_0^2 - \omega_1^2}$. In this expression ω_1 is the pole of the excitation while ω_0 corresponds roughly to the peak maximum. In this way, the RIXS intensity can be modeled by $\chi(\omega) \cdot [n_B(\omega) + 1]$, where $n_B(\omega) = \left(e^{\frac{\hbar\omega}{k_B T}} - 1\right)^{-1}$ is the Bose factor. The fit is performed in a way to obtain ω_0 and $\gamma/2$, and consequently extract ω_1 which is the energy of the excitation [79]. The quality of the fit can be appreciated in Fig. 2.6(b), where a Gaussian functionality and a second order polynomial are used for the elastic line and background respectively. The red area in Fig. 2.6 is the paramagnon modeled using Eq. 2.5.

Chapter 3

Theoretical Background

In this Chapter an introduction on the theoretical aspects adopted in this thesis is given. In particular, the XRD and RIXS processes are presented. The Chapter will end by introducing the Hubbard model at strong coupling, which is used to model the dispersion of the spin-excitations.

3.1 XRD Structure Factor

Although the Bragg law (Eq. 2.1) can give us important information about the sample, a more complete description of the diffracted pattern can be obtained by considering a scattering potential $U_i(\mathbf{r})$, between the x-ray and the electronic cloud of the i th atom within the unit cell. In real space, the position of each atom can be identified by the vector $\mathbf{R}_i^0 = n_1a + n_2b + n_3c$, where i corresponds to a given set of integers (n_1, n_2, n_3) . The total potential results to be $U^{tot}(\mathbf{r}) = \sum_i \mathbf{U}_i(\mathbf{r} - \mathbf{R}_i^0)$. We can thus define the *atomic scattering amplitude* as the Fourier transform of the atomic scattering potential:

$$U_{i,\mathbf{Q}} = \int U_i(\mathbf{r} - \mathbf{R}_i^0) e^{-j\mathbf{Q}\mathbf{r}} d\mathbf{r}, \quad (3.1)$$

where \mathbf{Q} is the reciprocal vector $2\pi \left(\frac{h}{a}, \frac{k}{b}, \frac{l}{c}\right)$. From this, the total scattering amplitude will be $U_{\mathbf{Q}}^{tot} = \sum_i U_{i,\mathbf{Q}}$.

Since, in an x-ray diffraction experiment, one measures the intensity I of the scattered beam, the differential cross-section $\frac{d\sigma}{d\Omega}$ has to be defined. In fact it results that $I \propto \frac{d\sigma}{d\Omega}$. To this end, one has to introduce the so-called *structure factor*:

$$F(\mathbf{Q}) = \sum_i U_{i,\mathbf{Q}} e^{j\mathbf{Q}\mathbf{R}_i^0}. \quad (3.2)$$

It can be shown that $\frac{d\sigma}{d\Omega} \propto |F(\mathbf{Q})|^2$.

As we will see in Chapter 4, a charge-density-wave system will be studied with hard x rays. To account for this phenomena we can express the position vector as $\mathbf{R}_i = \mathbf{R}_i^0 + \sum_m \mathbf{u}_m \sin \mathbf{q}_m \mathbf{R}_i^0$. The reciprocal lattice vector becomes $\mathbf{Q} = \boldsymbol{\tau} + n\mathbf{q}_m$, where n is an integer and $\boldsymbol{\tau}$ refers to the diffraction peaks in the absence of charge density wave. The vector \mathbf{u}_m , being the amplitude of the Fourier component with wavevector \mathbf{q}_m , represents the displacement of the atom associated with the charge modulation.

Let us, for simplicity, consider a modulation were only one component with amplitude \mathbf{u} and wavevector \mathbf{q} is present. This will generate a perfectly sinusoidal modulation of the charge in the system. Substituting the resulting \mathbf{R}_i in Eq. 3.2, we can calculate the *structure factor* for the charge density wave. In this case thus results:

$$I \propto |\mathbf{Q} \cdot \mathbf{u}|^2. \quad (3.3)$$

This simple relation has an important consequence: the direction at which the (charge density wave) satellite is more intense corresponds to the preferred displacement direction. Thus, by scanning the satellite peaks along the reciprocal space, it is possible to recreate the modulation in real space [81].

3.2 RIXS Cross Section

Here the RIXS cross section will be presented within a perturbation theory and dipole approximation treatments [75]. To this end the Hamiltonian of the matter-light interaction reads as:

$$\begin{aligned} H = \sum_i^N \left(\frac{[\mathbf{p}_i + e\mathbf{A}(\mathbf{r}_i)]^2}{2m} - e\phi(\mathbf{r}_i) + \frac{e\hbar}{2m} \boldsymbol{\sigma}_i \cdot \mathbf{B}(\mathbf{r}_i) \right. \\ \left. + \frac{e\hbar}{2(2mc)^2} \boldsymbol{\sigma}_i \cdot \{ \mathbf{E}(\mathbf{r}_i) \times [\mathbf{p}_i + e\mathbf{A}(\mathbf{r}_i)] - [\mathbf{p}_i + e\mathbf{A}(\mathbf{r}_i)] \times \mathbf{E}(\mathbf{r}_i) \} \right) \\ + H^C + \sum_{\mathbf{k}, \varepsilon} \hbar\omega_{\mathbf{k}} \left(c_{\mathbf{k}, \varepsilon}^\dagger c_{\mathbf{k}, \varepsilon} + \frac{1}{2} \right) \end{aligned} \quad (3.4)$$

where \mathbf{A} is the vector potential defined as $\mathbf{E}(\mathbf{r}) = -\nabla\phi - \partial\mathbf{A}/\partial t$ and $\mathbf{B} = \nabla \times \mathbf{A}$ with a continuously differentiable scalar function ϕ . \mathbf{p}_i and \mathbf{r}_i are the momentum and position operators of the i -th electron and $\boldsymbol{\sigma}_i$ the corresponding Pauli matrix. Creation (annihilation) of the photon with wave vector \mathbf{k} and polarization ε is represented by $c_{\mathbf{k}, \varepsilon}^\dagger$ ($c_{\mathbf{k}, \varepsilon}$) operator.

The first two terms of this Hamiltonian represent the kinetic and potential energies of electron in the presence of electromagnetic field. It follows by a Zeeman splitting and spin-orbit coupling parts. H^C contains the remaining electrostatic contributions, among which the electron-electron interaction. The last term is the energy of the radiation summed over all the modes.

We can separate the Hamiltonian in two parts. One is the Hamiltonian H^0 of electrons and the phonons which are not interacting. In this way the resulting eigenfunction is the product of the respective eigenfunctions. Consequently, the eigenvalue of this system is the sum the eigenvalues for the electronic and radiation Hamiltonians. The remaining part H' , instead, contains the information about the interaction between electrons and light. In this way we can treat H' as a perturbation to H^0 .

Within the two step model, the initial state is composed by the ground state $|g^{el} >$ of the electrons and the incident photon described by $|1_{\mathbf{k}_{in}, \varepsilon_{in}} >$. Where $|1_{\mathbf{k}_{in}, \varepsilon_{in}} >$ is one-photon wave function resulting from application of the creation operator $c_{\mathbf{k}, \varepsilon}^\dagger$ to the ground state $|0 >$. This results in an overall ground state $|g > = |g^{el}; 1_{\mathbf{k}_{in}, \varepsilon_{in}} >$ whose eigenvalue can be represented by $E_g = E_g^{el} + \hbar\omega_{in}$. In a similar way we can represent the final state as $|f > = |f^{el}; 1_{\mathbf{k}_{out}, \varepsilon_{out}} >$ whose eigenvalue corresponds to $E_f = E_f^{el} + \hbar\omega_{out}$.

With this notation the transition rate w for the scattering process can be written as:

$$w = \frac{2\pi}{\hbar} \sum_f \left| \langle f | H' | g \rangle + \sum_n \frac{\langle f | H' | n \rangle \langle n | H' | g \rangle}{E_g - E_n} \right|^2 \delta(E_f - E_g) \quad (3.5)$$

where $|n >$ is the intermediate state with eigenvalue E_n . In a non-resonant process the first term is large as compared to the second, which in turn is neglected. For resonant scattering, instead, the second term gets large since for some $|n >$ the denominator is very small resulting from $E_g \sim E_n$.

Neglecting the first term, we can expand the second one and obtain:

$$w = \frac{e^2 \hbar}{2m^2 V \epsilon_0 \sqrt{\omega_{in} \omega_{out}}} \sum_n \sum_{i, i'} \frac{\langle f | \epsilon_{out}^* \cdot \mathbf{p}_{i'} e^{-i\mathbf{k}_{out} \cdot \mathbf{r}_{i'}} | n \rangle \langle n | \epsilon_{in} \cdot \mathbf{p}_i e^{-i\mathbf{k}_{in} \cdot \mathbf{r}_i} | g \rangle}{E_g - E_n + i\Gamma_n} \quad (3.6)$$

where V is the volume of the system and Γ_n accounts for the intrinsic broadening due to the lifetime of the intermediate state. Substituting this expression in Eq. 3.5 one obtains the Kramers–Heisenberg expression describing the RIXS cross section.

Since in our case, only the soft x-ray photons are considered, it is reasonable to use the dipole approximation. Consequently the term $e^{-i\mathbf{k} \cdot \mathbf{r}}$ varies slowly over the characteristic

distance of the atomic wavefunction. Eq. 3.6 further simplifies in:

$$\begin{aligned}
 w &\approx \frac{e^2 \hbar}{2m^2 V \epsilon_0 \sqrt{\omega_{in} \omega_{out}}} \sum_n \sum_{i,i'}^N \frac{\langle f | \epsilon_{out}^* \cdot \mathbf{p}_{i'} | n \rangle \langle n | \epsilon_{in} \cdot \mathbf{p}_i | g \rangle}{E_g - E_n + i\Gamma_n} \\
 &\approx \frac{e^2 \hbar}{2m^2 V \epsilon_0} \sqrt{\omega_{in} \omega_{out}} \sum_n \sum_{i,i'}^N \frac{\langle f | \epsilon_{out}^* \cdot \mathbf{r}_{i'} | n \rangle \langle n | \epsilon_{in} \cdot \mathbf{r}_i | g \rangle}{E_g - E_n + i\Gamma_n}.
 \end{aligned} \tag{3.7}$$

3.3 Hubbard Model

To describe the magnetic-excitation dispersion extracted from RIXS studies on $\text{La}_{2-x}\text{Sr}_x\text{CuO}_4$ with $x = 0.12$ (Chapter 5) and thin films of $\text{La}_{2-x}\text{Sr}_x\text{CuO}_4$ (Chapter 6), a single-band Hubbard model at strong coupling is used. The Hubbard model is a powerful tool which can be used, for example, to describe the metal to (Mott) insulator transition (see Fig. 3.1). It was shown, that in order to describe the magnon dispersion in bulk La_2CuO_4 [82, 83], it is necessary to consider also the second- and third-neighbor hopping integrals [84, 85]. In this section I will present the analytical solution for the magnon dispersion and comment on the result.

A Hubbard Hamiltonian for a strongly-correlated electron system can be formulated as follows:

$$\begin{aligned}
 H = & -t \sum_{\langle i,j \rangle, \sigma} c_{i,\sigma}^\dagger c_{j,\sigma} - t' \sum_{\langle\langle i,j \rangle\rangle, \sigma} c_{i,\sigma}^\dagger c_{j,\sigma} \\
 & - t'' \sum_{\langle\langle\langle i,j \rangle\rangle\rangle, \sigma} c_{i,\sigma}^\dagger c_{j,\sigma} + U \sum_i n_{i,\uparrow} n_{i,\downarrow}
 \end{aligned} \tag{3.8}$$

where t , t' and t'' are the first-, second- and third-nearest neighbor hopping integrals. The electron-electron correlations are described by the on-site Coulomb interaction U . A creation (annihilation) of an electron at the site i and spin $\sigma = \uparrow, \downarrow$ is represented by the respective operator $c_{i,\sigma}^\dagger$ ($c_{i,\sigma}$). By definition the density operator at the site i is $n_{i,\sigma} \equiv c_{i,\sigma}^\dagger c_{i,\sigma}$. The summation in the first three terms is done over the first- $\langle \star \rangle$, second- $\langle\langle \star \rangle\rangle$ and third-nearest neighbor sites $\langle\langle\langle \star \rangle\rangle\rangle$.

Using this Hamiltonian at strong coupling it is possible to pass from a Hubbard to a Heisenberg type of representation by defining the exchange-interaction constants in terms of t , t' , t'' and U . In addition, also the ring-exchange interactions are considered, since they have been shown relevant for La_2CuO_4 . For a detailed derivation please consult Refs. [84, 85]. The magnon dispersion can be represented in the following way:

$$\omega(\mathbf{q}) = Z \sqrt{A(\mathbf{q})^2 - B(\mathbf{q})^2}. \tag{3.9}$$

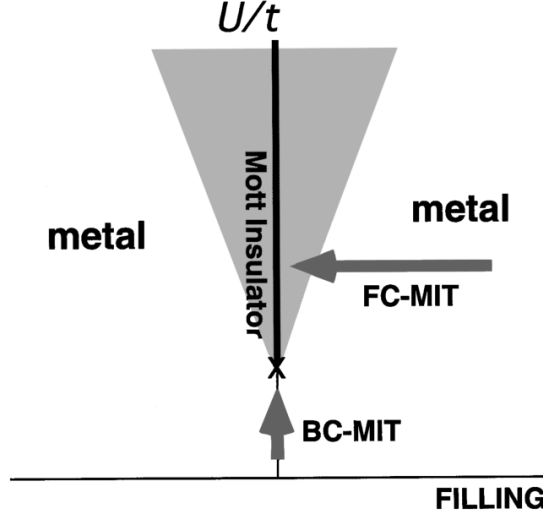


FIGURE 3.1: Schematics of metal-insulator transition (MIT) as a function of filling and ratio U/t , constructed from a Hubbard model. As shown, a Mott insulator is formed either by filling control (FC-MIT) or by bandwidth control (BC-MIT). Figure adapted from Ref. [51].

Here the renormalization factor Z accounts for the quantum fluctuations. It was shown that Z has a small momentum dependence. Having a negligible contribution in the magnon dispersion, a constant value of 1.219 (calculated for La_2CuO_4) is used in this thesis.

For each $\mathbf{q} = (h, k)$, with h and k expressed in reciprocal lattice units $2\pi/a$ and $2\pi/b$, the A and B terms depend on t, t', t'' and U . To simplify the notation we can define

$$\begin{aligned} P_j(h, k) &= \cos jha + \cos jka \\ X_j(h, k) &= \cos jha \cos jka \\ X_{3a}(h, k) &= \cos 3ha \cos ka + \cos ha \cos 3ka \end{aligned}$$

such that:

$$\begin{aligned} A &= 2J_1 + J_2 (P_2 - 8X_1 - 26) + 2J'_1 (X_1 - 1) \\ &+ \left[J''_1 - \frac{8J_1}{U^2} (-t'^2 + 4t't'' - 2t''^2) \right] (P_2 - 2) \\ &+ 2J'_2 (-2P_2 + 4X_1 + X_2 - 1) \\ &+ \frac{2J'_1 J''_1}{U} (5P_2 + 2X_1 - 3X_2 - X_{3a} - 7) \\ &+ J''_2 (4P_2 + P_4 - 8X_2 - 2) \end{aligned} \tag{3.10}$$

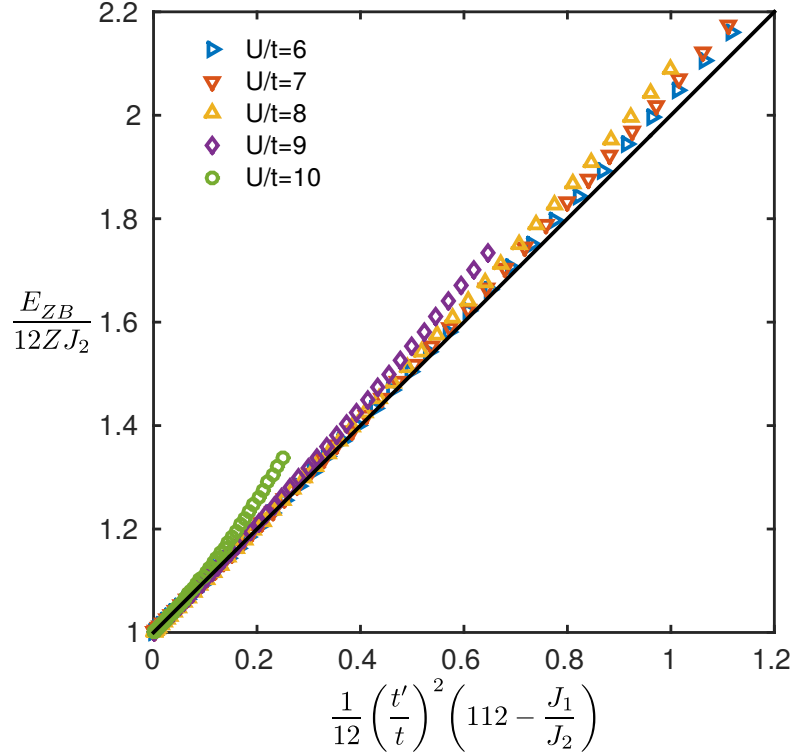


FIGURE 3.2: Exact numerical (scattered points) solution for the zone-boundary dispersion E_{ZB} , for U/t ratio as indicated, compared with the respective approximated analytical one (solid black line) obtained for $U/t = 8$. Note that $-t'/t$ varies from 0 to 0.5 while having $t = 0.43$ eV.

and

$$B = -J_1 P_1 + 16J_2 P_1 - \frac{4J_1}{U^2} [(6t'^2 - t't'') (X_1 - 1) + 3t''^2 (P_2 - 2)] P_1. \quad (3.11)$$

Here, the exchange-interaction constants are defined as $J_1 = \frac{4t^2}{U}$, $J_2 = \frac{4t^4}{U^3}$, $J'_1 = \frac{4t'^2}{U}$, $J'_2 = \frac{4t'^4}{U^3}$, $J''_1 = \frac{4t''^2}{U}$ and $J''_2 = \frac{4t''^4}{U^3}$. Note that no l component of \mathbf{q} is being considered. In fact, this model is for (quasi) two-dimensional systems only, where the coupling between the layers is small.

Now, let us define the zone boundary dispersion E_{ZB} . Here, we consider the Mott insulator La_2CuO_4 and the related doped systems. Since an antiferromagnetic order is present in the undoped system, we have to consider the boundary the of the respective Brillouin zone. The latter is rotated by 45° , with respect to the lattice Brillouin zone and it is centered around the high-symmetry M point $(1/2, 1/2)$. It thus results that $E_{ZB} = \omega(1/2, 0) - \omega(1/4, 1/4)$ in the lattice Brillouin-zone notation.

Having an analytical solution for ω we can thus derive an expression for E_{ZB} . To this end, it is useful to consider the case where only t and U are present. In this case, it

results that, at the high-symmetry $(1/2, 0)$ and $(1/4, 1/4)$ points the B term (Eq. 3.11) is equal to zero. We thus, obtain that the zone-boundary dispersion depends only on the second-neighbor exchange interaction: $E_{ZB} = 12ZJ_2$.

Including the contribution from t' and t'' to E_{ZB} , one obtains a complicated expression. For this reason an approximated solution is proposed, where $-t''/t' = 1/2$ (as it is often assumed) and terms scaling with J'_2 , J''_2 and $J'_1J''_1$ are neglected. Within these limits we obtain:

$$\frac{E_{ZB}}{12ZJ_2} \approx 1 + \frac{1}{12} \left(112 - \frac{J_1}{J_2} \right) \left(\frac{t'}{t} \right)^2, \quad (3.12)$$

which is valid for:

$$\frac{U}{t} \geq \sqrt{\frac{28 + 112 \left(\frac{t'}{t} \right)^2}{2 + 3 \left(\frac{t'}{t} \right)^2}}, \quad \text{and} \quad \left| \frac{t'}{t} \right| \lesssim 0.686. \quad (3.13)$$

Note that, the constrains in 3.13 are reasonable for the system which are considered in the present studies. In fact $-t'/t$ is usually limited to 0.5. From this results that, U/t should be approximately larger than 4.5.

To check if the solution in Eq. 3.12 is a good approximation to the exact solution, a direct comparison between the two is shown in Fig. 3.2. Here, $-t'/t$ varies from 0 to 0.5 and $t = 0.43$ eV. As we can see, the approximated solution agrees well with the exact numerical calculations for several values of U/t . Notice, that the approximated solution, varies negligibly with U/t . Thus, the difference between the two solutions lies in the higher order terms that have been omitted. For high enough $-t'/t$, this terms indeed, become important to describe the zone-boundary dispersion.

Another quantity, which will be useful for our analyses is the effective first-neighbor exchange interaction. Within our formalism it can be expressed as:

$$J_{\text{eff}} = 4\frac{t^2}{U} - 64\frac{t^4}{U^3}. \quad (3.14)$$

the first term corresponds to J_1 while the second take into account the effect of the cyclic interactions. For simplicity the additional corrections, coming from t' and t'' , has been neglected. The importance of Eq. 3.14 comes from the fact that the dispersion at the high-symmetry $(1/2, 0)$ point is approximately $2J_{\text{eff}}$. In this way the variation of the exchange-interaction can be tracked directly from the experimental data without a detailed analysis.

Chapter 4

Charge Order & Superconductivity in $\text{Ir}_{1-x}\text{Pt}_x\text{Te}_2$

Competing orders are of great interest in condensed matter physics. To this end, charge order and superconductivity play an important role. In cuprate systems a suppression of superconducting transition temperature T_c is observed around the anomalous $1/8$ doping. This suppression, which is stronger for $\text{La}_{2-x}\text{Ba}_x\text{CuO}_4$ among the cuprate family, is associated with the presence of charge order, or more specifically by the presence of stripe order [86]. Interestingly, in cuprates CO persists down to the lowest reachable temperatures inside the superconducting state. This suggests a stronger impact of CO on SC and not the other way around (i.e. SC on CO). The complex interplay between these two phases was studied using several different techniques. For example, CDW was extensively studied in the $\text{YBa}_2\text{Cu}_3\text{O}_{6+\delta}$ system [87] as a function of magnetic field and temperature. The magnetic field effect is to suppress the SC T_c of the system, thus enhancing the “strength” of the two-dimensional CDW at lower temperatures. Interestingly, at fields higher than 15 T a new three-dimensional CDW sets in with the same in-plane incommensurability as the 2D CDW but at different ℓ component [88–90]. Thus the magnetic field is both suppressing the superconductivity and pinning the 3D CDW order along the out of plane direction. In a similar fashion, we used a hydrostatic pressure to suppress the SC and reveal the CO in Pt doped IrTe_2 . This Chapter is organized as follows: first an introduction to the $\text{Ir}_{1-x}\text{Pt}_x\text{Te}_2$ system is presented; afterwards the resistivity and hard x-ray diffraction experiments under hydrostatic pressure are discussed; and finally we propose and discuss different models for the interplay between SC and CO in this system.

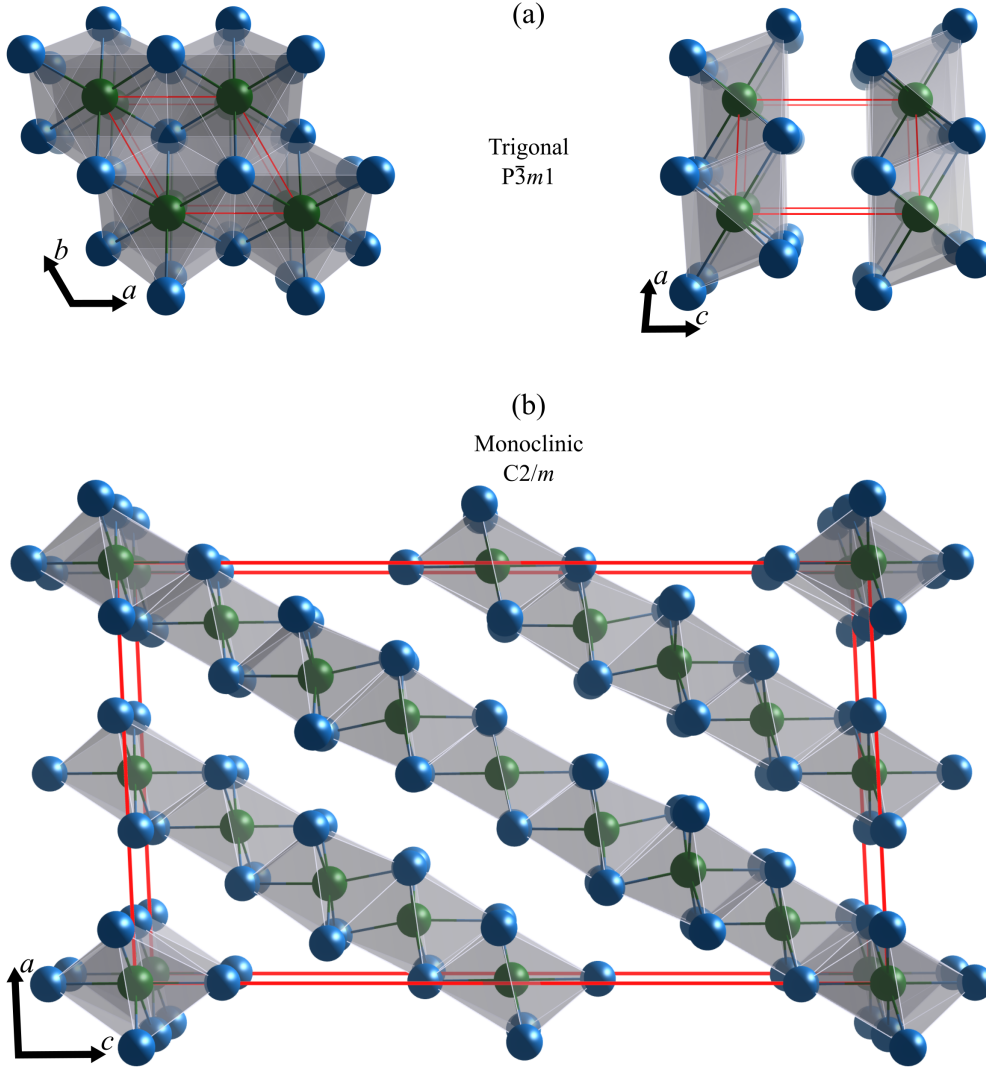


FIGURE 4.1: Crystal structure of IrTe_2 at high (a) and low (b) temperatures is presented. Blue (green) balls represent Te (Ir) atoms while the red solid line indicates the unit cell. Figure obtained using *VESTA* [13].

4.1 State of the Art

IrTe_2 has attracted considerable attention due to the large spin-orbit coupling in the Ir site. Moreover, a structural transition characterized by a considerable Fermi surface reconstruction occurs at $T_{s1} = 280$ K [91, 92]. The group symmetry is changing from the trigonal $P\bar{3}m1$ at high temperature to a monoclinic $C2/m$ at T_{s1} . As can be seen in Fig. 4.1, IrTe_2 is a layered system with edge-sharing octahedra forming sheets which stack along the c axis at high temperature and are tilted, with respect to the latter, at low temperature.

The structural transition is also accompanied by a development of a charge order of type $(\delta, 0, \delta)$, which at T_{s1} has $\delta = 1/5$ and transits to $\delta = 1/8$ under $T_{s2} = 200$ K. Upon

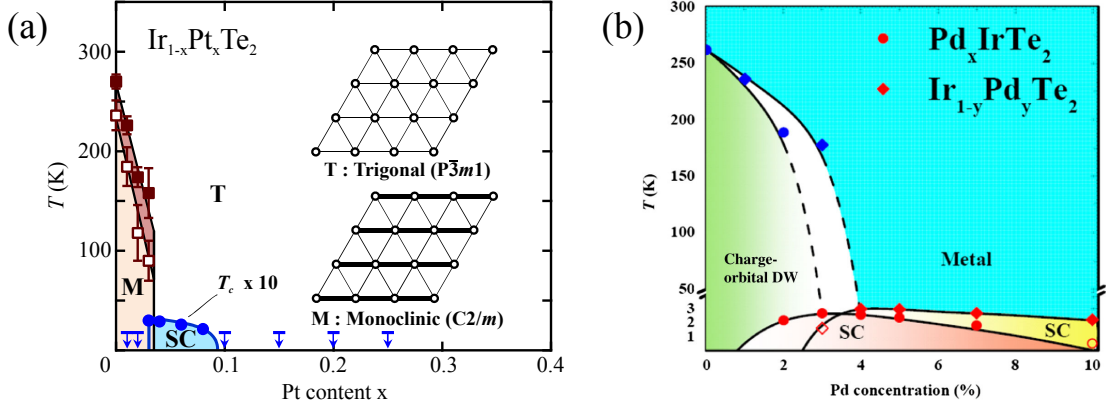


FIGURE 4.2: Phase diagram with Pt (a) and Pd (b) substituted IrTe_2 . SC stands for superconductivity. Figures adapted from Refs. [10] and [11] respectively.

warming (from low temperature) the $\delta = 1/5$ phase is suppressed but the ($\delta = 1/8$) CO still melts at T_{s1} . Furthermore, at the surface, a $\delta = 1/6$ phase was observed by a scanning tunneling microscopy (STM) study, revealing a similar hysterical behavior [93]. STM also revealed that this CO is characterized by a dimer formation, which was identified to be a pair of $\text{Ir}^{3+}-\text{Ir}^{3+}$. Following the same principle the bulk CO was explained as the alternation of electron-rich and electron-depleted (at the dimer site) regions. This mechanism was implemented in the Fermi-surface calculations and a reasonable agreement with experiments was obtained [94]. Nevertheless, a complete understanding of this peculiar charge order is yet to be accomplished. For example, a formation of CO should be followed by an opening of a gap at, or in the vicinity of, the Fermi surface. To date, only a suppression of the spectral weight was observed with optical and ARPES studies [94–96].

To conclude this introduction on the system, a phase diagram is presented in Fig. 4.2. It can be seen that, a Pt [10] or Pd [11] substitution in the Ir site induces a suppression of the structural (and CO) transition up to a critical concentration x_c after which superconductivity emerges. Similar behavior is also present (not shown) in the Cu intercalated IrTe_2 samples [97]. From such a phase diagram, we can conclude that a competition between the charge order and superconductivity is present in this systems.

4.2 Resistivity Measurements

The changes in crystal structure and the occurrence of the charge order are also detectable with resistivity measurements.¹ As shown in Fig. 4.3(a), IrTe_2 presents a big jump in the resistivity curve revealing a first order phase transition in the system.

¹Performed by L. Yang, D. Destraz., E. Martino, Y. Chen, C.Y. Guo, H.Q. Yuan, A. Pisoni, P. Matus, L. Forró and H. M. Rønnow.

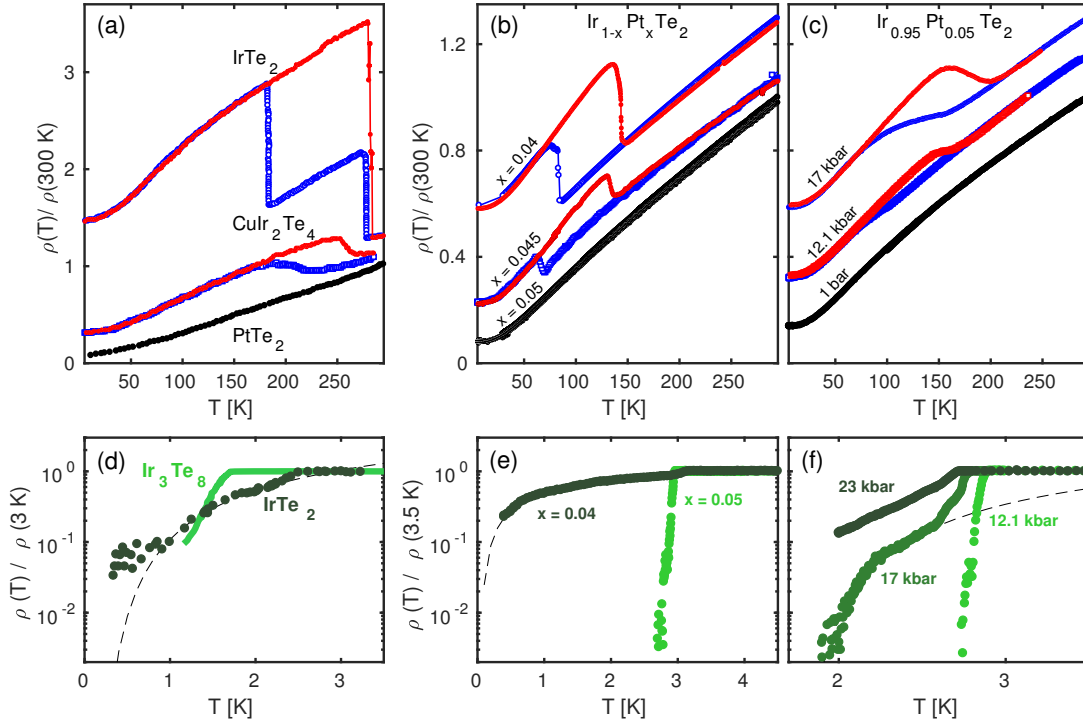


FIGURE 4.3: Warming (red) and cooling (blue) resistivity curves for IrTe_2 (adapted from Ref. [99]) and related materials CuIr_2Te_4 and PtTe_2 (adapted from Ref. [100]). Similar curves for $\text{Ir}_{1-x}\text{Pt}_x\text{Te}_2$ samples are presented as a function of doping x (b) and hydrostatic pressure (c) for $x = 0.05$. Broader step-like transition is due to the influence of the pressure cell. Low temperature data, obtained in the same conditions as in (a), (b) and (c), are presented in (d), (e) and (f), respectively. Note the logarithmic scale and normalization for the y axis in (d-f). In (d), data for IrTe_2 and Ir_3Te_8 are adapted from Refs. [96, 101]. Dashed lines in (d-f) are guides to the eye only.

These peculiar properties of the compound can be associated with both charge order and the structural transition. From the sole resistivity curves it is not possible to attribute which one is the driving mechanism. On the other hand, we can notice a hysteretical behavior when the warming and cooling curves are overlapped. Notably, the step-like anomaly occurs at characteristic temperatures close to the previously introduced T_{s1} and T_{s2} . Since T_{s2} is related to the CO, we might think that this is the driving "force". A similar resistivity anomaly is also present in the isostructural related compound CuIr_2Te_4 but absent in PtTe_2 [see Fig. 4.3(a)]. Although a charge order model was proposed for CuIr_2Te_4 [98], no direct evidence of it was yet reported.

The anomaly in the resistivity was further investigated as a function of doping and hydrostatic pressure in $\text{Ir}_{1-x}\text{Pt}_x\text{Te}_2$. As shown in Fig. 4.3(b) the hysteretic loop is present up to $x = 0.045$ but completely absent in the superconducting sample [see Fig. 4.3(e)] with $x = 0.05$. Only after a 12.1 kbar hydrostatic pressure is applied to the $\text{Ir}_{1-x}\text{Pt}_x\text{Te}_2$ with $x = 0.05$ sample, the anomaly in the resistivity is recovered [see Fig. 4.3(c)]. With increasing doping of Pt content x and decreasing pressure on

the $\text{Ir}_{1-x}\text{Pt}_x\text{Te}_2$ with $x = 0.05$, we observe two main similarities: (i) the size of the hysteretical loop is getting smaller and shifting towards lower temperatures; and (ii) the sample is undergoing a superconducting transition at low temperatures ($\lesssim 3$ K) once the resistivity anomaly is largely suppressed. To understand the behavior in the point (i) we conducted a hard X-ray diffraction experiment on $\text{Ir}_{1-x}\text{Pt}_x\text{Te}_2$ with $x = 0.04$ and $x = 0.05$, which will be presented in the next section. Concerning point (ii), we will propose a mechanism explaining the broadening of the SC transition in the conclusive part of this Chapter.

4.3 Hard X-ray Scattering Experiment

A hard x-ray (100 keV) study was performed at the P07 beamline at PETRAIII in DESY (Hamburg, Germany). Both the $\text{Ir}_{1-x}\text{Pt}_x\text{Te}_2$ with $x = 0.04$ and $x = 0.05$ samples were studied on a triple-axis diffractometer using a closed-cycle cryostat ($T_{\min} \sim 20$ K). Hydrostatic pressure was applied by means of a piston-type pressure cell. For more detail, please refer to Chapter 2. The data are presented in reciprocal lattice units (r.l.u.) and a hexagonal notation is used with $a = b = 3.95$ Å and $c = 5.38$ Å.

As already presented previously, we performed the diffraction experiment on the superconducting $\text{Ir}_{1-x}\text{Pt}_x\text{Te}_2$ with $x = 0.04$ and the superconducting (at atmospheric pressure) $\text{Ir}_{1-x}\text{Pt}_x\text{Te}_2$ with $x = 0.05$ samples. Due to the resistivity anomaly in the $x = 0.04$ system, a structural or CO transition (or both at the same time) is expected, as in the parent compound IrTe_2 . In Fig. 4.4(b) a scan along the reciprocal $(h, 0, h)$ direction is shown for the $x = 0.04$ sample. Charge order with $\delta = 1/5$ commensurability is found. It is also observed that the $(m\delta, 0, m\delta + k)$ reflections with $k = 1, 2, 3$ are much weaker than for $k = 0$ (with $m = 1, 2, 3, 4$). Since the diffracted intensity I is proportional to the scattering vector \mathbf{Q} scalar the atomic displacement \mathbf{u} (see Eq. 3.3), it follows that the charge modulation is along the $[101]$ direction as in IrTe_2 . Upon warming, the CO is almost completely melted at 160 K. A little signal is still detectable at the two strongest scattering vectors $(1/5, 0, 1/5)$ and $(2/5, 0, 2/5)$, as shown by the solid black line in Fig. 4.4(b). Nonetheless, this is consistent with the characteristic temperatures for the step-like features [Fig. 4.3(b)] in the resistivity measurements. On the other hand, no evident structural transition is observed. In the 2θ scan (obtained by varying the scattering angle, in order to fulfill the Bragg condition for different lattice constants) no peak splitting of the Bragg peak [see inset of Fig. 4.4(b)] is detected, at the base temperature (20 K). However, indications of peak splitting (not shown) are observed in the orthogonal (ω) scan under 160 K. Most likely, the structural transition is present but not detected. Some domains can be suppressed and no peak splitting

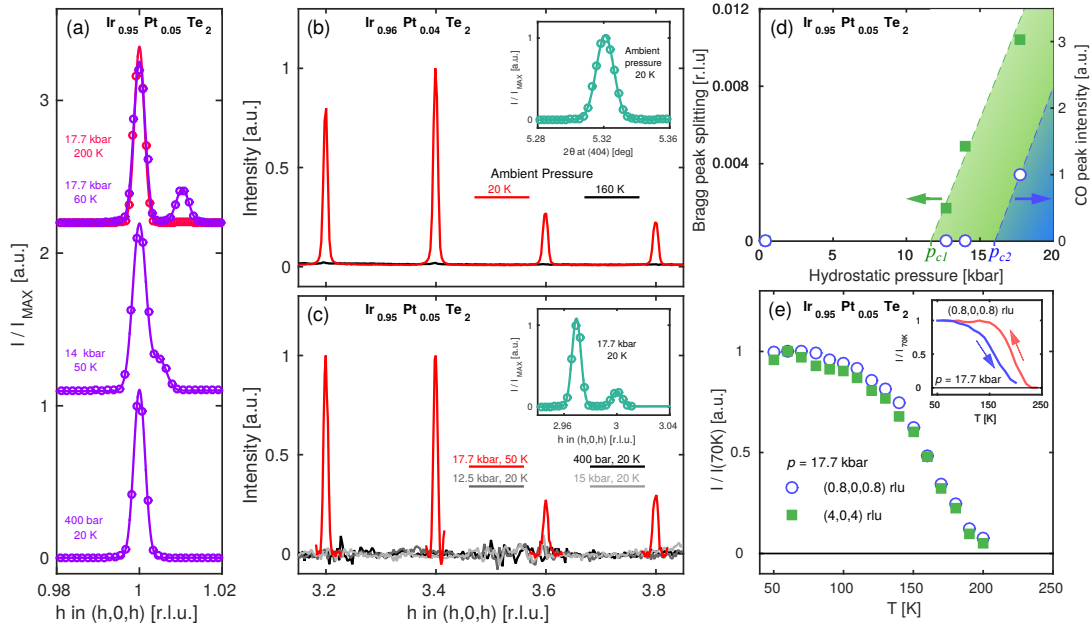


FIGURE 4.4: X-ray scattering data for $\text{Ir}_{1-x}\text{Pt}_x\text{Te}_2$. In (a) the (101) Bragg reflection is presented for $x = 0.05$ sample as a function of hydrostatic pressure and temperature, as indicated. Solid lines are fit to the data using two (one for 400 bar) Gaussian functionalities. $\text{Ir}_{1-x}\text{Pt}_x\text{Te}_2$ with $x = 0.04$ diffraction intensity (at ambient pressure) along the [101] axis, at 20 (red) and 160 K (black), are presented in (b). Similar data, at low temperature, for $\text{Ir}_{1-x}\text{Pt}_x\text{Te}_2$ with $x = 0.05$ are presented in (c) for different hydrostatic pressures, as indicated. Insets in (b) and (c) depict the scans over the reference (for charge order) Bragg peak, for the two compositions as indicated. In (d) the splitting of the (101) reflection and charge order intensity [extracted from data as in (a) and (c)] are presented as a function of applied pressure. Temperature dependence (cooling) of the short-axis Bragg signal and CO intensities are shown in (e), alongside with the warming and cooling curves, for CO only, presented in the inset.

is observed. The structural transition for this composition is expected to occur at the same temperature as for the charge order, similar to the undoped IrTe_2 .

Surprisingly, cooling the sample down to 20 K, no CO with $\delta = 1/8$ was detected. This signifies that the ground state for the $\text{Ir}_{1-x}\text{Pt}_x\text{Te}_2$ with $x = 0.04$ is different from the parent compound and that there is a transition doping at which the $\delta = 1/8$ CO disappears. While this assumption still has to be confirmed experimentally, the main conclusion of this first part is that a strong charge order is present in the non-superconducting sample. To reveal whether the opposite (i.e. no CO in the SC sample) is true, we measured the $\text{Ir}_{1-x}\text{Pt}_x\text{Te}_2$ with $x = 0.05$ sample.

A systematic study of $\text{Ir}_{1-x}\text{Pt}_x\text{Te}_2$ with $x = 0.05$ sample was performed under several hydrostatic pressures. The lowest adopted pressure is 400 bar and we consider it to be equivalent to the ambient pressure since no particular change in the resistivity is observed up to about 12 kbar [see Fig. 4.3(c,f)]. Following the (101) Bragg peak [Fig. 4.4(a)] it is clear that upon increasing the pressure, firstly a shoulder appears at 14 kbar and an

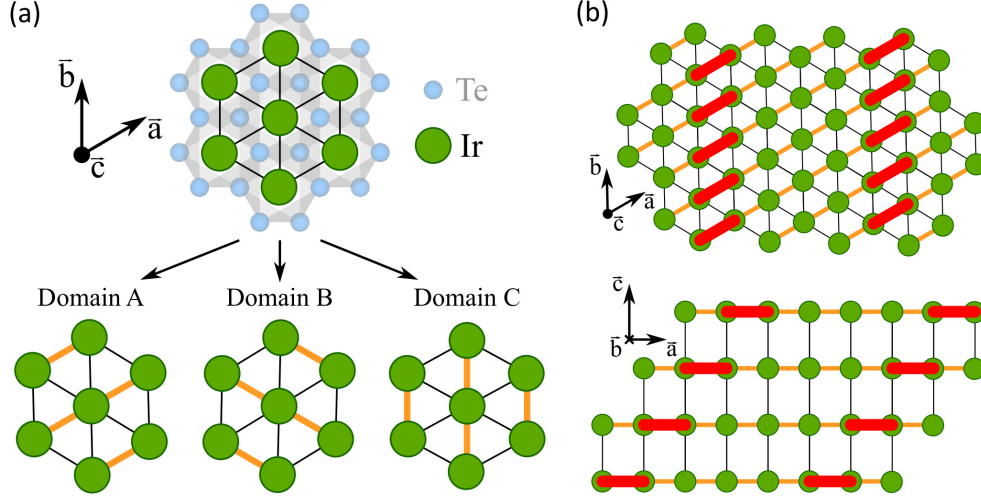


FIGURE 4.5: Simplified version of the trigonal-to-monoclinic transition is schematically shown in (a) along the (001) projection of the hexagonal IrTe_2 crystal structure. Different domains are obtained due to the formation of a short axis (thick orange bond) along the \vec{a} , \vec{b} and $\vec{a} - \vec{b}$ directions. For each domain a dimerization (thick red line) of Ir atoms is proposed in (b) as a model for the charge order found in $\text{Ir}_{1-x}\text{Pt}_x\text{Te}_2$ at atmospheric ($x = 0.04$) and hydrostatic applied pressure ($x = 0.05$).

additional peak is completely developed at about 17.7 kbar. This structural transition occurs at a critical pressure p_{c1} , which we estimate to be 11.5 kbar. No detailed study on the symmetry of this transition was performed but our data are consistent with the monoclinic $C2/m$ space group. We thus assume that the lowering of the crystal symmetry is the same as for the parent compound.

Concerning the charge order [Fig. 4.4(c)], commensurate reflections with $\delta = 1/5$ are found only at the highest applied pressure of 17.7 kbar and only with respect to the new (short-axis) Bragg reflection, suggesting its uniaxial nature. From this a critical pressure p_{c2} for the CO, is estimated to be 16 kbar. Even though the exact values still have to be found with further examination, it is clear that $p_{c1} < p_{c2}$ for $\text{Ir}_{1-x}\text{Pt}_x\text{Te}_2$ with $x = 0.05$ system. This separation in two distinct phases [Fig. 4.4(d)], suggests that the structural transition is a prerequisite for the appearance of the charge order and not the other way around. This intimate relation is further confirmed by the temperature dependence of the scattering intensity of the $(1 - \delta, 0, 1 - \delta)$ and monoclinic (404) reflections [Fig. 4.4(e)]. Upon cooling, indeed the Bragg- and CO-peak intensities overlap on each other and disappear at about 200 K. In addition, a hysteresis loop of the CO-peak intensity [see inset of Fig. 4.4(e)] is found between the warming and cooling curves, as in the resistivity measurements. Even though the resistivity anomaly is no more a well defined step-like jump (probably due to the more complicated set-up), the characteristic transition temperatures agree well with the diffraction results. Unfortunately no warming-curve of the Bragg peak is available but it is reasonable to conclude that it will follow a

hysteretical behavior. In addition, it is evident that the main reason of the resistivity anomaly at about 12 kbar [Fig. 4.3(b)] is the structural transition, as no evidence of charge order is found [Fig. 4.4(c)]. The fact that the area of the loop (in the resistivity curves) is growing with pressure, suggests that the appearance of the CO also contributes to this anomaly. A simultaneous x-ray diffraction and resistivity measurement might resolve this issue.

A closer examination of Figs. 4.4(b) and 4.4(c) reveals that the modulation of the charge peaks is almost identical. The slight difference might be the result of the background subtraction which was necessary for the pressure experiment on $\text{Ir}_{1-x}\text{Pt}_x\text{Te}_2$ with $x = 0.05$ sample and arising from the powder-ring reflections from the pressure cell. Since the scattering structural factor is strongly dependent on the symmetry, we conclude that the very same charge order is observed for the two compounds. Furthermore, having such a close similarity for two different Pt contents and at two different pressures, we can extend this picture by assuming that this charge order is of the same kind as for the parent compound IrTe_2 . We thus propose a similar mechanism for the charge order, illustrated in Fig. 4.5 and involving the formation of $\text{Ir}^{3+}-\text{Ir}^{3+}$ dimers. In Fig. 4.5(a) it is shown that from a hexagonal structure it is possible to obtain three monoclinic domains, in which one of the lattice parameter is shorter than the other. This results in a twinned sample which explains the presence of two Bragg reflections in Fig. 4.4(a). Each of this domains will allow (and induce) the formation of the charge order. We saw that the CO is closely related to the shorter lattice parameter [i.e. higher h in $(h, 0, h)$] and thus a dimerization mechanism is proposed only along this direction. As shown in Fig. 4.5(b) this model results in dimer planes cutting the crystal with a non-zero angle with respect to the c axis.

4.4 Discussion & Conclusions

To conclude, we have observed that a $\delta = 1/5$ charge order is present for the $\text{Ir}_{1-x}\text{Pt}_x\text{Te}_2$ with $x = 0.04$ at atmospheric pressure and that no $\delta = 1/8$ phase was detected down to 20 K. A pressure induced structural transition and the formation of a $\delta = 1/5$ charge order is obtained at two distinct pressures p_{c1} and p_{c2} respectively. Since $p_{c1} < p_{c2}$, a monoclinic phase is necessary for the appearance of CO. Having collected all this information, we propose a $p - T - x$ phase diagram in Fig. 4.6. Further studies are needed to confirm and precisely draw the boundaries of the different phases for this compound. In addition, a study on the Pd-doped sample would be of main importance to find similarities and differences between the two compounds and thus gain more insight into the physics behind these phenomena.

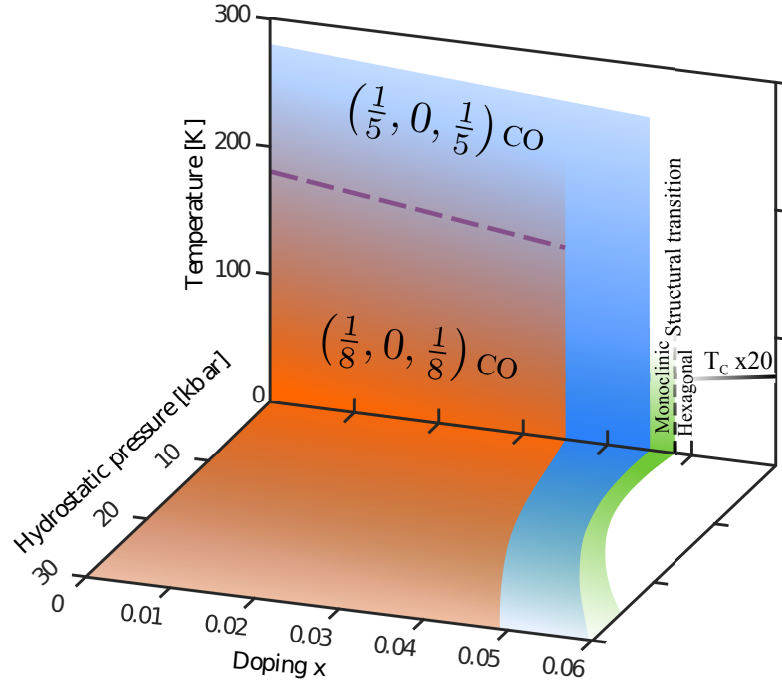


FIGURE 4.6: A hydrostatic pressure *vs.* temperature *vs.* doping x phase diagram is proposed for the $\text{Ir}_{1-x}\text{Pt}_x\text{Te}_2$ system.

Some final remarks are needed with respect to the low-temperature behavior for the pressure-applied $\text{Ir}_{1-x}\text{Pt}_x\text{Te}_2$ with $x = 0.05$ sample. Namely, a competition between the charge order and superconductivity is observed. This can be seen from Figs. 4.7, which were constructed from data as shown in Figs. 4.3(c) and 4.3(f). In fact, the superconducting transition remains sharp after the structural transition occurs at about 12 kbar, but becomes broader once the charge order is developed for $p > p_{c2}$. The onset of the transition remains fairly the same at about 3 K but the region where zero resistivity is observed becomes (instrumentally) unavailable.

This broadening of the superconducting phase can result from the following mechanisms:

- Inhomogeneities:
 - pressure
 - chemical
 - electronical
- Granular superconductivity
- Low-dimensional superconductivity

Pressure inhomogeneities, for example, can be a result of a solidification of the transmitting liquid inside the pressure cell, creating a non uniform strain on the sample. We notice, however, that the maximum applied pressure was under the solidification limit

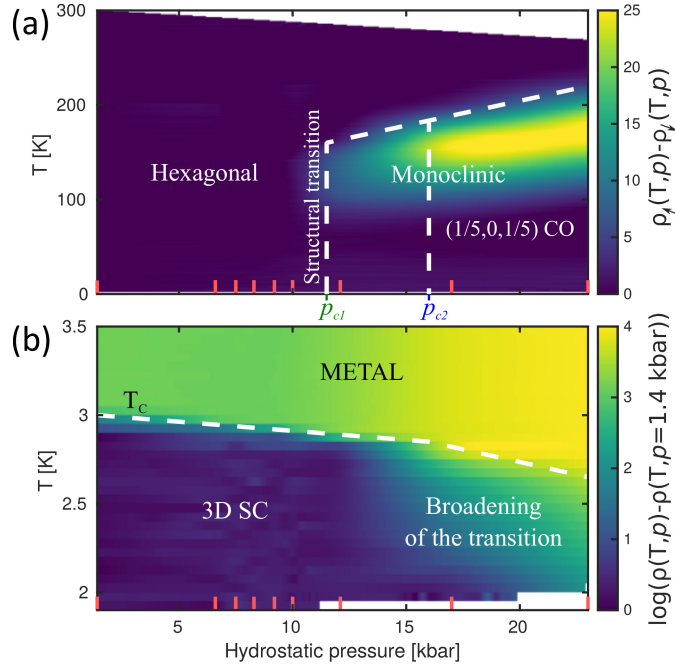


FIGURE 4.7: False-color map plot of the difference between the warming and cooling resistivity curves, as a function of hydrostatic pressure and temperature, for $\text{Ir}_{1-x}\text{Pt}_x\text{Te}_2$ with $x = 0.05$ is presented in (a). A similar plot, but at low temperatures, is shown in (b) for the difference (in logarithmic scale) between the resistivity curves at a particular pressure and the minimum applied one.

of the Daphne oil. Furthermore, we observe similar broadenings both as a function of hydrostatic applied pressure and chemical substitution. Chemical inhomogeneities can also be excluded since a hydrostatic pressure should have no effect on the dopant disorder. As for the last point, also the electronic inhomogeneities could be responsible for the broadening, especially because they can be tuned by the doping content x and by the applied pressure. However, we can exclude the whole “Inhomogeneities” picture by the fact that a general disorder would produce a broad charge order reflection, which is in stark contrast with the observed resolution-limited signal.

For what concerns the granular superconductivity, this is characterized by regions which are superconducting separated (and thus surrounded) by a non superconducting ones. Within such a picture, it is natural to think that in our system the non superconducting part will be constituted by the monoclinic domain walls between different twins. Therefore, one needs to select a single-domain sample (or to detwin a multi-domain one) and to measure the magnetic (Meissner effect) and conducting properties. If the sample results superconducting and with a sharp transition, this would hint towards the granular superconductivity scenario. Unfortunately, this experiment is difficult to realize due to technical reasons: currently available samples are small (thin along the c axis) and fragile, resulting to be unapproachable to a detwinning (which by the way should be done *in situ* since $T_{s1} < 300$ K). On the other hand, we observe that for $\text{Ir}_{1-x}\text{Pt}_x\text{Te}_2$ with

$x = 0.05$ sample, under 12.1 kbar the superconducting transition is still sharp as much as for the lowest applied pressure [see Fig. 4.3(e)], but a monoclinic transition, and thus the formation of domain walls, has already occurred, as confirmed by the diffraction experiment [Fig. 4.4(a)]. Explaining the data within the granular superconductivity results to be non straightforward.

Finally, we discuss the two-dimensional superconductivity scenario which takes place within the Berezinskii – Kosterlitz – Thouless transition. Briefly, one can see [102, 103] that it is possible to approximately describe the resistivity drop below T_c by an exponential-type of function [see dashed line in Figs. 4.3(d-f)] of the form: $\rho(T) \propto e^{-b/\sqrt{t}}$, where b is a constant and $t = (T - T_{BKT})/T_{BKT}$ with T_{BKT} as a second-order temperature scale. This scenario is supported by the occurrence of the charge order, which as we saw is competing with superconductivity in this system. Indeed, the dimerization on the Ir site produces a local suppression of the density of states [91, 92, 104–106]. Therefore, it is plausible that superconductivity is suppressed inside these sheets [Figs. 4.5(b) and 4.5(c)], separating completely superconducting parts of the sample. Also in this case it is (experimentally) challenging to prove such a scenario, due to the above mentioned technical issues and the fact that the charge order runs along a non crystallographic high-symmetry direction. However, an experimental evidence of Berezinskii – Kosterlitz – Thouless transition would be of main interest.

Chapter 5

Damped Spin Excitations in $\text{La}_{2-x}\text{Sr}_x\text{CuO}_4$

Superconductivity is a phenomena characterized by zero-electrical resistivity and perfect diamagnetism, so-called Meissner effect. In 1911 superconductivity was observed, for the first time, in solid mercury by Heike K. Onnes [107]. Later on, many other compounds were found to be superconducting under a critical temperature T_c [see Fig. 5.1]. Depending on the particular type of superconductivity and the composition, these materials can be grouped in families. One of these families comes under the name of cuprates, because the active part is composed of copper oxide.

Cuprate superconductors are an interesting and exciting topic of solid state physics. The first high-temperature superconductor (HTS) was discovered in 1986 by J. Georg Bednorz and K. Alex Müller at Universität Zürich in a mixture of Ba–La–Cu–O system [108]. Later the 1987 Physics Nobel Laureates reported that actually $\text{La}_{2-x}\text{Ba}_x\text{CuO}_4$ is the superconducting compound with T_c of about 30 K [109]. Following, new compounds were discovered with higher transition temperatures, with the record T_c of 133 K for $\text{HgBa}_2\text{Ca}_2\text{Cu}_3\text{O}_{8+\delta}$ compound [110] discovered by Andreas Schilling in 1993 at Universität Zürich.

After 30 years [111], no microscopic description of HTS is found despite an enormous number of publications. Even though, enhancing the T_c is possible, for example, by epitaxial strain [28, 112] and hydrostatic pressure [27, 113], it is still under debate what is the pairing mechanism of Cooper pairs. Antiferromagnetic fluctuations are believed to be responsible but no direct evidence, as the isotope effect [114, 115] for phonon-mediated superconductors, is yet observed. On the other hand, an agreement on the d -wave symmetry of the gap [38] is reached, and it is believed that it is a universal property for cuprates. For these reasons, and for the presence of several other phenomena

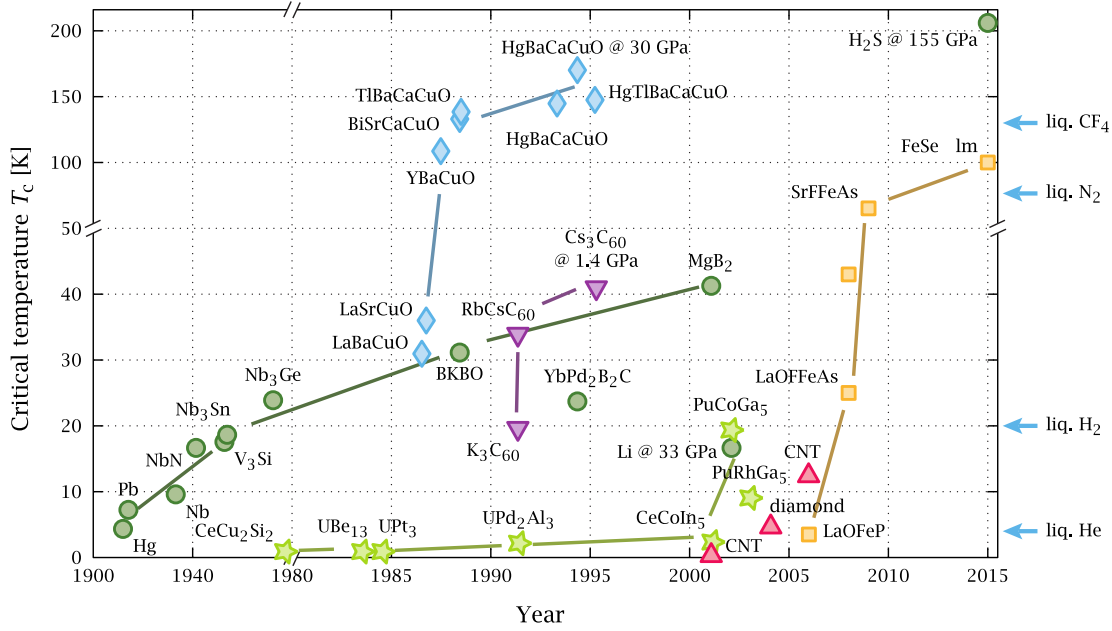


FIGURE 5.1: Transition temperature T_c for superconductivity as a function of discovery date of respective compounds. Cuprates are indicated with light blue diamonds. On the right are also indicated, by arrows, the condensation liquid-phase temperatures for gases as indicated. Figure from Ref. [118]

like the stripe order, the pseudogap region and the charge density wave, cuprates are still under intense research.

In this Chapter we will focus on bulk $\text{La}_{2-x}\text{Sr}_x\text{CuO}_4$ (LSCO) high-temperature superconductor [116] from a Resonant Inelastic X-ray Scattering point of view. A brief introduction on the cuprate physics, relevant to the present work, will follow on the next section. For a more complete overview, from experimental and theoretical insights, I suggest the reviews at Refs. [1, 3, 33, 117]. In Chapter 5 a similar RIXS work will be presented on thin films of the parent compound La_2CuO_4 .

5.1 State of the Art

Superconductivity is obtained once the compound is doped away from the insulating (charge-transfer) Mott state. Doping is achieved either by varying interstitial oxygen content [46] or by transition-metal substitution [33]. A typical temperature *vs.* doping phase diagram is shown in Fig. 5.2(a). Both electron and hole doping is possible. We will concentrate only on the hole-doped system $\text{La}_{2-x}\text{Sr}_x\text{CuO}_4$, for which a highest T_c of about 40 K is obtained once the Sr content x is about 0.15 [119].

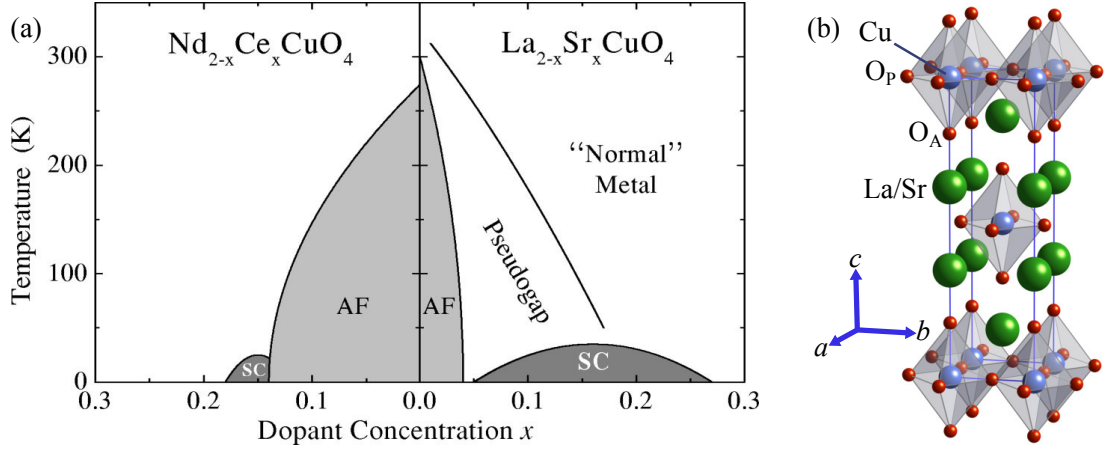


FIGURE 5.2: (a) Schematic representation for electron- (left) and hole-doped (right) cuprates. AF stands for antiferromagnetic, while SC for superconductivity. Figure adapted from Ref. [117]. (b) Tetragonal crystal structure of $\text{La}_{2-x}\text{Sr}_x\text{CuO}_4$, with $a = b \cong 3.8$ Å and $c \cong 13.2$ Å. Two different oxygen sites are indicated as O_P and O_A , having planar and apical coordination. Solid blue line indicated the tetragonal unit cell. Figure obtained using *VESTA* [13].

$\text{La}_{2-x}\text{Sr}_x\text{CuO}_4$ presents a typical perovskite-type of crystal structure with superconducting CuO_2 layers separated by La_2O_2 layers [see Fig. 5.2(b)]. At room temperature the compound presents a tetragonal (Bmab) structure if $x > 0.1$, below which it is orthorhombic ($F4/mmm$) [120]. This structural transition is both temperature and doping dependent, resulting in an orthorhombic phase inside the superconducting dome. Being a layered system, with a small coupling between the CuO_2 layers, it is a quasi-two-dimensional system, as confirmed by resistivity and Angle Resolved Photoemission Spectroscopy (ARPES) studies [117, 121]. Nevertheless, this small coupling has an important impact on the superconducting properties. Indeed, a higher T_c is obtained, for example, in $\text{YBa}_2\text{Cu}_3\text{O}_{6+\delta}$ system (92 K) which is a double layer compound. On the other hand, a similar T_c is obtained for the single layered $\text{HgBa}_2\text{CuO}_{4+\delta}$ (Hg1201) at about 90 K [122]. It is important to note, that contrary to the Hg1201 system, LSCO presents a tilting of the CuO_6 octahedra in the orthorhombic phase. Thus both in- and out-of-plane structural characteristics are different.

A simple valency analysis can give us an important information. In fact, if considering La_2CuO_4 , one finds that it is charge-neutral as La is trivalent and Cu is bivalent. On the other hand, the CuO_2 layers possess a net charge of -2 , and of course the La_2O_2 layers $+2$. Thus La_2O_2 acts as a charge reservoir to the CuO_2 planes. Once the system is doped, La^{3+} atoms are substituted by Sr^{2+} which in turn takes two electrons from the superconducting layers. Since there are two CuO_2 layers inside a unit cell, we can see that the number of holes (doping p) per copper plane is equivalent to the Sr content x .

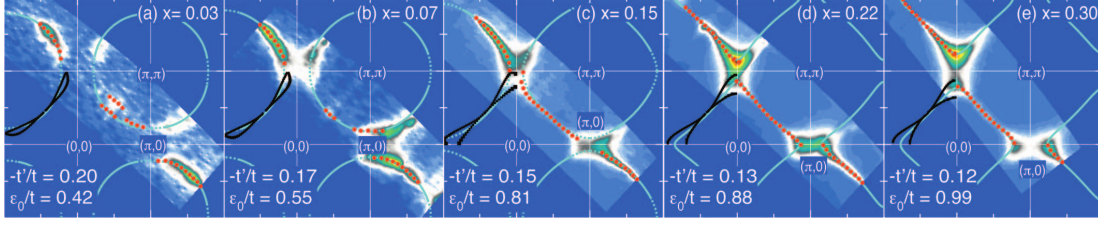


FIGURE 5.3: Fermi surface topology of $\text{La}_{2-x}\text{Sr}_x\text{CuO}_4$ as a function of doping x . Solid blue lines are fit to the data using a single-band tight-binding model. The outputs from the fit are shown in the lower left corner (t and t' , and ϵ_0 are the first- and second-neighbor hopping integrals, and chemical potential respectively). Solid black lines are LDA band-structure calculations for $k_z = 0$. Figure adapted from Ref. [36].

As already mentioned, once the superconductivity occurs a $d_{x^2-y^2}$ gap Δ , of the form $\Delta_0 (\cos k_x + \cos k_y)$, opens at the Fermi level E_F . Here k_x and k_y are the k -vectors inside the Brillouin zone. From this equation, one can see that a node (point at which the gap changes sign) occurs along $(k_x, k_y = \pm k_x)$ and that the maximum gap is along $(\pm k_x, 0)$ and $(0, \pm k_y)$. From this the so-called nodal and antinodal directions are defined, which correspond to Cu-Cu and Cu-O-Cu bond directions respectively.

For temperatures $T > T_c$ and outside the Mott insulating state [see Fig. 5.2(a)], the system is metallic [123], with only one band (with strong $d_{x^2-y^2}$ character [124]) crossing the Fermi level. Nevertheless, underdoped $\text{La}_{2-x}\text{Sr}_x\text{CuO}_4$ (as much as other hole-doped cuprates [117]), present a partial gap at the antinodal direction [125]. The so-called “pseudogap” is present up to a, strongly doping dependent, temperature T^* [126]. In fact, at the overdoped side of the superconducting dome the pseudogap vanishes at a critical doping x^* . At $T > T^*$, the resistivity is linearly temperature dependent and the system is called “strange metal”. Once the pseudogap sets in below T^* , the resistivity shows an upturn (as in LSCO [127]) or a downturn (as in YBCO [128]) and a “bad metallic” behavior appears. The origin of this phenomena, and how/if it is related to the superconductivity, is still under debate [129]. Additionally the Fermi surface itself has a doping dependence as shown in Fig. 5.3. On the strongly underdoped side it is hole-like, closing around the high-symmetry M point $[(\pi, \pi)]$, with a cylindrical shape. With increasing doping it evolves and becomes diamond shaped on the overdoped side, closing around the Γ point $[(0, 0)]$ and having an electron-like character.

To quantify this evolution, a common method is to fit the Fermi surface using a single-band tight binding model. Thus, by fitting the data, it is possible to extract the hopping integrals t , t' and t'' . In fact one can derive the following: $\epsilon_k = \epsilon_0 - 2t (\cos k_x a + \cos k_y a) - 4t' \cos k_x a \cos k_y a - 2t'' (\cos 2k_x a + \cos 2k_y a)$. Here ϵ_0 is the chemical potential. To simplify the fit it is common to assume $-t''/t = 1/2$. Yoshida *et al.* adopted this model using $t = 0.25$ eV [36] as a fixed parameter, thus extracting $-t'/t$ and ϵ_0/t from the fit.

The result is that $-t'/t$ is 0.2 for $x = 0.03$ and decreases towards 0.12 for $x = 0.3$ (see Fig. 5.3). For $\text{La}_{2-x}\text{Sr}_x\text{CuO}_4$ with $x = 0.12$ it thus results that $-t'/t \cong 0.15$.

Considering just the $d_{x^2-y^2}$ band, it was shown that the $d_{3x^2-y^2}$ band (d_{z^2} for simplicity) can have a non negligible contribution to the in-plane hopping terms [121, 124, 130, 131]. This two-band model has a relevant effect on the hopping integrals for the more orthorhombic compound, which can be quantified by $t_r = (t' + t'')/t$. Indeed, it is found that for LSCO $t_r = 0.14$ and 0.35 , using single- and two-band models respectively. On the other hand, this quantity varies little for the most tetragonal single-layer cuprate Hg1201, going from 0.37 to 0.41 . This can be explained by considering $\Delta E = E_{x^2-y^2} - E_{z^2}$, which was calculated to be 0.91 and 2.19 eV for LSCO and Hg1201 respectively. As a consequence a small hybridization between the $d_{x^2-y^2}$ and d_{z^2} bands does not have a strong impact on t_r for Hg1201 system. Notably, adopting the two-band model, the difference in t_r reduces considerably for the two compounds and it is roughly 0.4 .

Another important overview comes from band-structure calculations. In fact it is observed that, in order to reproduce the experimental evidence, a single-band model is not enough, even if just the low-energy part of the spectrum is considered [1]. For this reason a three-band model was adopted, in which also the p_x and p_y oxygen orbitals were taken into account [132]. In this calculations the undoped La_2CuO_4 compound was correctly identified as a charge-transfer Mott insulator. It results thus evident that a single-band model is not a correct approximation to describe the single-layer cuprate physics.

As already anticipated, one of the most debated questions is about the pairing superconducting mechanism. Due to the vicinity of the superconducting dome to the Mott state, antiferromagnetic pairing mechanism was proposed. Within this theory antiferromagnetic spin fluctuations are responsible for the formation of Cooper pairs [133]. However, a controversy arises due to the fact that in a Fermi liquid only ferromagnetic exchange interactions are possible [134]. To this end, spin excitations were studied both by means of neutron scattering [33] and more recently with RIXS [77].

Neutron scattering studies are concentrated near the antiferromagnetic Brillouin zone center (π, π) . Here it was found that while the excitations in La_2CuO_4 can be described by the spin-wave theory, for the doped samples a crossing between the magnon dispersion occurs, forming the so called “hour-glass” [66]. This transition of the shape of the excitations is smooth as a function of doping. Indeed, a decrease of E_c (the energy at which the crossing occurs) is observed with decreasing the doping of the system. Another interesting aspect is that the high-energy part is commensurate, converging towards (π, π) high-symmetry point. Contrary, the low-energy part is incommensurate, converging towards the static stripe-order reflections [44]. These type of excitations are

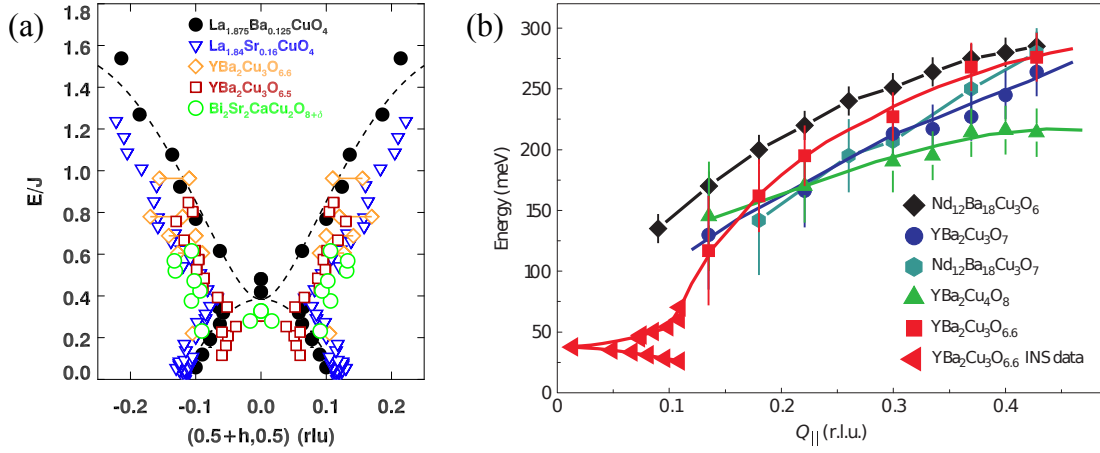


FIGURE 5.4: The so-called hour-glass dispersion, measured with neutron scattering near the antiferromagnetic Brillouin-zone center, is shown in (a), for compounds as indicated. Adapted from Ref. [135]. In (b), antinodal spin-excitation dispersion, measured along the antinodal direction with RIXS, are shown for compounds as indicated. Adapted from Ref. [77].

found in several cuprate system [135] as can be seen in Fig. 5.4(a) but not for all of them a stripe order was observed. Furthermore, the low-energy excitations (see Fig. 1.4) exhibit a gap once the superconducting state is formed [35]. Roughly linear relation between the size of the gap and the optimal-doping T_c is found if considering LSCO, YBCO and BSCCO [33]. It is thus natural to ask whether these excitations are relevant for the cuprate problem.

Besides the low-energy part, also the high-energy spin excitations received a considerable attention. For La_2CuO_4 , where an electronic gap of about 2 eV is present, only spin excitations are present in the relevant part of the spectra. Thus a spin-only Hamiltonian can be drawn and the resulting spin-wave model can be used to fit the dispersion of the magnons [82–84]. For $\text{La}_{2-x}\text{Sr}_x\text{CuO}_4$, instead, a maximum gap of about 50 meV is present in the superconducting state [38]. Thus, the spin excitations are damped due to mobile carriers. These paramagnons were studied in several cuprate systems, along the antinodal direction, by means of RIXS [77]. However, no relevant evolution has been observed [Fig. 5.4(b)] despite a big variation of superconducting transition temperatures.

In the following sections we will address a RIXS study of the (high-energy) spin excitations in $\text{La}_{2-x}\text{Sr}_x\text{CuO}_4$ with $x = 0.12$ and draw the conclusions relevant to this system.

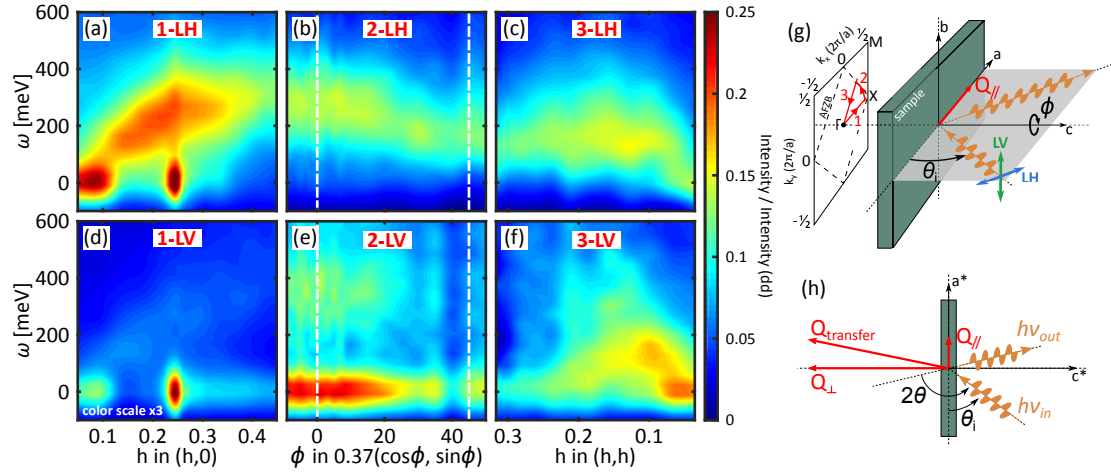


FIGURE 5.5: Color maps in false color of intensity of RIXS spectra for different momentum along the antinodal (a), azimuthal (b) and nodal (c) directions, for incident linear horizontal (LH) light polarization, are presented. Similar data but with linear vertical (LV) light are shown in (d), (e) and (f) respectively. Scattering geometry, as much as the path inside the Brillouin zone, is presented in (g) and (h).

5.2 Results: Paramagnons in $\text{La}_{2-x}\text{Sr}_x\text{CuO}_4$

We have studied, by means of RIXS, the paramagnon excitations in $\text{La}_{2-x}\text{Sr}_x\text{CuO}_4$ with $x = 0.12$ ($T_c = 27$ K) for a large set of momentum transfer. This work was performed at ADRESS beamline at Swiss Light Source (SLS) in Switzerland. The scattering angle was kept fixed at 130° and both linear horizontal (LH) and linear vertical (LV) incident light were used in a grazing out geometry, as schematically represented in Fig. 5.5(g,h). With this geometry, single-spin-flip magnetic excitations are observed only for incident LH light polarization [77]. Consequently, no outgoing light polarization analysis was performed. Note that LH and LV correspond to π and σ polarizations, with respect to the scattering plane [gray section in Fig. 5.5(g)]. The initial alignment of the sample was done *ex situ* using a Laue diffractometer. Sample cleaving was done, using the standard top-post procedure, in order to obtain a clean flat surface. Sample cleaving and measurements were performed at the Ultra High Vacuum (UHV) conditions at pressures better than 10^{-8} mbar. Incident light energy was tuned to the Cu L_3 edge (933 eV) and a resulting 132 meV energy resolution was obtained at the detector stage. Momentum transfer resolution was about 0.01 \AA^{-1} . The experiment was performed at a base temperature of 20 K inside the low temperature orthorhombic (LTO) phase of the sample. Nevertheless, a tetragonal notation is adopted, with $a \approx b \approx 3.78 \text{ \AA}$ ($c \approx 13.2 \text{ \AA}$). In-plane momentum transfer $Q = (h, k)$ is represented in reciprocal lattice units (r.l.u.) $2\pi/a$. The out-of-plane l component is neglected being $\text{La}_{2-x}\text{Sr}_x\text{CuO}_4$ a quasi-two-dimensional system.

In Fig. 5.5 color-map plots, of the the intensity of the acquired data, are presented along three different directions [shown schematically in (g)]. With the CARVING manipulator, available at the RIXS endstation, it was possible to change *in situ* the orientation of the sample, with respect to the incident beam. Thus, we could continuously scan the sample between the antinodal [Fig. 5.5(a,d)], nodal [(c,f)] and azimuthal [(b,e)] directions connecting the former two. Additionally, since the sample presents a CDW [136, 137], a careful alignment of the sample was possible using this reflection. In fact, along the antinodal direction, a strong elastic signal ($\omega = 0$) is observed [besides the one at specular condition at $Q = (0, 0)$], as can be seen in Fig. 5.5(a,d). The resulting incommensurability $Q_{CDW} = (\delta_1, \delta_2)$ is found to be $\delta_1 = 0.24(6)$ and $\delta_2 \cong \pm 0.01$, which is consistent with the literature.

The inelastic part of the spectrum (for LH light) presents a strong dispersion of the paramagnons along the antinodal and azimuthal directions [Fig. 5.5(a-b)], whereas along the nodal [(c)], these excitations are strongly damped and nearly non dispersive. For LV light, instead, no clear evidence of dispersion is observed [(d-f)]. In Fig. 5.6 raw data, with the fit, are presented along the antinodal (a-d), azimuthal (e-h) and nodal (i-l) directions. To fit the data a Gaussian and quadratic functionalities were used for the elastic line ($\sigma = 56$ meV) and dd -excitation background respectively. For the paramagnon excitation an antisymmetric Lorentzian function [77–79] was adopted (see Eq. 2.5). The resulting pole of the excitation is marked by the pink thick bar in Fig. 5.6 and presented along the three directions, as a function of momentum transfer Q , in Fig. 5.7(c-e). While the antinodal dispersion is about 300 meV, consistent with other cuprates [77], the nodal dispersion is softened of about 150 meV with respect to the latter. This effect, which is clearly evident in the raw data [Fig. 5.7(a,b)], has already been reported for overdoped LSCO [78] and Bi-based [138, 139] systems. Nevertheless, thanks to the azimuthal scan [Fig. 5.7(d)], the exact evolution of this softening is reported for the first time. The relevance of this result comes from a direct comparison with the magnon dispersion observed in La_2CuO_4 [82, 83]. In fact, La_2CuO_4 presents a less pronounced (≈ 50 meV) zone-boundary dispersion $E_{ZB} = \omega(1/2, 0) - \omega(1/4, 1/4)$. The three-dimensional topology of this effect is shown in Fig. 5.7(f,g), which is obtained with a Hubbard $t - t' - t'' - U$ model at strong coupling [84, 85]. An analytical solution, of the form $\omega = Z\sqrt{A^2 - B^2}$, can be obtained for this model. Here, Z being the quantum-fluctuation renormalization factor, is kept constant (neglecting the momentum dependence) and equal to 1.219 [84]. A and B terms are functions of t, t', t'' and U , for fixed momentum Q . For simplicity, we also adopt $-t''/t' = 1/2$ [36]. In addition, in order to compare directly the results for the two compounds, a fixed value for t was kept and equal to 0.43 eV, as obtained from experiments [140, 141] and LDA calculations [142]. Besides La_2CuO_4 and $\text{La}_{2-x}\text{Sr}_x\text{CuO}_4$ with $x = 0.12$, a fit to the magnetic-excitation

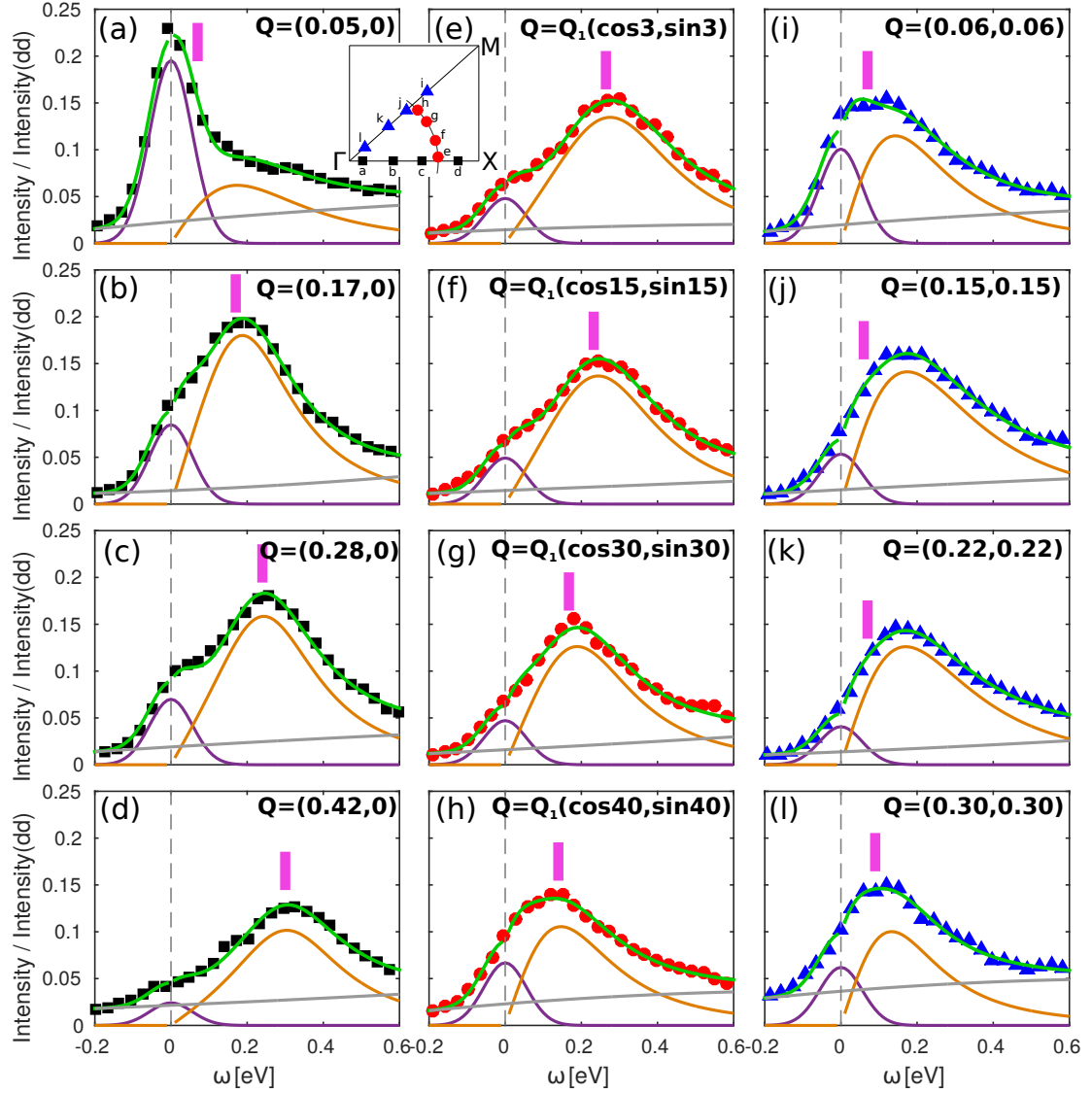


FIGURE 5.6: Raw RIXS spectra with the respective fit (solid green line) are presented along the antinodal (a-d), azimuthal (e-h) and nodal (i-l) directions, for (parallel) momentum transfer as indicated. Single components of the fit are also shown: elastic line (purple), paramagnon (orange) and background (gray). The pole of the magnetic excitation, as extracted from the fit is represented by the pink thin line (for further details see the main text). The position of each spectra within the Brillouin zone is indicated in the inset. In (e-h) $Q_1 = 0.37$ r.l.u.

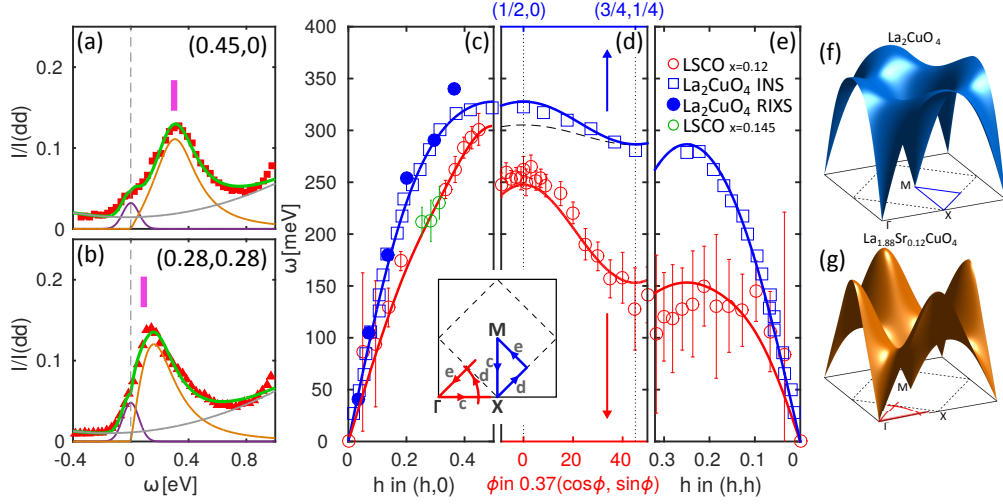


FIGURE 5.7: RIXS spectra of $\text{La}_{2-x}\text{Sr}_x\text{CuO}_4$ with $x = 0.12$ sample, with the respective fit, near the antinodal (a) and nodal (b) zone-boundary points. The pole of the excitation (pink mark in (a) & (b)) is extracted for each spectra and presented (red open circles) along the antinodal (c) and nodal (e) directions, alongside the azimuthal (d) connecting the first two as shown in the inset. Green open circles are from $\text{La}_{2-x}\text{Sr}_x\text{CuO}_4$ with $x = 0.145$ and are used to replace the $x = 0.12$ data near the charge order momenta (see text for further explanation). La_2CuO_4 data are also presented, as extracted from an inelastic neutron scattering study [83] (open blue squares) and from a RIXS study [80] (filled blue circles). Solid line through the data in (c-e) are fits using a Hubbard model (see text for further details) and are presented three-dimensionally, with the Brillouin zone, both for La_2CuO_4 (f) and $\text{La}_{2-x}\text{Sr}_x\text{CuO}_4$ with $x = 0.12$ (g).

dispersion was performed also on $\text{Bi}_2\text{Sr}_{0.99}\text{La}_{1.1}\text{CuO}_{4+\delta}$ (Bi2201) [143] ($E_{ZB} \approx 75$ meV). The quality of the fit can be appreciated in Figs. 5.7(c-e) and 5.8, while the obtained parameters are listed in Tab. 5.1. It is important to notice that the present model is derived for half filling and thus it is optimal to describe La_2CuO_4 magnon dispersion. On the other hand, this model is not strictly applicable to $\text{La}_{2-x}\text{Sr}_x\text{CuO}_4$ and Bi2201 since they are doped away from half filling conditions. Nevertheless, we adopt this model because: (i) there is no analytical solution for doped systems; and (ii) it is still a good parametrization tool which can be used to compare different systems.

TABLE 5.1: Results of the fit to the magnetic-excitation dispersion of LCO [82, 83], LSCO $x = 0.12$ (this work) and Bi2201 [143]. For comparison, the results from the fit for LCO dispersion, are shown as reported from previous studies. \star indicates the results using the procedure described in the main text.

$\text{La}_{2-x}\text{Sr}_x\text{CuO}_4$	U [eV]	U/t	t'/t	t''/t	Z	Ref.
$x = 0$	2.2	7.4	0	0	1.18	[82, 83]
$x = 0$	3.6	8.3	-0.313	0.167	1.219	[84]
$x = 0$	3.9	9.1	-0.308	0.154	1.219	\star
$x = 0.12$	2.9	6.8	-0.405	0.202	1.219	\star
Bi2201						
$x = 0$	3.4	8.0	-0.352	0.176	1.219	\star

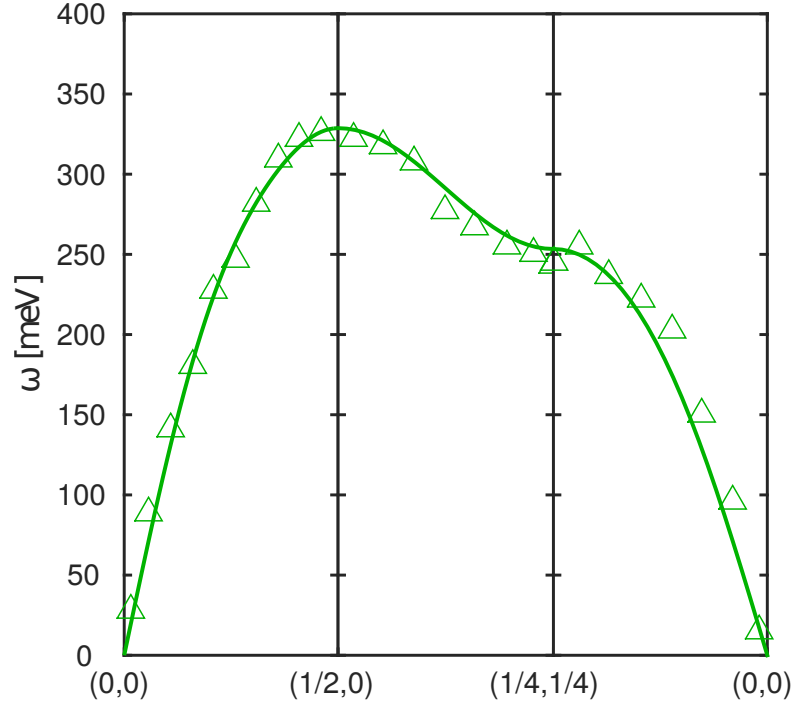


FIGURE 5.8: Spin excitations of $\text{Bi}_2\text{Sr}_{0.99}\text{La}_{1.1}\text{CuO}_{4+\delta}$ along the Brillouin zone as indicated. Solid line is the fit to the data using the Hubbard model. Data extracted from Ref. [143].

5.3 Discussion & Conclusions

The main experimental observation is that the zone-boundary dispersion E_{ZB} is considerable for $\text{La}_{2-x}\text{Sr}_x\text{CuO}_4$ with $x = 0.12$. In order to understand what is the important parameters for such an effect we can analyze in more detail the Hubbard model adopted in the present study. To this end, it was shown [82, 83] that for LCO a model with only t and U was enough to describe the experimental data, if the cyclic hopping terms were taken into account. For such a model the zone-boundary dispersion takes the following expression: $E_{ZB} = 12ZJ_2$, with $J_2 = 4\frac{t^4}{U^3}$ (see Chapter 3). Thus considering $t = 0.43$ eV and $U/t = 8$, it is straightforward to see that $E_{ZB} \approx 50$ meV. Although, with lower values of U/t it is possible to obtain the observed E_{ZB} in $\text{La}_{2-x}\text{Sr}_x\text{CuO}_4$ with $x = 0.12$, it is not possible to obtain a good fit to the data allowing to reproduce simultaneously both the azimuthal and nodal direction dispersions. Consequently, higher-order hopping terms t' and t'' has to be included. Having an analytical expression [84, 85] for the spin dispersion we can easily extract the E_{ZB} functionality, but since it has a complicated expression, we consider the approximated solution expressed in Eq. 3.12. The quality of this approximation, with respect to the exact solution, can be appreciated in Fig. 3.2 in Chapter 3. The main observation for the Eq. 3.12 is that the additional term for E_{ZB} depends quadratically on the ratio t'/t , thus allowing bigger zone-boundary dispersion

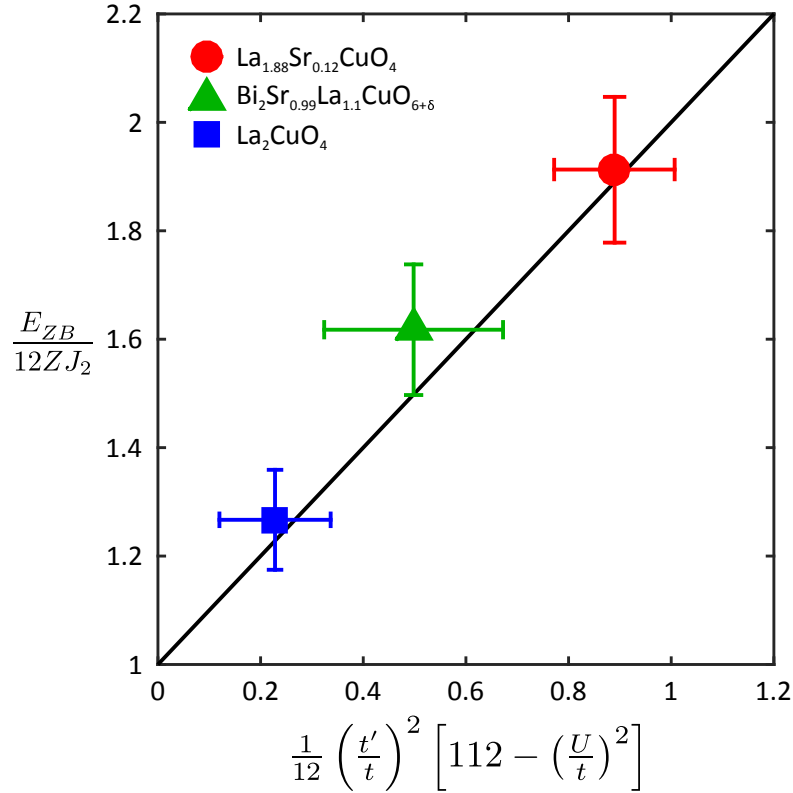


FIGURE 5.9: Zone-boundary dispersion, normalized to $12ZJ_2$ (see text for further details), *vs.* the respective approximated analytical value. Data points are obtained using the experimental E_{ZB} and fit results for U/t and $-t'/t$ (while having $t = 0.43$ eV, $Z = 0.219$ and $-t''/t' = 0.5$). Solid black line is the approximated solution for $U/t = 8$. Data for La_2CuO_4 and $\text{Bi}_2\text{Sr}_{0.99}\text{La}_{1.1}\text{CuO}_{4+\delta}$ are extracted from Refs. [83] and [143] respectively.

for higher ratios of U/t . In fact, considering $t = 0.43$ eV, $U/t = 8$ and $-t'/t = 0.4$, a zone-boundary dispersion of about 80 meV is obtained.

This simple analysis brings us to the conclusion that t' (and consequently t'') is an important parameter for the doped systems. Indeed, a good fit to the data can be obtained for both $\text{La}_{2-x}\text{Sr}_x\text{CuO}_4$ with $x = 0.12$ and $\text{Bi}_2\text{Sr}_{0.99}\text{La}_{1.1}\text{CuO}_{4+\delta}$ [Figs. 5.7(c-e) & 5.8]. This can be also appreciated in Fig. 5.9 where the experimental and fit E_{ZB} results are compared using the approximated solution.

The importance of the t' hopping term is further evidenced from the numerical value obtained from our fit. We quantify this parameter by the, physically meaningful, ratio $-t'/t$, for which a value of ~ 0.41 was obtained for $\text{La}_{2-x}\text{Sr}_x\text{CuO}_4$ with $x = 0.12$ (Tab. 5.1). This can be directly compared with the Fermi surface analysis from ARPES data. Using a single-band tight binding model, for the same compound and similar doping, a value of $-t'/t \cong 0.15$ is obtained [36]. In addition, we observe an increase of $-t'/t$ as a function of doping, since for La_2CuO_4 a value of about 0.31 is found. On the contrary, the ARPES study evidences a decrease of this parameter with increasing

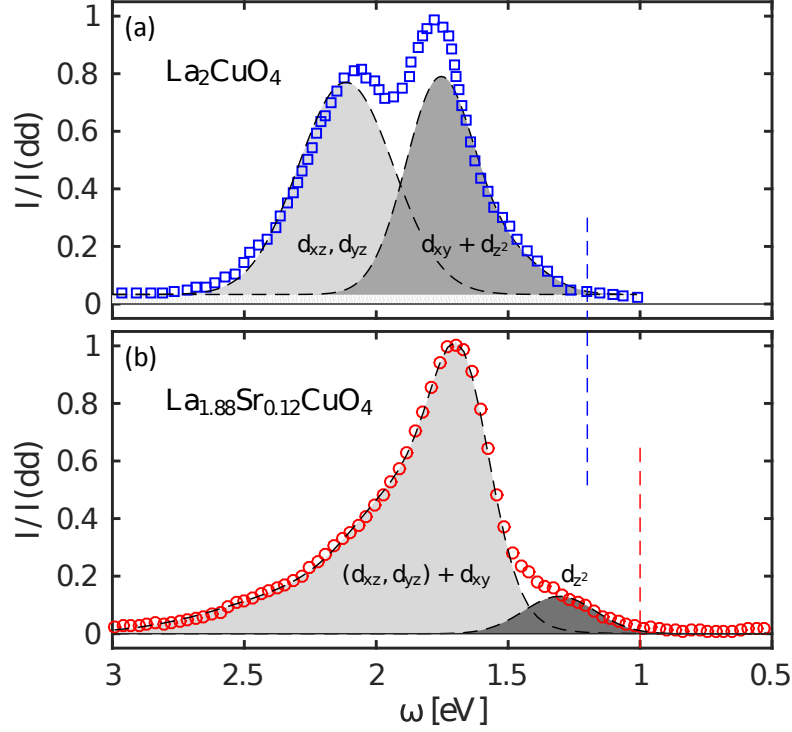


FIGURE 5.10: RIXS spectra in the energy range of dd excitations for La_2CuO_4 [143] (a) and $\text{La}_{2-x}\text{Sr}_x\text{CuO}_4$ with $x = 0.12$ (b). Shaded areas under the data are guides to the eye only, while the vertical dashed lines indicate the onset of these charge excitations.

doping, having $-t'/t = 0.20$ for $x = 0.03$ (see Fig. 5.3). To solve this discrepancy we invoke a two-orbital model, in which besides the $d_{x^2-y^2}$ also the d_{z^2} orbital is taken into account [130, 131].

In this model, a contribution to the Fermi surface topology is coming from the d_{z^2} Cu orbital. The stronger the hybridization between the $d_{x^2-y^2}$ and d_{z^2} orbitals is, the more this effect will impact the Fermi surface. This can be quantified by the energy difference ΔE between the corresponding bands. Indeed, for Hg1201, the d_{z^2} band is well below the Fermi level, contributing marginally to the Fermi surface [130, 131]. This is evidenced by the fact that t_r is varying little if adopting a single- and two-orbital models. The same calculation for La_2CuO_4 system evidences a strong contribution from the d_{z^2} orbital and consequently the t_r parameter varies considerably. This has also been linked to the large difference between the superconducting T_c for the optimally doped systems. It is concluded that the avoidance of the hybridization between the $d_{x^2-y^2}$ and d_{z^2} bands is favorable for the superconductivity. This mechanism is called *orbital distillation* [144].

To confirm that the d_{z^2} band is relevant in our system, we have to consider the dd excitations from RIXS spectra. In Fig. 5.10 La_2CuO_4 [143] and $\text{La}_{2-x}\text{Sr}_x\text{CuO}_4$ with $x = 0.12$ spectra are compared. We observe that the two system are considerably different: two distinct peaks are present for La_2CuO_4 , while a broad excitation is characterizing

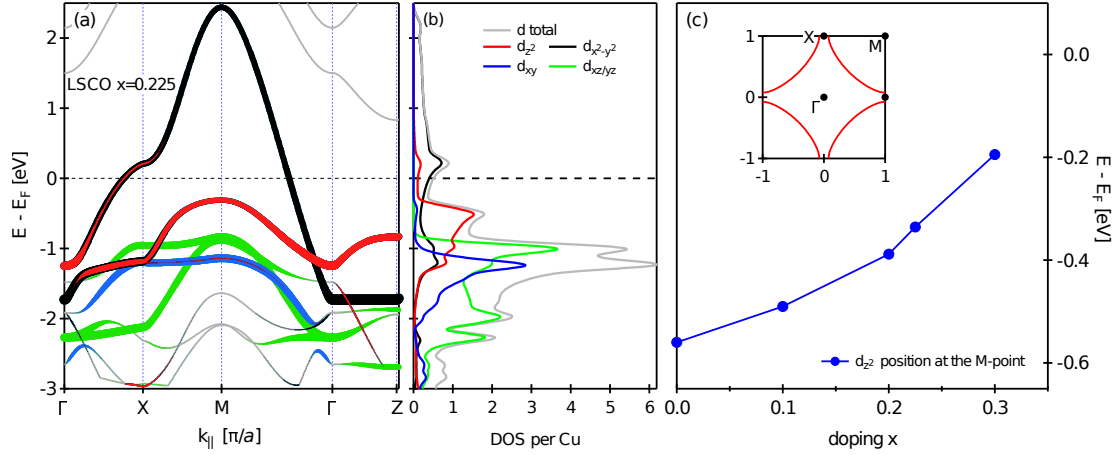


FIGURE 5.11: Density functional theory calculations for the band dispersion (a) through high-symmetry directions [see inset in (c)] and density of states (DOS) for Cu 3d orbitals (b) is presented for $\text{La}_{2-x}\text{Sr}_x\text{CuO}_4$ $x = 0.225$. In (c) is shown the doping dependence of the d_{z^2} band at the M point. A rigid shift of the bands is adopted to account for the change in doping. A tetragonal crystal structure is considered [120] for the calculations.

$\text{La}_{2-x}\text{Sr}_x\text{CuO}_4$ with $x = 0.12$ system. Unfortunately, due to the intrinsic broadening of these excitations, it is not possible to distinguish clearly each of the four ($d_{xz/yz}$, d_{xy} and d_{z^2}) contributions to the spectra. A RIXS cross-section study for La_2CuO_4 concluded that the d_{z^2} level lies in the low energy-loss part [76]. It is thus, reasonable to quantify the splitting between the $d_{x^2-y^2}$ (corresponding to zero energy loss) and d_{z^2} bands, by considering the onset of the dd excitations (vertical dashed lines in Fig. 5.10). Being, the onset of the dd excitations, closer to the zero energy loss for $\text{La}_{2-x}\text{Sr}_x\text{CuO}_4$ with $x = 0.12$, a stronger hybridization is present in the system. This is confirmed by DFT calculations on the overdoped $\text{La}_{2-x}\text{Sr}_x\text{CuO}_4$ (see Fig. 5.11). The vicinity of the d_{z^2} band is visible in (a) across the whole Brillouin zone, which is also evidenced by the (momentum integrated) density of states in (b). This supports the assumption to consider the onset of the dd excitations to quantify this effect. Furthermore, a doping-dependent evolution of the d_{z^2} band, as extracted from DFT calculations at the M point, is consistent with the experimental observation [Fig. 5.11(c)].

Recently, an ARPES study [124] directly observed the hybridization between the $d_{x^2-y^2}$ and d_{z^2} bands in $\text{La}_{2-x}\text{Sr}_x\text{CuO}_4$ $x = 0.23$. Using a two-orbital tight-binding model a value for t_r is found to be 0.32. This suggests that $t_r \sim 0.4$ is a universal value for single-layer cuprates but masked by the vicinity of the van Hove singularity close to the Fermi surface [130]. The latter results from the repulsion of the $d_{x^2-y^2}$ and d_{z^2} bands. We notice that this might be the main cause of disagreement between the single-band tight-binding and Hubbard models.

To conclude, we have observed, by means of RIXS, a strong zone-boundary dispersion

in $\text{La}_{2-x}\text{Sr}_x\text{CuO}_4$ with $x = 0.12$. Compared to La_2CuO_4 , this effect is consistent with an enhanced $-t'/t$ ratio due to a stronger hybridization of the $d_{x^2-y^2}$ and d_{z^2} bands. The relevance of d_{z^2} band for the cuprates is thus confirmed.

Chapter 6

Magnetic & Charge Excitations in La_2CuO_4 Thin Films

Cuprate superconductivity arises once the system is doped away from the insulating Mott state. The latter is characterized by a static antiferromagnetic order with spins aligning predominantly in-plane inside the CuO_2 planes. For La_2CuO_4 , this order persists up to a Néel temperature $T_N = 325$ K [145]. While this static order is rapidly suppressed with doping, a spin density wave (or stripe order) is present up to approximately optimal doping for superconductivity. For these reasons spin fluctuation theory was proposed as the pairing mechanism for superconducting Cooper pairs [1]. Being the SC dome very close to the antiferromagnetic insulating state, antiferromagnetic spin fluctuations are proposed. This picture is supported by an analog of the isotope effect for the phonon-mediated superconductors. In Fig. 6.1(a) both the T_N and T_c as a function of doping y are presented for several values of x in $(\text{Ca}_x\text{La}_{1-x})(\text{Ba}_{1.75-x}\text{La}_{0.25+x})\text{Cu}_3\text{O}_y$ system [146]. Each curve is normalized to the optimal-doping superconducting transition temperature T_c^{opt} , while T_N was corrected accordingly due to the absence of a pure three-dimensional antiferromagnetic order. Also a proper scaling of the doping axis is made to align the optimal dopings for each system. Besides these details, the relevant information, that comes from this analysis, is that an overlap of the AF and SC domes is obtained for these systems. This evidences a strong intertwining between antiferromagnetic Mott insulator and superconductivity.

The antiferromagnetic spin-fluctuation theory was applied also to other compounds, like for example the heavy fermion superconductors [1]. A Moriya-Ueda like plot can be drawn for several compounds, where the superconducting transition temperature T_c is related to the characteristic spin-fluctuation temperature T_0 [147]. Fig. 6.1(b) presents this relation, where linear correlation is evidenced. This is a further supporting clue to

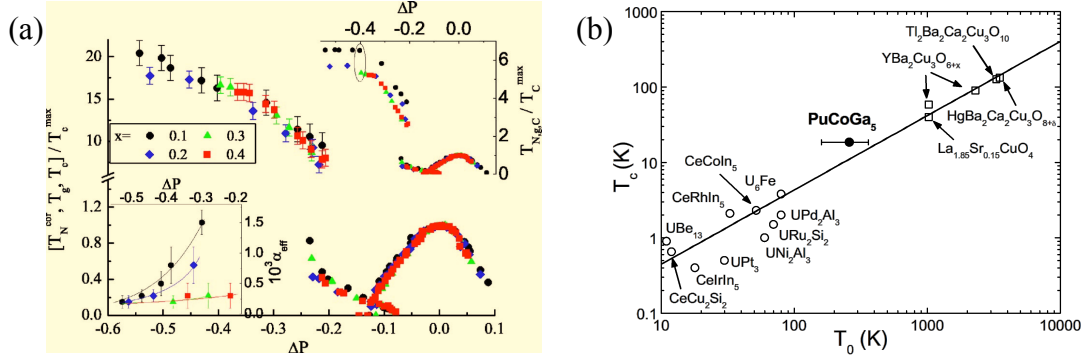


FIGURE 6.1: (a) Scaled antiferromagnetic and superconducting domes for $(\text{Ca}_x\text{La}_{1-x})(\text{Ba}_{1.75-x}\text{La}_{0.25+x})\text{Cu}_3\text{O}_y$ system. For more details see Ref. [146] from which the figure was adapted. (b) Moriya-Ueda like plot of superconducting transition temperature T_c vs. the characteristic temperature of spin fluctuations T_0 , for compounds as indicated. Solid line is a guide to the eye. Figure adapted from the supplementary information of Ref. [147].

the antiferromagnetic spin-fluctuation mechanism. Furthermore it takes a more generic significance since different type of systems obey this relationship.

While on one side, spin excitations are studied both theoretically and experimentally, on the other, ways to enhance or suppress the superconducting transition temperature are tested. This is of great interest, since it allows to vary the intertwinning between different phases in these materials and thus to obtain new insights into the physics of these phenomena. Modification of structural lattice parameters, for example, has a direct impact on the superconducting phase. Application of hydrostatic pressure on $\text{HgBa}_2\text{CuO}_{4+\delta}$ system [Fig. 6.2(a)], has been observed favorable to enhance T_c by about 20 K at 10 GPa [27]. Interestingly both underdoped and optimally doped systems reach the same T_c^{max} at high enough pressures. Anisotropic kind of pressure, realized in strained thin films, has also important implications. Depending on the substrate, an enhancement or suppression of T_c can be obtained, as compared to the bulk system. In Fig. 6.2(b) this effect is presented for $\text{La}_{2-x}\text{Sr}_x\text{CuO}_4$ system [28]. Namely, thin films grown on LaSrAlO_4 substrate result in an overall higher T_c . An opposite effect is obtained for thin films on SrTiO_3 substrate. While, this phenomena was linked to the out-of-plane lattice parameter, a microscopic explanation has not been proposed. In addition, one should not forget that also the in-plane lattice parameter is changed (with respect to the bulk crystal), and this, within the AF pairing mechanism, has a direct influence on the Heisenberg exchange interaction.

Driven by the relevance of d_{z^2} orbital in the $\text{La}_{2-x}\text{Sr}_x\text{CuO}_4$ system (Chapter 5) and by the relevance of the AF phase in cuprate system, we conducted a RIXS study of the magnetic and charge excitations of thin films of La_2CuO_4 .

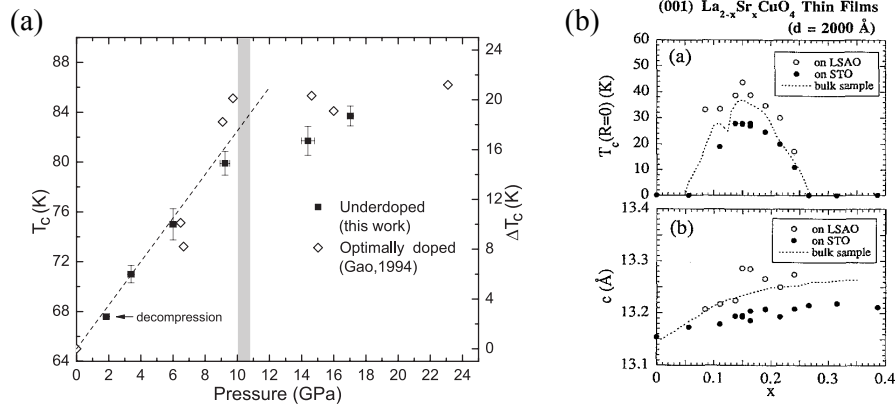


FIGURE 6.2: Superconducting transition temperature T_c as a function of hydrostatic applied pressure, for $\text{HgBa}_2\text{CuO}_{4+\delta}$ system, is shown in (a). Adapted from Ref. [27]. In (b) is shown T_c as a function of doping x for thin films of $\text{La}_{2-x}\text{Sr}_x\text{CuO}_4$ (upper panel). A suppression of the superconducting dome is obtained with STO substrate (filled circles), while an enhancement is visible if the thin films are grown on LSAO substrate (open marks). Dotted line is the T_c for bulk materials. The related c -axis parameters are shown in the lower panel. Adapted from Ref. [28].

6.1 RIXS Study of La_2CuO_4 Thin Films

Thin films of La_2CuO_4 have been grown by molecular beam epitaxy (MBE) technique on four different substrates: LaSrAlO_4 (LSAO), NdGaO_3 (NGO), $(\text{LaAlO}_3)_{0.3}(\text{Sr}_2\text{TaAlO}_6)_{0.7}$ (LSAT) and SrTiO_3 (STO). The growth was performed on cubic (001)_c surfaces of LSAO ($a = 3.756$ Å), LSAT ($a = 3.868$ Å) and STO ($a = 3.905$ Å), and on the pseudo-cubic, resulting from the orthorhombicity, (001)_{pc} surface of NGO ($a = 3.864$ Å). The LCO/LSAO sample is presented in Fig. 6.3(a). We consider the in-plane lattice parameters a_f of the films to be equal to the respective a_s of the substrates. Although, by means of x-ray diffraction technique, signs of structural relaxation has been observed for NGO and LSAT thin films.

We define strain as $\varepsilon = (a - a_0)/a_0$, where a is the in-plane lattice parameter of the thin film and $a_0 = 3.803$ Å the respective bulk value. In-plane compressive (LSAO) and tensile (NGO, LSAT and STO) strains thus result, with ε of -1.25 , 1.59 , 1.70 and 2.67 % respectively. Due to the Poisson effect, also the out-of-plane lattice parameter c of the films is changed, since the system tries to maintain the same volume as for bulk crystal. This is confirmed by x-ray diffraction and the results are presented in Fig. 6.3(c). As expected for LSAO the 2θ angle of the thin-film peak is lower than that for the other samples. Consequently, due to the Bragg law, the c lattice parameter is higher. Additionally, from these measurements, it is possible to extract the thickness of the thin films counting the number of replicas of this reflection. The results are shown in Tab. 6.1 along with the in- and out-of-plane strain values. Note that the bulk La_2CuO_4 is orthorhombic [120] but

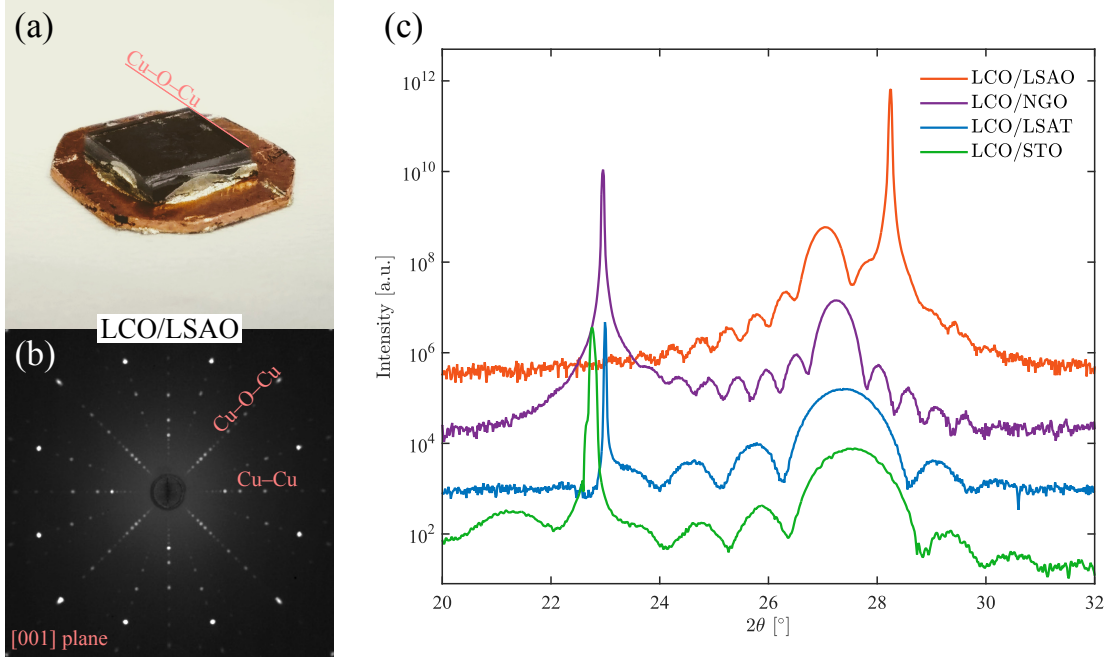


FIGURE 6.3: (a) and (b) present the photo and x-ray Laue pattern of LCO/LSAO sample ($\sim 5 \times 5 \text{ mm}^2$). The bond directions of the sample are also indicated. (c) 2θ scans along the c axis for samples as indicated. The c lattice parameter for each sample is extracted from the broad peak at about 27° – 28° region while the thickness from the number of fringes. The sharp peak at 23° and 28° is coming from the underlying substrates. An incident energy of 1.5406 \AA was used. Each spectra is shifted vertically for a better visualization and the intensity is presented in logarithmic scale.

since the thin films are bound to the substrates, it is reasonable to assume a tetragonal structure even at low temperatures.

The experiment was conducted at ADDRESS beamline at the SLS [see Fig. 2.3(a)]. At Cu L_3 edge an energy resolution of 136 meV (FWHM) was obtained as extracted from the elastic line of the spectra. A scattering angle of 130° was used. Measurements were performed at the base temperature of 20 K at UHV conditions (better than 10^{-9} mbar). Both linear vertical (σ) and horizontal (π) incident light polarizations were used. Samples were pre-aligned using a commercial Laue diffractometer (see Chapter 2). A Laue

TABLE 6.1: Thickness and lattice parameters of the thin films are shown. Also the corresponding bulk values are indicated [120]. From this the in-plane ε and out-of-plane ε_c are calculated. All the parameters are measured at room temperature. The substrate lattice parameters are taken from Refs. [28, 148].

Sample	h [nm]	a [Å]	c [Å]	ε [%]	ε_c [%]
LCO/STO	7–8	3.905	12.891	2.67	-2.01
LCO/LSAT	7–8	3.868	12.981	1.70	-1.33
LCO/NGO	17–19	3.864	13.077	1.59	-0.60
LCO/LSAO	18–19	3.756	13.195	-1.25	0.30
Bulk LCO	—	3.803	13.156	—	—

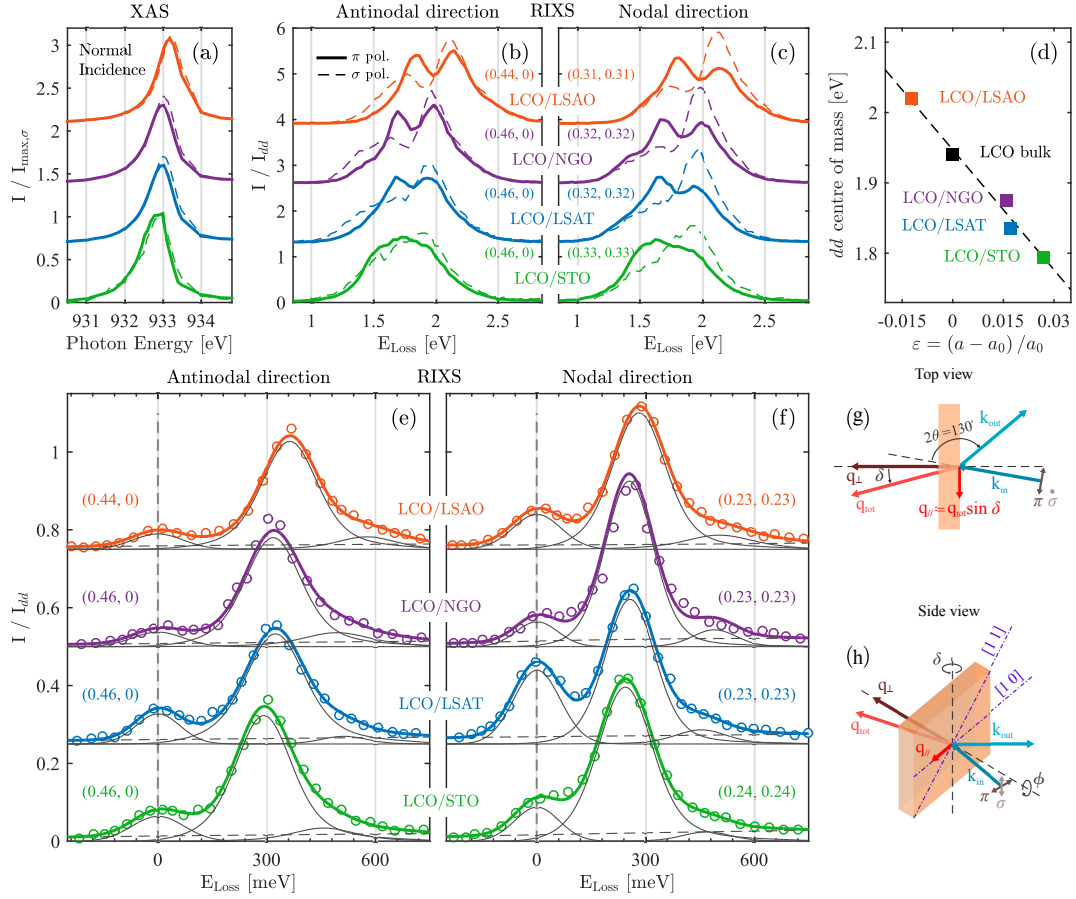


FIGURE 6.4: XAS spectra at Cu L_3 (a) and RIXS dd excitations (b-c) for samples (and momenta) as indicated. Solid (dashed) lines correspond to incident π (σ) light polarization. The "center of mass" for the dd excitations, extracted from the spectra in (b) & (c), are presented in (d) as a function of in-plane strain ε . RIXS spectra along the antinodal (e) and nodal (f) directions (for momenta as indicated), show the evolution of magnetic excitations. Schematic representation of the scattering (grazing-in) geometry is shown from the top (g) and side (f) views.

pattern, with the respective bond directions, is shown in Fig. 6.3(b), which results similar as for $\text{La}_{2-x}\text{Sr}_x\text{CuO}_4$ with $x = 0.12$ (see Fig. 2.1). Reciprocal lattice units ($2\pi/a$) are adopted to indicate the (parallel) momentum transfer $\mathbf{q} = \mathbf{q}_{\parallel} = (h, k)$. Scattering geometry is schematically represented in Fig. 6.4(g,h).

Raw XAS and RIXS data on our four thin film systems are presented in Fig. 6.4. The first observation is that, going from tensile to compressive in-plane strain, the resonance of the Cu L_3 edge is shifting to higher energies [Fig. 6.4(a)]. Since this signal is proportional to the splitting between lower and upper Hubbard bands (LHB and UHB respectively), a strain induced variation of the on-site Coulomb interaction U is evidenced. Choosing the incident photon energy in accordance to the resonance for each sample, RIXS spectra have been acquired along three high-symmetry directions: antinodal (Cu–O–Cu), nodal (Cu–Cu) and azimuthal [see inset of Fig. 6.5(c)]. Each spectra has been normalized to

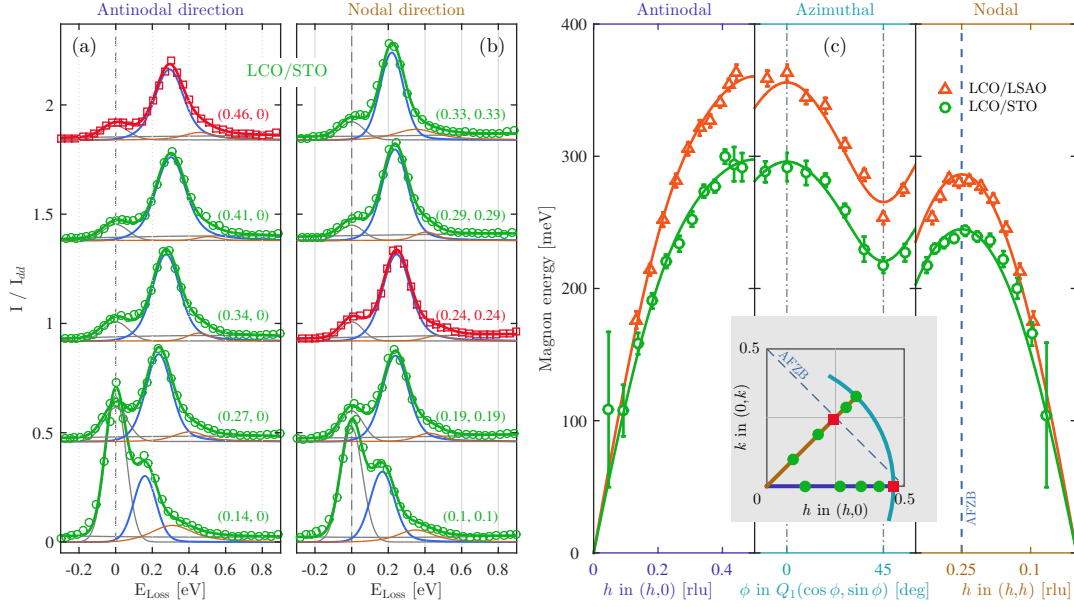


FIGURE 6.5: A selection of raw spectra, with the respective fits (see main text for more details), is presented along the antinodal (a) and nodal (b) direction for LCO/STO sample. Red spectra indicate the closest to the antiferromagnetic zone boundary border [same as in Fig. 6.4(e) & (f) respectively]. The fit-extracted pole of the excitation is plotted in (c) with respect to the momenta transfer (see inset) and compared to the result from the LCO/LSAO sample. In (c) Q_1 equals to 0.4611 LCO/STO and to 0.4437 for LCO/LSAO, as a result of different resonances and in-plane lattice constants.

the integrated (over energy loss) spectral weight of the dd excitations. Similar to the XAS, also the dd excitations present a similar shift, both along the antinodal [Fig. 6.5(b)] and nodal [panel (c)] directions. This is further evidenced by the *center of mass* of these features, as represented in Fig. 6.5(d). In addition, another strain effect can be inferred from the shape of the dd excitations. In fact they are broad for LCO/STO and evidence clearly two peaks for the other samples. This resembles the bulk $\text{La}_{2-x}\text{Sr}_x\text{CuO}_4$ and La_2CuO_4 signals respectively (see Fig. 5.10). Since these excitations are a measure of the splitting of the $d_{x^2-y^2}$ and d_{z^2} , d_{xy} and $d_{xz/yz}$ bands, a pressure induced variation of crystal-field environment is observed. If, again, we consider the onset of the dd excitations to be representative of the splitting between the $d_{x^2-y^2}$ and d_{z^2} bands, we observe the predicted evolution. The higher the c lattice parameter ($c_{\text{LCO/LSAO}} > c_{\text{LCO/STO}}$) the higher the splitting, and a lower hybridization between the two bands is thus expected.

The imposed strain also has an evident effect on the magnetic excitations along the antinodal and nodal directions [Fig. 6.4(e) and (f) respectively]. Indeed, while LCO/STO presents a dispersion of about 300 meV near the $(1/2, 0)$ high-symmetry point, the respective excitation is hardened of about 60 meV for the in-plane compressive LCO/LSAO sample. This directly evidences a strain evolution of the exchange interaction in this

TABLE 6.2: Parameters obtained from the fit to the data (exp) and from DFT and cRPA calculations as indicated. Fits are obtained using a Hubbard model for strong coupling, with $Z = 1.219$, $-t''/t' = 1/2$ and $U/t = 9$ as fixed parameters. For completeness a hypothetical La_2CuO_4 sample, with $a = 3.842 \text{ \AA}$ and $c = 13.105 \text{ \AA}$, is also considered for the theoretical calculations.

Sample	$t_{(\text{exp})} [\text{meV}]$	$-\frac{t'}{t}_{(\text{exp})}$	$t_{(\text{DFT})} [\text{meV}]$	$-\frac{t'}{t}_{(\text{DFT})}$	$-\frac{t''}{t'}_{(\text{DFT})}$	$U_{(\text{cRPA})} [\text{eV}]$
LCO/STO	460.5	0.389	369.6	0.0908	-0.044	1.92
LCO/LSAT	488.9	0.387	395.0	0.0907	0.165	2.05
LCO/NGO	483.6	0.388	416.1	0.0910	0.335	2.20
LCO/LSAO	613.2	0.422	473.7	0.0917	0.640	2.60
Bulk LCO	—	—	443.7	0.0915	0.510	2.40
Hypo. LCO	—	—	417.9	0.0917	0.361	2.25

system, since $E_{(1/2,0)} \propto J_1$. Furthermore a smaller hardening is observed along the nodal direction, and thus a zone-boundary dispersion E_{ZB} is also dependent on the imposed strain.

To quantify this effect on the magnon dispersion, we fit the data using a similar method as for $\text{La}_{2-x}\text{Sr}_x\text{CuO}_4$ with $x = 0.12$ in Chapter 5. More precisely a Gaussian is adopted for the elastic line. The standard deviation σ is used as a fit parameter to account for the presence of the phonon at about 50 meV [80]. A second-order polynomial functionality is used to mimic the dd -excitation background. Antisymmetric Lorentzian [77–79] (see Eq. 2.5) is used both for the magnon and small multimagnon [80] signals. Since this is an undoped system, the resulting magnons are resolution limited and thus the pole of the excitation corresponds approximately to the peak maximum. The quality of the fit can be appreciated in Fig. 6.5 for LCO/STO along the antinodal (a) and nodal (b) high-symmetry directions. In Fig. 6.6, similar data are shown for LCO/LSAO (a,b), LCO/NGO (d,e) and LCO/LSAT (g,h). The extracted magnon dispersion for LCO/STO and LSCO/LSAO, through the Brillouin zone (see inset), is shown in Fig. 6.5(c) [and in Fig. 6.6(c,f,i) for the other systems]. The difference in $E_{(1/2,0)}$ between the two system is evident, as much as the bigger E_{ZB} for the LCO/LSAO.

The evolution of the magnon dispersion on these samples was characterized by means of Hubbard model at strong coupling, as it was done for $\text{La}_{2-x}\text{Sr}_x\text{CuO}_4$ with $x = 0.12$. To compare directly the available samples we fix the ratio $U/t = 9$. This value is chosen in order to be within the band-width controlled region ($U/t > 8$) and below the, Monte Carlo extracted [149], limit for a persistent (in temperature) Mott insulator ($U/t = 11$). Again, $Z = 1.219$ and we assume $-t''/t' = 1/2$ for simplicity. Thus fitting the dispersion relation for all the compounds [see solid line through the data Fig. 6.5(c) and Fig. 6.6(c, f & i)], the evolution of the first- and second-neighbor hopping integrals is obtained as a function of strain. These results are shown in Fig. 6.7 and Tab. 6.2, and compared with

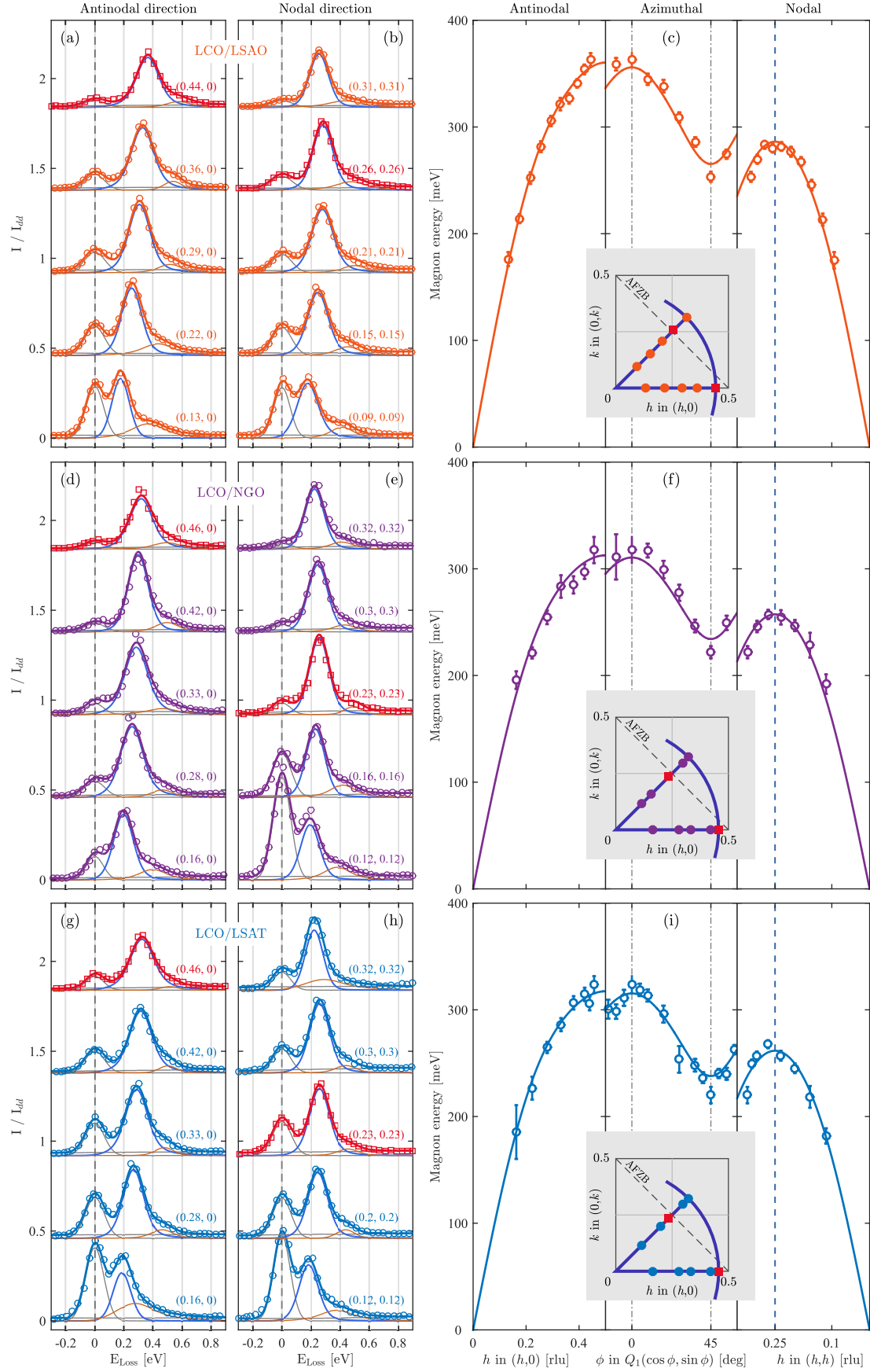


FIGURE 6.6: A selection of raw antinodal- and nodal-direction spectra and the respective dispersion of the magnetic excitations for LCO/LSAO (a-c), LCO/NGO (d-f) and LCO/LSAT (g-i) samples. For more detail see the caption of Fig. 6.5 and the main text.

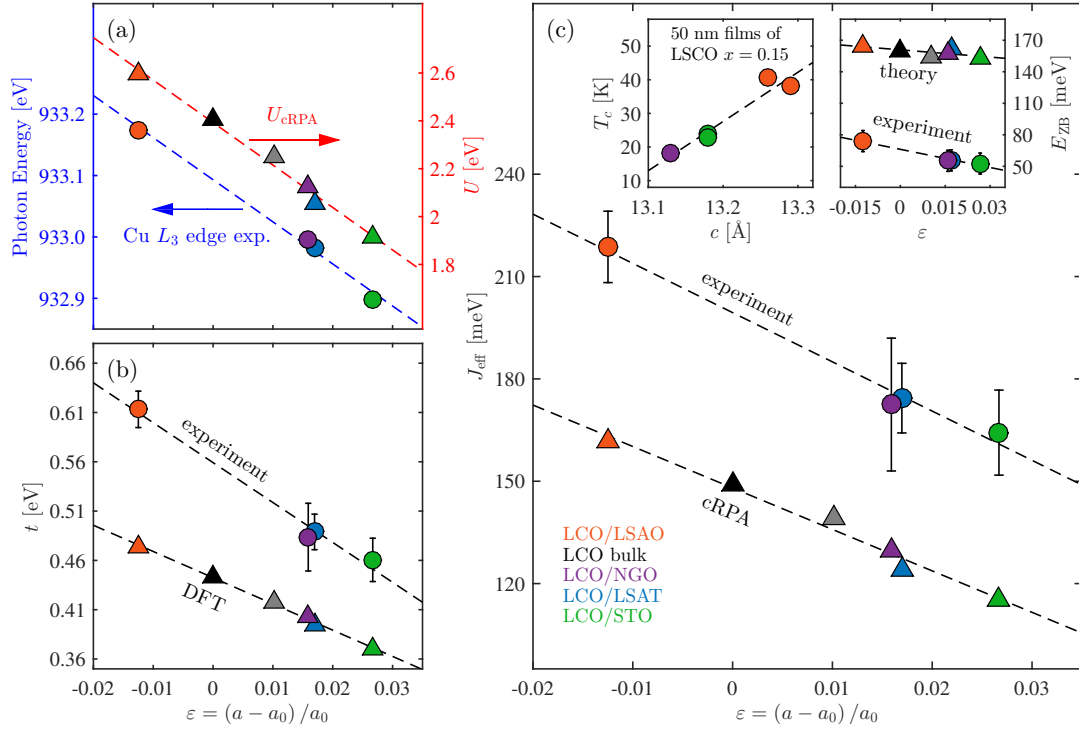


FIGURE 6.7: Experimental and theoretical parameters for La_2CuO_4 thin films. In (a) the experimentally extracted resonance of the Cu L_3 edge (left) is compared to the cRPA calculation for U (right). In (b) the experimental and DFT results for t are shown as a function of in-plane strain ε . With the respective (experimental and theoretical) values for t and U , the effective exchange interaction J_{eff} (see main text) is computed and presented as a function of strain. The value of the zone-boundary dispersion E_{ZB} is presented in the right inset as a function of strain for both experiment and theory. Left inset represents superconducting T_c for optimally doped thin films (50 nm) of $\text{La}_{2-x}\text{Sr}_x\text{CuO}_4$ as a function of out-of-plane lattice parameter. Note that the theoretical value corresponding to $\varepsilon \sim 0.01$ (gray triangular mark) is an artificial sample as described in the main text.

the theoretical calculations¹ using density functional (DFT) and constrained random phase approximation (cRPA) theories. While the experimental and theoretical results differ numerically, the evolution, with respect to the strain, is in good agreement.

Before proceeding with the implications of these results, we should spend a few words on J_{eff} and the theoretical calculations. We define $J_{\text{eff}} = 4\frac{t^2}{U} - 64\frac{t^4}{U^3}$ [84]. This is preferred over J_1 since $E_{(1/2,0)} \approx 2J_{\text{eff}}$ in our case, while $2J_1$ greatly overestimates the experimental evidence. Additionally, having the ratio of U/t fixed, it results that $J_{\text{eff}} \propto t$.

To simplify the theoretical calculations, a tetragonal crystal symmetry was assumed. This is justified, since it has been shown that the rotation of the CuO_6 octahedra, has a negligible effect on the resulting t and U parameters [58]. The adopted lattice parameters are shown in Tab. 6.1 and an additional hypothetical sample was considered with $a = b = 3.842 \text{ \AA}$ and $c = 13.105 \text{ \AA}$. The latter is extrapolated from the experimental

¹Performed by J. M. Tomczak.

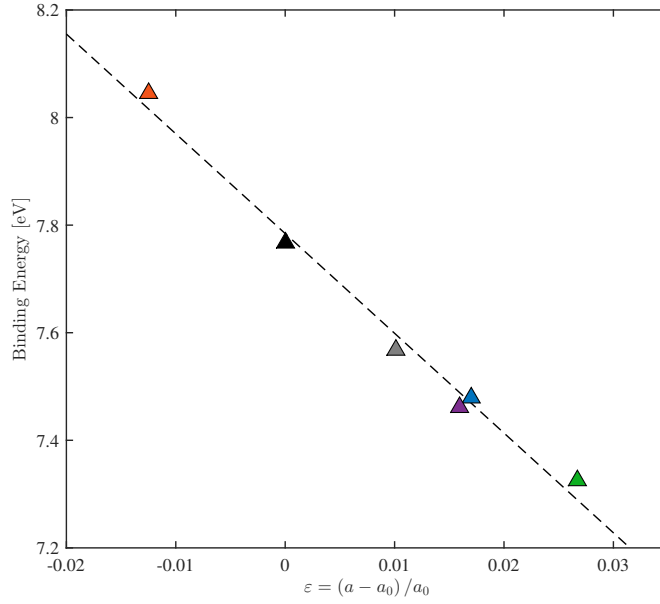


FIGURE 6.8: Evolution of the oxygen p bands with only p_x and p_y character are presented *vs.* in-plane strain, as extracted from DFT calculations.

data available for our samples. For comparison also the values for a bulk crystal were calculated. Notice that, while the distance between the in-plane oxygen is set by a , the distance with the apical oxygen d_{AO} , as much as with the La atom d_{La} , is assumed to be directly proportional to c . In other words, d_{AO}/c and d_{La}/c is considered to be the same as in the bulk compound and equal to 0.18(4) and 0.36(1) respectively [120].

6.2 Discussion & Conclusions

We have observed from the XAS spectra that the local Coulomb interaction U is increasing upon in-plane compressive strain [Fig. 6.7(a)]. This was a conclusion from a picture where the UHB and the LHB were the important characteristics of the system. However, we remind that La_2CuO_4 is a charge-transfer Mott insulator [132]. This means that instead of the Mott gap Δ_{M} we should consider the charge-transfer gap Δ_{CT} . In Fig. 6.8 we show how the p_x and p_y bands, which are degenerate in the tetragonal symmetry, evolve with respect to the in-plane strain. For compressive strain, thus, oxygen $p_{x/y}$ bands shift to higher binding energies. We thus conclude that, in our case, it is equivalent to consider Δ_{M} instead of Δ_{CT} , as they present similar evolution upon strain.

To understand what is the drive for an increased U , we performed a cRPA calculations. In fact, Coulomb interaction can both increase or decrease as a function of pressure [150–152], as a result of balance between the spatial extent of the orbitals and the effective

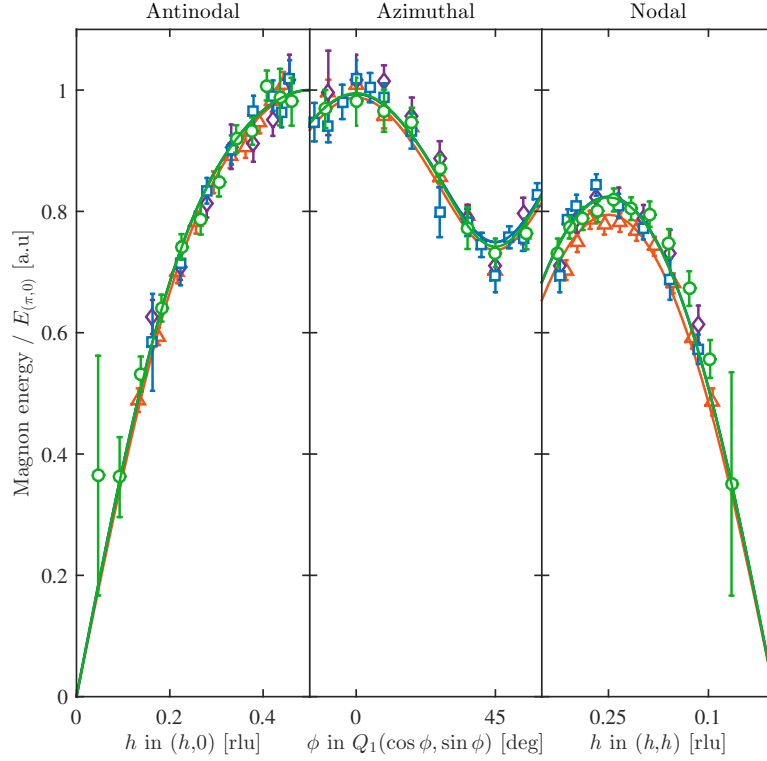


FIGURE 6.9: Magnetic excitation for all four samples (LCO/STO, LCO/LSAT, LCO/NGO and LCO/LSAO) normalized to the maximum along the antinodal direction $E_{(\pi,0)}$.

screening. Within the single band projection of the cRPA method, $d_{x^2-y^2}$ band contains the relevant physics in La_2CuO_4 thin films. In our case, two effects conspire to increase the local Coulomb interaction. On one side there is a lower hybridization between the oxygen $p_{x/y}$ and the $d_{x^2-y^2}$ bands, in addition to a higher splitting between the e_g states [Fig. 6.4(d)]. This, in turn results in a reduced effective screening and thus an enhancement of U . On the other hand, because of in-plane compressive strain, there is a higher overlap between the $d_{x^2-y^2}$ orbitals of neighboring Cu atoms. As a result, a (counter-intuitive) increase of the Coulomb interaction occurs [150]. We should point out, that the resulting theoretical value of $U/t \approx 5$ [see Tab. 5.1] is below the band-width controlled threshold ($U/t = 8$). It is, however, known that the correlation effects are underestimated when using the static limit of the interaction [153].

Now, let us discuss the magnetic-excitation dispersion. We saw that an enhanced effective exchange interaction J_{eff} occurs for the compressive LCO/LSAO sample. As we showed, this is directly related to the enhancement of t , resulting from a higher orbital overlap between the neighboring atoms. Thus an intuitive explanation of a higher dispersion of the antinodal dispersion $E_{(1/2,0)}$ is obtained. On the other hand, we also observed an enhanced zone-boundary dispersion E_{ZB} . In Chapter 5, we saw that a softening of

the nodal dispersion for $\text{La}_{2-x}\text{Sr}_x\text{CuO}_4$ with $x = 0.12$, with respect to the parent compound, is caused by a higher hybridization of $d_{x^2-y^2}$ and d_{z^2} bands. Thus, we expect to have a smaller E_{ZB} for LCO/LSAO than for LCO/STO, as the e_g splitting is bigger for the former [see Fig. 6.4(b-d)]. To explain this effect, we should have a closer look at the Hubbard-model fit results in Tab. 6.2. Besides an increased t for LCO/LSAO, we also observe a slightly increased $-t'/t$. Again this is in apparent contradiction with the results obtained from RIXS study on bulk $\text{La}_{2-x}\text{Sr}_x\text{CuO}_4$ with $x = 0.12$, but it might be a consequence of assuming a constant ratio of U/t for our samples. Nevertheless, the important result is that $-t'/t \approx 0.4$. Although a small sample dependence is found (see Tab. 6.2), this supports the fact that this is a universal characteristics for the cuprate system [124, 130, 131]. With this in mind, if we look at the approximated solution for E_{ZB} (Eq. 3.12), it is evident that for a constant $-t'/t$ (and U/t) the relevant parameter is only the first-neighbor hopping integral t . The fact that, in our case, effectively only one parameter is relevant is further supported by the scaling relation illustrated in Fig. 6.9. Here the dispersion relation, for each sample, is normalized to the experimentally obtained antinodal dispersion $E_{(1/2,0)}$. This further supports the fact that, the effect of modified t has more relevance on the whole magnetic-excitation dispersion than the change induced from the variation of $-t'/t$ ratio.

To end this section, a projection on the optimally doped $\text{La}_{2-x}\text{Sr}_x\text{CuO}_4$ thin films physics can be made from the results obtained for undoped La_2CuO_4 . In Tab. 6.3 we report the relevant structural parameters for the optimally doped thin films as a function of superconducting transition temperature T_c . Although higher T_c has been linked to larger c -axis parameter [28, 112] [see left inset of Fig. 6.7(c)], the physical origin of this

TABLE 6.3: In-plane a and out-of-plane c lattice parameters and superconducting transition temperature T_c for $\text{La}_{2-x}\text{Sr}_x\text{CuO}_4$ thin films grown on substrates as indicated. Thickness h of the thin films is indicated as it has considerable influence on T_c . Bulk $\text{La}_{2-x}\text{Sr}_x\text{CuO}_4$ parameters are also indicated for comparison.

Substrate	h [nm]	Doping $[x]$	a_S [Å]	c [Å]	a [Å]	T_c [K]	Ref.
STO	15	0.10	3.905	13.17	3.80	10	[154]
STO	50	0.15	3.905	~ 13.16	~ 3.870	~ 23.9	[28]
STO	50	~ 0.16	3.905	~ 13.18	—	~ 23	[112]
STO	200	~ 0.16	3.905	~ 13.20	—	~ 28	[112]
STO	200	0.15	3.905	13.18	3.837	27.4	[28]
NGO	50	0.15	3.842	~ 13.13	~ 3.797	~ 18.2	[28]
LSAO	15	0.10	3.754	13.31	3.76	49.1	[154]
LSAO	50	0.15	3.756	~ 13.26	~ 3.756	~ 40.7	[28]
LSAO	50	~ 0.15	3.756	13.29	—	~ 38	[112]
LSAO	200	0.15	3.7564	13.29	3.762	43.8	[28]
Bulk LSCO	—	0.10	—	13.21	3.778	27	[155]
Bulk LSCO	—	0.15	—	13.23	3.777	36.5	[155]

effect has remained elusive. In addition the thickness of these films has an important relevance as they tend to relax to the bulk structure. Nevertheless, highest T_c has been observed for thin films of $\text{La}_{2-x}\text{Sr}_x\text{CuO}_4$ grown on LSAO substrate [28, 112]. In our case thin films of LCO/LSAO present higher e_g splitting and exchange interaction J_{eff} . If we project this knowledge to the doped systems, since a relation between the antiferromagnetic and superconducting domes has been proposed [146], we can conclude the following. The bigger e_g splitting for LSAO system is consistent with the *orbital distillation* effect, which has been proposed to be beneficial for superconductivity [130, 131]. On the other hand, higher e_g splitting might, indirectly enhance T_c by changing the screening of the local Coulomb interaction U . As for J_{eff} , a link with T_c is expected for a large U/t limit [146, 156, 157]. This would be consistent with the antiferromagnetic d -wave coupling for cuprates [1].

To conclude, we observed a direct link between the structural parameters and the local Coulomb interaction U , the first-neighbor hopping integral t and the exchange interaction J_{eff} for La_2CuO_4 thin films. We thus propose optimizing the Mott insulating state as a principle to reach higher superconducting T_c upon optimally doping the system.

Chapter 7

Conclusions

In summary, charge order in $\text{Ir}_{1-x}\text{Pt}_x\text{Te}_2$ and magnetic excitations in $\text{La}_{2-x}\text{Sr}_x\text{CuO}_4$ systems were studied by hard x-ray diffraction and resonant inelastic x-ray scattering respectively. For Pt doped IrTe_2 superconductivity is suppressed going from $x = 0.05$ to $x = 0.04$, where a strong long-range charge order is present down to 20 K. Additionally, only $(1/5, 0, 1/5)$ CO is found for $x = 0.04$, in contrast to the undoped sample where the ground state is characterized by the $(1/8, 0, 1/8)$ CO. For $x = 0.05$, no charge order is found at ambient pressure, but it reemerges under application of 17.7 kbar and having a $\delta = 1/5$ modulation. Also in this case superconductivity is suppressed when CO sets in. Notably, structural transition appears at lower pressures (where SC is still present) evidencing the requisite of lower lattice symmetry for the formation of the charge order. A careful examination of resistivity measurements and diffraction data, (both) upon application of hydrostatic pressure, evidences a particular suppression of SC for the $x = 0.05$ sample. Indeed, a progressive broadening of the SC transition is observed while the onset temperature remains fairly constant. To account for this phenomena we propose a model where superconductivity and charge order coexist. In fact, charge order can be explained as a formation of Ir-Ir dimerization, which organizes in a layered manner. It was observed that, dimer formation is followed by a local suppression of the density of states near the Fermi level. This in turn is likely to suppress superconductivity. We thus argue, that superconductivity is enclosed quasi-two dimensionally between the charge order layers. This model find its description in Berezinskii – Kosterlitz – Thouless transition, which has still to be confirmed (experimentally) for this system.

Magnetic excitation in $\text{La}_{2-x}\text{Sr}_x\text{CuO}_4$ with $x = 0.12$ has been studied along three different directions inside the Brillouin zone. A strong anisotropy is found between the antinodal and nodal directions, which is tracked by the azimuthal scan connecting these two directions. In order to quantify this experimental evidence, a fit to the data was

performed using a Hubbard model for strong coupling. The resulting ratio between the second- and first-neighbor hopping integrals resulted in $-t'/t \approx 0.4$, which is in contrast with the ARPES derived value of 0.15. This discrepancy is explained by means of two-band model, where the hybridization between the $d_{x^2-y^2}$ and d_{z^2} is considered. In fact, this model and our experiments suggest a universal value of $-t'/t \approx 0.4$ for single layered cuprates. This is also supported by a recent ARPES study on $\text{La}_{2-x}\text{Sr}_x\text{CuO}_4$ with $x = 0.23$, where a two-orbital tight-binding model was used to fit the Fermi surface [121, 124].

Driven by the relevance of the d_{z^2} band for the magnetic excitations, thin MBE films of La_2CuO_4 were grown on four different substrates. The resulting strain, going from in-plane compressive to tensile, has a direct impact on the lattice parameters. RIXS measurements revealed a strong evolution, as a function of strain, of the magnon dispersion both for the antinodal and nodal directions. From raw (XAS and RIXS) data and from the fit to the dispersion, using the Hubbard model, an enhancement of Coulomb interaction U , first-neighbor hopping term t and antiferromagnetic exchange interaction J_{eff} is observed for the compressive sample. In addition the fit revealed an almost constant ratio of $-t'/t$ for all the samples and equal approximately to 0.4, confirming the previously drawn conclusions. The relevance of this study has also an impact on the superconductivity for optimally doped samples. In particular, since the tensile sample, upon optimal doping, has also the highest T_c , a strong connection between the Mott and superconducting states is proposed. Optimizing the the insulating phase of these compounds is a promising strategy for improving the superconducting properties.

Appendix A

XRD Studies of $\text{Pr}_4\text{Fe}_2\text{As}_2\text{Te}_{0.88}\text{O}_4$

Among Fe-arsenides a new compound $\text{Pr}_4\text{Fe}_2\text{As}_2\text{Te}_{0.88}\text{O}_4$ (PFATO) has joined the family [158, 159]. This system resembles (structurally) the 1111 phase since it has Fe-As layer in between Pr-O layers [Fig. A.1(a)], but it has a considerably larger c axis parameter. At room temperature, it presents tetragonal $I4/mmm$ crystal structure, with $a = b = 4.02 \text{ \AA}$ and $c = 29.86 \text{ \AA}$ [159]. The angle α between As-Fe-As is $112.94(5)^\circ$ and the height h_p of the pnictogen is $1.332(3) \text{ \AA}$ [158, 159]. This quantities has been shown to be correlated with superconductivity (see Chapter 1), for which the optimal parameters are $\alpha = 109.47^\circ$ and $h_p = 1.38 \text{ \AA}$. PFATO presents a $\sim 10 \%$ of Te deficiency, which could be the doping causing superconductivity below $T_c \approx 25.5 \text{ K}$. The second critical magnetic field $H_{c2}(0 \text{ K}) \approx 6.5 \text{ T}$ is low if compared to other FeAs-based superconductors with similar T_c [158]. Due to these differences with other phases, PFATO has been defined as 42214 phase [158, 159]. Here, XRD studies on the structural transition of PFATO are presented. The results are discussed in comparison to resistivity and ARPES studies [160].

High-quality single crystals of PFATO were synthesized by a high-flux crystal growth technique [158]. The largest samples of about $50 \times 50 \times 10 \text{ }\mu\text{m}^3$ were used for these studies. XRD experiments were performed at P07 beamline in PETRA III, DESY (Hamburg) using 100 keV incident photon energy. To ensure an optimal instrumental resolution a high-resolution monochromator was adopted. The results are presented in reciprocal lattice units (r.l.u.) $\frac{2\pi}{a}$ and $\frac{2\pi}{b}$ in tetragonal notation. From the width of a Bragg peak (at high temperature) an overall resolution of $\sim 10^{-3}$ r.l.u. was obtained. The sample was mounted on a cactus needle (to reduce the background from the copper sample holder) in a way that a and b axes [Fig.A.1(a)] are in the scattering plane. This allowed to scan through the instrumentally accessible $(h, k, 0)$ Bragg reflections. A 10 T cryomagnet was used in order to obtain a good temperature control.

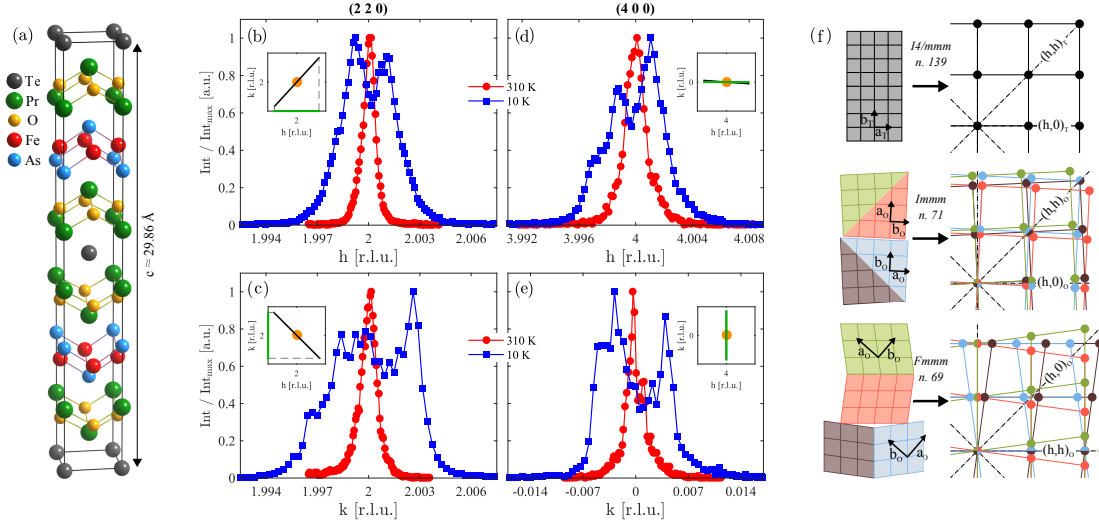


FIGURE A.1: (a) Unit cell of $\text{Pr}_4\text{Fe}_2\text{As}_2\text{Te}_{0.88}\text{O}_4$ represented by the tetragonal $I4/mmm$ space group. (b-e) longitudinal 2θ (top panels) and transverse ω (bottom panels) scans through the $(2,2,0)$ and $(4,0,0)$ Bragg reflections at room temperature (red) and 10 K (blue). (f) In-plane lattice domains for tetragonal $I4/mmm$ (top), orthorhombic $Immm$ (middle) and $Fmmm$ (bottom) with associated Bragg reflections. Orthorhombic axes, for the $Immm$ and $Fmmm$ symmetries, are shown with respect to the high-temperature $I4/mmm$ phase (dashed lines).

The structural transition of PFATO was studied by means of the $(2,2,0)$ and $(4,0,0)$ Bragg reflections [see Fig. A.1(b-e)]. In particular, longitudinal 2θ [Fig. A.1(b,d)] and transverse ω [Fig. A.1(c,e)] scans were acquired for each of the peaks at several temperatures. These scans correspond approximately to $[h, h, 0]$ ($[h, 0, 0]$) and $[2 - h, 2 + h, 0]$ ($[4, k, 0]$) scan directions for the $(2,2,0)$ ($(4,0,0)$) Bragg reflection. For a better comparison between the $(2,2,0)$ and $(4,0,0)$ data, a projection on the h and k axes is made, as shown in the insets of Fig. A.1(b-e). While at room temperature, a single peak is present for both reflections, colling down to 30 K, a splitting in the 2θ and ω scans is clearly evidenced [Fig. A.1(b-e)].

Generally, a splitting of a Bragg peak results from a crystal-symmetry breaking. If considering that only one symmetry operation is removed from the $I4/mmm$ space group, than the only two [161] possible orthorhombic subgroups are $Immm$ and $Fmmm$. In addition to the $I4/mmm$ structure, these are schematically represented in Fig. A.1(f) in both real and reciprocal spaces. As can be seen, we can distinguish between the two subgroups because of a different arrangement of domains. Namely, four peaks are expected along the orthorhombic $(h,0)_o$ direction and three along the $(h,h)_o$. Since the orthorhombic axes for the $Immm$ and $Fmmm$ structures are rotated by 45° , in the reference of the high-temperature tetragonal $I4/mmm$ structure, a unique identification of the low-temperature structure is possible. Nevertheless, the experimental data evidence a more complicated picture. In fact, a splitting of the $(2,2,0)$ Bragg peak is observed

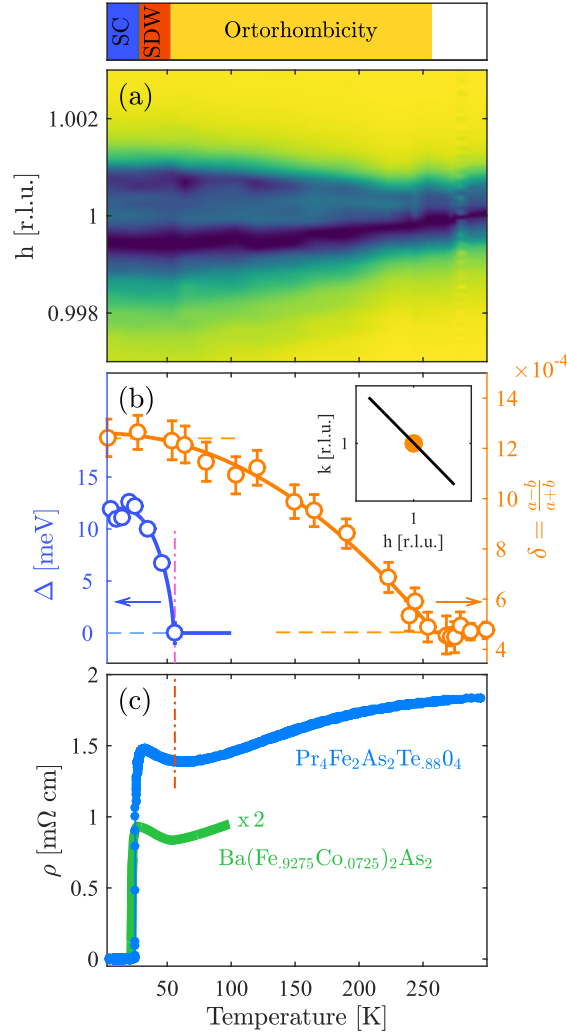


FIGURE A.2: (a) Diffraction intensity displayed in false color scale along the transverse direction through (1, 1, 0) Bragg reflection as a function of temperature. (b) Orthorhombicity $\delta = \frac{a-b}{a+b}$ of the (1, 1, 0) Bragg peak, as extracted from transverse scans, along with the spectral gap amplitude Δ extracted from ARPES studies. Solid line are guides to the eye only. (c) Resistivity curves of $\text{Pr}_4\text{Fe}_2\text{As}_2\text{Te}_{0.88}\text{O}_4$ and $\text{Ba}(\text{Fe}_{0.9275}\text{Co}_{0.0725})_2\text{As}_2$ adapted from Refs. [158, 162]

both along the longitudinal 2θ [Fig. A.1(b)] and transverse ω [Fig. A.1(c)] scans. This favors towards the $Fmmm$ structure [Fig. A.1(f) bottom], which should present a single peak along the longitudinal and three peaks along the transverse scans on the (4, 0, 0) Bragg peak. On the other hand, a splitting is observed, once again, along both directions [see Fig. A.1(d,e)]. As a conclusion, both the $Immm$ and $Fmmm$ symmetries are excluded, evidencing multiple symmetry breaking for the PFATO compound.

To track the orthorhombicity, as a function of temperature, transverse scans were taken on the (1, 1, 0) Bragg peak. These data are presented in Fig. A.2(a), where a false-color plot represents the intensity of the signal. To analyse the data, three Lorentzian functionalities were used. In addition the intensity and width of each peak, the distance

between the outer peaks, with respect to the central one, has been kept equal and used as a fit parameter. The splitting $\Delta\omega$ of these outer peaks is directly related to the orthorhombicity [163]:

$$\delta = \frac{a-b}{a+b} = \frac{\tan \frac{90+\Delta\omega}{2} - 1}{\tan \frac{90+\Delta\omega}{2} + 1}. \quad (\text{A.1})$$

In Fig. A.2(b), δ is presented as a function of temperature. We can observe that the orthorhombicity decreases gradually as a function of temperature from ~ 50 K to $T_s \sim 250$ K. Notably, for $T > T_s$, δ seems to have reached a saturation even though the peak still presents signs of orthorhombicity up to 300 K [see Fig. A.2(a)]. On the other hand, at low temperatures ($T < 50$ K), δ has no significant variation. Interestingly, this temperature coincides with the temperature T_g at which a band gap Δ (at high-symmetry M point) closes, as revealed by ARPES studies [see Fig. A.2(b)]. This band gap cannot be related to superconductivity, as the T_c of PFATO is $\sim 0.5 * T_g$.

In order to understand the nature of a gap opening at T_g , in Fig. A.2(c) we present the resistivity curves for PFATO and for the 122 system $\text{BaFe}_{2-x}\text{Co}_x\text{As}_2$. As can be seen, the data are similar for the two compounds except a scaling factor. This latter can be explained by the higher concentration of defects in PFATO crystal, which is in part due to the intercalated Te ions. At about 50 K, both systems present an upturn of the resistivity curves [Fig. A.2(c)]. For $\text{BaFe}_{2-x}\text{Co}_x\text{As}_2$, this is explained with the well established SDW in the system [164]. We thus argue that also in PFATO the anomaly in resistivity and an opening of a band gap at T_g might be a result of a presence of a SDW phase. In order to confirm this, experimental evidence of a spin order in this system would be of main importance.

Bibliography

- [1] D. J. Scalapino, Rev. Mod. Phys. **84**, 1383 (2012).
- [2] M. Lang and J. Müller, “Organic Superconductors,” in The Physics of Superconductors (Springer Berlin Heidelberg, 2004) p. 453–554.
- [3] P. A. Lee, N. Nagaosa, and X.-G. Wen, Rev. Mod. Phys. **78**, 17 (2006).
- [4] C. Pfeiderer, Rev. Mod. Phys. **81**, 1551 (2009).
- [5] G. R. Stewart, Rev. Mod. Phys. **83**, 1589 (2011).
- [6] Cao Yuan, Fatemi Valla, Fang Shiang, Watanabe Kenji, Taniguchi Takashi, Kaxiras Efthimios, and Jarillo-Herrero Pablo, Nature **556**, 43 (2018).
- [7] Manzeli Sajedeh, Ovchinnikov Dmitry, Pasquier Diego, Yazyev Oleg V., and Kis Andras, Nature Reviews Materials **2**, 17033 (2017).
- [8] A. Pulkin and O. V. Yazyev, Phys. Rev. B **93**, 041419 (2016).
- [9] Sipos B., Kusmartseva A. F., Akrap A., Berger H., Forró L., and Tutiš E., Nature Materials **7**, 960 (2008).
- [10] S. Pyon, K. Kudo, and M. Nohara, Journal of the Physical Society of Japan **81**, 053701 (2012).
- [11] J. J. Yang, Y. J. Choi, Y. S. Oh, A. Hogan, Y. Horibe, K. Kim, B. I. Min, and S.-W. Cheong, Phys. Rev. Lett. **108**, 116402 (2012).
- [12] Xi Xiaoxiang, Wang Zefang, Zhao Weiwei, Park Ju-Hyun, Law Kam Tuen, Berger Helmuth, Forró László, Shan Jie, and Mak Kin Fai, Nature Physics **12**, 139 (2015).
- [13] K. Momma and F. Izumi, Journal of Applied Crystallography **44**, 1272–1276 (2011).
- [14] S. Nandi, M. G. Kim, A. Kreyssig, R. M. Fernandes, D. K. Pratt, A. Thaler, N. Ni, S. L. Bud’ko, P. C. Canfield, J. Schmalian, R. J. McQueeney, and A. I. Goldman, Phys. Rev. Lett. **104**, 057006 (2010).

- [15] Shimizu Katsuya, Kimura Tomohiro, Furomoto Shigeyuki, Takeda Keiki, Kontani Kazuyoshi, Onuki Yoshichika, and Amaya Kiichi, *Nature* **412**, 316 (2001).
- [16] H. Okada, K. Igawa, H. Takahashi, Y. Kamihara, M. Hirano, H. Hosono, K. Matsumabayashi, and Y. Uwatoko, *Journal of the Physical Society of Japan* **77**, 113712 (2008).
- [17] A. S. Sefat, R. Jin, M. A. McGuire, B. C. Sales, D. J. Singh, and D. Mandrus, *Phys. Rev. Lett.* **101**, 117004 (2008).
- [18] J. Guo, S. Jin, G. Wang, S. Wang, K. Zhu, T. Zhou, M. He, and X. Chen, *Phys. Rev. B* **82**, 180520 (2010).
- [19] X. Wang, Q. Liu, Y. Lv, W. Gao, L. Yang, R. Yu, F. Li, and C. Jin, *Solid State Communications* **148**, 538–540 (2008).
- [20] F.-C. Hsu, J.-Y. Luo, K.-W. Yeh, T.-K. Chen, T.-W. Huang, P. M. Wu, Y.-C. Lee, Y.-L. Huang, Y.-Y. Chu, D.-C. Yan, and M.-K. Wu, *Proceedings of the National Academy of Sciences* **105**, 14262–14264 (2008).
- [21] X. Zhu, F. Han, G. Mu, P. Cheng, B. Shen, B. Zeng, and H.-H. Wen, *Phys. Rev. B* **79**, 220512 (2009).
- [22] S. Margadonna, Y. Takabayashi, Y. Ohishi, Y. Mizuguchi, Y. Takano, T. Kagayama, T. Nakagawa, M. Takata, and K. Prassides, *Phys. Rev. B* **80**, 064506 (2009).
- [23] Takahashi Hiroki, Igawa Kazumi, Arii Kazunobu, Kamihara Yoichi, Hirano Masahiro, and Hosono Hideo, *Nature* **453**, 376 (2008).
- [24] W. Qing-Yan, L. Zhi, Z. Wen-Hao, Z. Zuo-Cheng, Z. Jin-Song, L. Wei, D. Hao, O. Yun-Bo, D. Peng, C. Kai, W. Jing, S. Can-Li, H. Ke, J. Jin-Feng, J. Shuai-Hua, W. Ya-Yu, W. Li-Li, C. Xi, M. Xu-Cun, and X. Qi-Kun, *Chinese Physics Letters* **29**, 037402 (2012).
- [25] Ge Jian-Feng, Liu Zhi-Long, Liu Canhua, Gao Chun-Lei, Qian Dong, Xue Qi-Kun, Liu Ying, and Jia Jin-Feng, *Nature Materials* **14**, 285 (2014).
- [26] Chen X. H., Wu T., Wu G., Liu R. H., Chen H., and Fang D. F., *Nature* **453**, 761 (2008).
- [27] S. Wang, J. Zhang, J. Yan, X.-J. Chen, V. Struzhkin, W. Tabis, N. Barišić, M. K. Chan, C. Dorow, X. Zhao, M. Greven, W. L. Mao, and T. Geballe, *Phys. Rev. B* **89**, 024515 (2014).
- [28] H. Sato and M. Naito, *Physica C: Superconductivity* **274**, 221–226 (1997).

- [29] K. Miyazawa, K. Kihou, P. M. Shirage, C.-H. Lee, H. Kito, H. Eisaki, and A. Iyo, *Journal of the Physical Society of Japan* **78**, 034712 (2009).
- [30] C.-H. Lee, A. Iyo, H. Eisaki, H. Kito, M. Teresa Fernandez-Diaz, T. Ito, K. Kihou, H. Matsuhata, M. Braden, and K. Yamada, *Journal of the Physical Society of Japan* **77**, 083704 (2008).
- [31] T. Imai, K. Ahilan, F. L. Ning, T. M. McQueen, and R. J. Cava, *Phys. Rev. Lett.* **102**, 177005 (2009).
- [32] Kothapalli K., Böhmer A. E., Jayasekara W. T., Ueland B. G., Das P., Sapkota A., Taufour V., Xiao Y., Alp E., Bud'ko S. L., Canfield P. C., Kreyssig A., and Goldman A. I., *Nature Communications* **7**, 12728 (2016).
- [33] J. M. Tranquada, *AIP Conference Proceedings* **1550**, 114–187 (2013).
- [34] M. D. Lumsden, A. D. Christianson, D. Parshall, M. B. Stone, S. E. Nagler, G. J. MacDougall, H. A. Mook, K. Lokshin, T. Egami, D. L. Abernathy, E. A. Goremychkin, R. Osborn, M. A. McGuire, A. S. Sefat, R. Jin, B. C. Sales, and D. Mandrus, *Phys. Rev. Lett.* **102**, 107005 (2009).
- [35] N. B. Christensen, D. F. McMorrow, H. M. Rønnow, B. Lake, S. M. Hayden, G. Aeppli, T. G. Perring, M. Mangorkontong, M. Nohara, and H. Takagi, *Phys. Rev. Lett.* **93**, 147002 (2004).
- [36] T. Yoshida, X. J. Zhou, K. Tanaka, W. L. Yang, Z. Hussain, Z.-X. Shen, A. Fujimori, S. Sahrakorpi, M. Lindroos, R. S. Markiewicz, A. Bansil, S. Komiya, Y. Ando, H. Eisaki, T. Kakeshita, and S. Uchida, *Phys. Rev. B* **74**, 224510 (2006).
- [37] C. C. Tsuei, J. R. Kirtley, C. C. Chi, L. S. Yu-Jahnes, A. Gupta, T. Shaw, J. Z. Sun, and M. B. Ketchen, *Phys. Rev. Lett.* **73**, 593 (1994).
- [38] Hashimoto Makoto, Vishik Inna M., He Rui-Hua, Devereaux Thomas P., and Shen Zhi-Xun, *Nature Physics* **10**, 483 (2014).
- [39] Y. Yanagi, Y. Yamakawa, and Y. Ōno, *Phys. Rev. B* **81**, 054518 (2010).
- [40] H. Kontani and S. Onari, *Phys. Rev. Lett.* **104**, 157001 (2010).
- [41] I. I. Mazin, D. J. Singh, M. D. Johannes, and M. H. Du, *Phys. Rev. Lett.* **101**, 057003 (2008).
- [42] H. Kontani, T. Saito, and S. Onari, *Phys. Rev. B* **84**, 024528 (2011).

- [43] Christianson A. D., Goremychkin E. A., Osborn R., Rosenkranz S., Lumsden M. D., Malliakas C. D., Todorov I. S., Claus H., Chung D. Y., Kanatzidis M. G., Bewley R. I., and Guidi T., *Nature* **456**, 930 (2008).
- [44] Tranquada J. M., Sternlieb B. J., Axe J. D., Nakamura Y., and Uchida S., *Nature* **375**, 561 (1995).
- [45] T. Ido, K. Magoshi, H. Eisaki, and S. Uchida, *Phys. Rev. B* **44**, 12094 (1991).
- [46] B. O. Wells, Y. S. Lee, M. A. Kastner, R. J. Christianson, R. J. Birgeneau, K. Yamada, Y. Endoh, and G. Shirane, *Science* **277**, 1067–1071 (1997).
- [47] J. M. Tranquada, Y. Kong, J. E. Lorenzo, D. J. Buttrey, D. E. Rice, and V. Sachan, *Phys. Rev. B* **50**, 6340 (1994).
- [48] P. Wochner, J. M. Tranquada, D. J. Buttrey, and V. Sachan, *Phys. Rev. B* **57**, 1066 (1998).
- [49] R. Kajimoto, K. Ishizaka, H. Yoshizawa, and Y. Tokura, *Phys. Rev. B* **67**, 014511 (2003).
- [50] J. Zaanen, G. A. Sawatzky, and J. W. Allen, *Phys. Rev. Lett.* **55**, 418 (1985).
- [51] M. Imada, A. Fujimori, and Y. Tokura, *Rev. Mod. Phys.* **70**, 1039 (1998).
- [52] E. Gati, M. Garst, R. S. Manna, U. Tutsch, B. Wolf, L. Bartosch, H. Schubert, T. Sasaki, J. A. Schlueter, and M. Lang, *Science Advances* **2**, e1601646 (2016).
- [53] S. Friedemann, H. Chang, M. B. Gamza, P. Reiss, X. Chen, P. Alireza, W. A. Coniglio, D. Graf, S. Tozer, and F. M. Grosche, *Scientific Reports* **6**, 25335 EP (2016).
- [54] E. Wigner and H. B. Huntington, *The Journal of Chemical Physics* **3**, 764–770 (1935).
- [55] Drozdov A. P., Eremets M. I., Troyan I. A., Ksenofontov V., and Shylin S. I., *Nature* **525**, 73 (2015).
- [56] A. P. Drozdov, V. S. Minkov, S. P. Besedin, P. P. Kong, M. A. Kuzovnikov, D. A. Knyazev, and M. I. Eremets, *ArXiv e-prints* (2018).
- [57] M. Somayazulu, M. Ahart, A. K. Mishra, Z. M. Geballe, M. Baldini, Y. Meng, V. V. Struzhkin, and R. J. Hemley, *ArXiv e-prints* (2018).
- [58] B. Kim, P. Liu, J. M. Tomczak, and C. Franchini, *Phys. Rev. B* **98**, 075130 (2018).
- [59] J. M. Tomczak, *Journal of Physics: Condensed Matter* **30**, 183001 (2018).

- [60] M. v. Zimmermann, R. Nowak, G. D. Gu, C. Mennerich, H.-H. Klauss, and M. Hücker, *Review of Scientific Instruments* **79**, 033906 (2008).
- [61] M. Hücker, M. v. Zimmermann, M. Debessai, J. S. Schilling, J. M. Tranquada, and G. D. Gu, *Phys. Rev. Lett.* **104**, 057004 (2010).
- [62] R. Bouchard, D. Hupfeld, T. Lippmann, J. Neufeind, H.-B. Neumann, H. F. Poulsen, U. Rütt, T. Schmidt, J. R. Schneider, J. Süssenbach, and M. von Zimmermann, *Journal of Synchrotron Radiation* **5**, 90 (1998).
- [63] V. N. Strocov, T. Schmitt, U. Flechsig, T. Schmidt, A. Imhof, Q. Chen, J. Raabe, R. Betemps, D. Zimoch, J. Krempasky, X. Wang, M. P. A. Grioni, and L. Patthey, *J. Synchrotron Radiat.* **17**, 631 (2010).
- [64] P. Willmott, *An Introduction to Synchrotron Radiation: Techniques and Applications* (Wiley, 2011).
- [65] Peng Y. Y., Fumagalli R., Ding Y., Minola M., Caprara S., Betto D., Bluschke M., De Luca G. M., Kummer K., Lefrançois E., Salluzzo M., Suzuki H., Le Tacon M., Zhou X. J., Brookes N. B., Keimer B., Braicovich L., Grilli M., and Ghiringhelli G., *Nature Materials* **17**, 697–702 (2018).
- [66] Tranquada J. M., Woo H., Perring T. G., Goka H., Gu G. D., Xu G., Fujita M., and Yamada K., *Nature* **429**, 534 (2004).
- [67] N. Brookes, F. Yakhov-Harris, K. Kummer, A. Fondacaro, J. Cezar, D. Betto, E. Velez-Fort, A. Amorese, G. Ghiringhelli, L. Braicovich, R. Barrett, G. Berruyer, F. Cianciosi, L. Eybert, P. Marion, P. van der Linden, and L. Zhang, *Nuclear Instruments and Methods in Physics Research Section A: Accelerators, Spectrometers, Detectors and Associated Equipment* **903**, 175–192 (2018).
- [68] G. Ghiringhelli, A. Piazzalunga, C. Dallera, G. Trezzi, L. Braicovich, T. Schmitt, V. N. Strocov, R. Betemps, L. Patthey, X. Wang, and M. Grioni, *Review of Scientific Instruments* **77**, 113108 (2006).
- [69] F. Marschall, D. McNally, V. A. Guzenko, B. Rösner, M. Dantz, X. Lu, L. Nue, V. Strocov, T. Schmitt, and C. David, *Opt. Express* **25**, 15624 (2017).
- [70] K. Ichikawa, K. Jouda, S. Tanaka, K. Soda, M. Matsumoto, Y. Taguchi, T. Katsumi, O. Aita, H. Maezawa, Y. Azuma, and H. Kitazawa, *Journal of Electron Spectroscopy and Related Phenomena* **78**, 183–186 (1996).
- [71] L.-C. Duda, J. Nordgren, G. Dräger, S. Bocharov, and T. Kirchner, *Journal of Electron Spectroscopy and Related Phenomena* **110-111**, 275–285 (2000), soft X Ray Emission Spectroscopy.

- [72] G. Ghiringhelli, N. B. Brookes, E. Annese, H. Berger, C. Dallera, M. Grioni, L. Perfetti, A. Tagliaferri, and L. Braicovich, *Phys. Rev. Lett.* **92**, 117406 (2004).
- [73] L. Braicovich, L. J. P. Ament, V. Bisogni, F. Forte, C. Aruta, G. Balestrino, N. B. Brookes, G. M. De Luca, P. G. Medaglia, F. M. Granozio, M. Radovic, M. Salluzzo, J. van den Brink, and G. Ghiringhelli, *Phys. Rev. Lett.* **102**, 167401 (2009).
- [74] J. Schlappa, T. Schmitt, F. Vernay, V. N. Strocov, V. Ilakovac, B. Thielemann, H. M. Rønnow, S. Vanishri, A. Piazzalunga, X. Wang, L. Braicovich, G. Ghiringhelli, C. Marin, J. Mesot, B. Delley, and L. Patthey, *Phys. Rev. Lett.* **103**, 047401 (2009).
- [75] L. J. P. Ament, M. van Veenendaal, T. P. Devereaux, J. P. Hill, and J. van den Brink, *Rev. Mod. Phys.* **83**, 705 (2011).
- [76] M. M. Sala, V. Bisogni, C. Aruta, G. Balestrino, H. Berger, N. B. Brookes, G. M. de Luca, D. D. Castro, M. Grioni, M. Guarise, P. G. Medaglia, F. M. Granozio, M. Minola, P. Perna, M. Radovic, M. Salluzzo, T. Schmitt, K. J. Zhou, L. Braicovich, and G. Ghiringhelli, *New Journal of Physics* **13**, 043026 (2011).
- [77] M. L. Tacon, G. Ghiringhelli, J. Chaloupka, M. M. Sala, V. Hinkov, M. W. Haverkort, M. Minola, M. Bakr, K. J. Zhou, S. Blanco-Canosa, C. Monney, Y. T. Song, G. L. Sun, C. T. Lin, G. M. D. Luca, M. Salluzzo, G. Khaliullin, T. Schmitt, L. Braicovich, and B. Keimer, *Nat. Phys.* **7**, 725 (2011).
- [78] C. Monney, T. Schmitt, C. E. Matt, J. Mesot, V. N. Strocov, O. J. Lipscombe, S. M. Hayden, and J. Chang, *Phys. Rev. B* **93**, 075103 (2016).
- [79] J. Lamsal and W. Montfrooij, *Phys. Rev. B* **93**, 214513 (2016).
- [80] L. Braicovich, J. van den Brink, V. Bisogni, M. M. Sala, L. J. P. Ament, N. B. Brookes, G. M. De Luca, M. Salluzzo, T. Schmitt, V. N. Strocov, and G. Ghiringhelli, *Phys. Rev. Lett.* **104**, 077002 (2010).
- [81] Forgan E. M., Blackburn E., Holmes A. T., Briffa A. K. R., Chang J., Bouchenoire L., Brown S. D., Liang Ruixing, Bonn D., Hardy W. N., Christensen N. B., Zimmermann M. V., Hücker M., and Hayden S. M., *Nature Communications* **6**, 10064 (2015).
- [82] R. Coldea, S. M. Hayden, G. Aeppli, T. G. Perring, C. D. Frost, T. E. Mason, S.-W. Cheong, and Z. Fisk, *Phys. Rev. Lett.* **86**, 5377 (2001).
- [83] N. S. Headings, S. M. Hayden, R. Coldea, and T. G. Perring, *Phys. Rev. Lett.* **105**, 247001 (2010).

- [84] J.-Y. P. Delannoy, M. J. P. Gingras, P. C. W. Holdsworth, and A.-M. S. Tremblay, *Phys. Rev. B* **79**, 235130 (2009).
- [85] B. Dalla Piazza, M. Mourigal, M. Guarise, H. Berger, T. Schmitt, K. J. Zhou, M. Grioni, and H. M. Rønnow, *Phys. Rev. B* **85**, 100508 (2012).
- [86] Tranquada J. M., Sternlieb B. J., Axe J. D., Nakamura Y., and Uchida S., *Nature* **375**, 561 (1995).
- [87] Chang J., Blackburn E., Holmes A. T., Christensen N. B., Larsen J., Mesot J., Liang Ruixing, Bonn D. A., Hardy W. N., Watenphul A., Zimmermann M. v., Forgan E. M., and Hayden S. M., *Nature Physics* **8**, 871 (2012).
- [88] Wu Tao, Mayaffre Hadrien, Krämer Steffen, Horvatić Mladen, Berthier Claude, Hardy W. N., Liang Ruixing, Bonn D. A., and Julien Marc-Henri, *Nature* **477**, 191 (2011).
- [89] S. Gerber, H. Jang, H. Nojiri, S. Matsuzawa, H. Yasumura, D. A. Bonn, R. Liang, W. N. Hardy, Z. Islam, A. Mehta, S. Song, M. Sikorski, D. Stefanescu, Y. Feng, S. A. Kivelson, T. P. Devereaux, Z.-X. Shen, C.-C. Kao, W.-S. Lee, D. Zhu, and J.-S. Lee, *Science* **350**, 949 (2015).
- [90] Chang J., Blackburn E., Ivashko O., Holmes A. T., Christensen N. B., Hücker M., Liang Ruixing, Bonn D. A., Hardy W. N., Rütt U., Zimmermann M. v., Forgan E. M., and Hayden S M, *Nature Communications* **7**, 11494 (2016).
- [91] G. L. Pascut, K. Haule, M. J. Gutmann, S. A. Barnett, A. Bombardi, S. Artyukhin, T. Birol, D. Vanderbilt, J. J. Yang, S.-W. Cheong, and V. Kiryukhin, *Phys. Rev. Lett.* **112**, 086402 (2014).
- [92] M. J. Eom, K. Kim, Y. J. Jo, J. J. Yang, E. S. Choi, B. I. Min, J.-H. Park, S.-W. Cheong, and J. S. Kim, *Phys. Rev. Lett.* **113**, 266406 (2014).
- [93] C. Chen, J. Kim, Y. Yang, G. Cao, R. Jin, and E. W. Plummer, *Phys. Rev. B* **95**, 094118 (2017).
- [94] D. Ootsuki, S. Pyon, K. Kudo, M. Nohara, M. Horio, T. Yoshida, A. Fujimori, M. Arita, H. Anzai, H. Namatame, M. Taniguchi, N. L. Saini, and T. Mizokawa, *Journal of the Physical Society of Japan* **82**, 093704 (2013).
- [95] K. Kim, S. Kim, K.-T. Ko, H. Lee, J.-H. Park, J. J. Yang, S.-W. Cheong, and B. I. Min, *Phys. Rev. Lett.* **114**, 136401 (2015).
- [96] Fang A. F., Xu G., Dong T., Zheng P., and Wang N. L., *Scientific Reports* **3**, 1153 (2013).

- [97] M. Kamitani, M. S. Bahramy, R. Arita, S. Seki, T. Arima, Y. Tokura, and S. Ishiwata, *Phys. Rev. B* **87**, 180501 (2013).
- [98] S. Nagata, N. Kijima, S. Ikeda, N. Matsumoto, R. Endoh, S. Chikazawa, I. Shimon, and H. Nishihara, *Journal of Physics and Chemistry of Solids* **60**, 163 (1999).
- [99] Ko K.-T., Lee H.-H., Kim D.-H., Yang J.-J., Cheong S.-W., Eom M.J., Kim J.S., Gammag R., Kim K.-S., Kim H.-S., Kim T.-H., Yeom H.-W., Koo T.-Y., Kim H.-D., and Park J.-H., *Nature Communications* **6**, 7342 (2015).
- [100] N. Matsumoto, K. Taniguchi, R. Endoh, H. Takano, and S. Nagata, *Journal of Low Temperature Physics* **117**, 1129 (1999).
- [101] L. Li, T. F. Qi, L. S. Lin, X. X. Wu, X. T. Zhang, K. Butrouna, V. S. Cao, Y. H. Zhang, J. Hu, S. J. Yuan, P. Schlottmann, L. E. De Long, and G. Cao, *Phys. Rev. B* **87**, 174510 (2013).
- [102] Q. Li, M. Hücker, G. D. Gu, A. M. Tsvelik, and J. M. Tranquada, *Phys. Rev. Lett.* **99**, 067001 (2007).
- [103] L. Benfatto, C. Castellani, and T. Giamarchi, *Phys. Rev. B* **80**, 214506 (2009).
- [104] G. L. Pascut, T. Birol, M. J. Gutmann, J. J. Yang, S.-W. Cheong, K. Haule, and V. Kiryukhin, *Phys. Rev. B* **90**, 195122 (2014).
- [105] T. Toriyama, M. Kobori, T. Konishi, Y. Ohta, K. Sugimoto, J. Kim, A. Fujiwara, S. Pyon, K. Kudo, and M. Nohara, *Journal of the Physical Society of Japan* **83**, 033701 (2014).
- [106] S. F. Blake, M. D. Watson, A. McCollam, S. Kasahara, R. D. Johnson, A. Narayanan, G. L. Pascut, K. Haule, V. Kiryukhin, T. Yamashita, D. Watanabe, T. Shibauchi, Y. Matsuda, and A. I. Coldea, *Phys. Rev. B* **91**, 121105 (2015).
- [107] D. van Delft and P. Kes, *Physics Today* **63**, 38–43 (2010).
- [108] J. G. Bednorz and K. A. Müller, *Zeitschrift für Physik B Condensed Matter* **64**, 189–193 (1986).
- [109] J. G. Bednorz and K. A. Müller, *Rev. Mod. Phys.* **60**, 585 (1988).
- [110] Schilling A., Cantoni M., Guo J. D., and Ott H. R., *Nature* **363**, 56 (1993).
- [111] “Heating up of Superconductors,” (2017), American Physical Society Collection.
- [112] J. Locquet and E. Williams, *Acta Physica Polonica A* **92**, 69–84 (1997).

- [113] L. P. Gor'kov and V. Z. Kresin, Rev. Mod. Phys. **90**, 011001 (2018).
- [114] E. Maxwell, Phys. Rev. **78**, 477 (1950).
- [115] C. A. Reynolds, B. Serin, W. H. Wright, and L. B. Nesbitt, Phys. Rev. **78**, 487 (1950).
- [116] R. J. Cava, R. B. van Dover, B. Batlogg, and E. A. Rietman, Phys. Rev. Lett. **58**, 408 (1987).
- [117] A. Damascelli, Z. Hussain, and Z.-X. Shen, Rev. Mod. Phys. **75**, 473 (2003).
- [118] P. J. Ray, "Master's thesis: Structural investigation of $\text{La}(2-x)\text{Sr}(x)\text{CuO}(4+y)$ - Following staging as a function of temperature," (2016).
- [119] J. M. Tarascon, L. H. Greene, W. R. Mckinnon, G. W. Hull, and T. H. Geballe, Science **235**, 1373 (1987).
- [120] P. G. Radaelli, D. G. Hinks, A. W. Mitchell, B. A. Hunter, J. L. Wagner, B. Dabrowski, K. G. Vandervoort, H. K. Viswanathan, and J. D. Jorgensen, Phys. Rev. B **49**, 4163 (1994).
- [121] M. Horio, K. Hauser, Y. Sassa, Z. Mingazheva, D. Sutter, K. Kramer, A. Cook, E. Nocerino, O. K. Forslund, O. Tjernberg, M. Kobayashi, A. Chikina, N. B. M. Schröter, J. A. Krieger, T. Schmitt, V. N. Strocov, S. Pyon, T. Takayama, H. Takagi, O. J. Lipscombe, S. M. Hayden, M. Ishikado, H. Eisaki, T. Neupert, M. Månsson, C. E. Matt, and J. Chang, Phys. Rev. Lett. **121**, 077004 (2018).
- [122] J. Wagner, P. Radaelli, D. Hinks, J. Jorgensen, J. Mitchell, B. Dabrowski, G. Knapp, and M. Beno, Physica C: Superconductivity **210**, 447–454 (1993).
- [123] S. Uchida, T. Ido, H. Takagi, T. Arima, Y. Tokura, and S. Tajima, Phys. Rev. B **43**, 7942 (1991).
- [124] Matt C. E., Sutter D., Cook A. M., Sassa Y., Månsson M., Tjernberg O., Das L., Horio M., Destraz D., Fatuzzo C. G., Hauser K., Shi M., Kobayashi M., Strocov V. N., Schmitt T., Dudin P., Hoesch M., Pyon S., Takayama T., Takagi H., Lipscombe O. J., Hayden S. M., Kurosawa T., Momono N., Oda M., Neupert T., and Chang J., Nature Communications **9**, 972 (2018).
- [125] M. Shi, A. Bendounan, E. Razzoli, S. Rosenkranz, M. R. Norman, J. C. Campuzano, J. Chang, M. Månsson, Y. Sassa, T. Claesson, O. Tjernberg, L. Patthey, N. Momono, M. Oda, M. Ido, S. Guerrero, C. Mudry, and J. Mesot, EPL (Europhysics Letters) **88**, 27008 (2009).

- [126] O. Cyr-Choinière, R. Daou, F. Laliberté, C. Collignon, S. Badoux, D. LeBoeuf, J. Chang, B. J. Ramshaw, D. A. Bonn, W. N. Hardy, R. Liang, J.-Q. Yan, J.-G. Cheng, J.-S. Zhou, J. B. Goodenough, S. Pyon, T. Takayama, H. Takagi, N. Doiron-Leyraud, and L. Taillefer, *Phys. Rev. B* **97**, 064502 (2018).
- [127] G. S. Boebinger, Y. Ando, A. Passner, T. Kimura, M. Okuya, J. Shimoyama, K. Kishio, K. Tamasaku, N. Ichikawa, and S. Uchida, *Phys. Rev. Lett.* **77**, 5417 (1996).
- [128] Y. Ando, S. Komiya, K. Segawa, S. Ono, and Y. Kurita, *Phys. Rev. Lett.* **93**, 267001 (2004).
- [129] M. R. Norman, D. Pines, and C. Kallin, *Advances in Physics* **54**, 715 (2005).
- [130] H. Sakakibara, H. Usui, K. Kuroki, R. Arita, and H. Aoki, *Phys. Rev. Lett.* **105**, 057003 (2010).
- [131] H. Sakakibara, H. Usui, K. Kuroki, R. Arita, and H. Aoki, *Phys. Rev. B* **85**, 064501 (2012).
- [132] W. Hanke, M. Kiesel, M. Aichhorn, S. Brehm, and E. Arrigoni, *The European Physical Journal Special Topics* **188**, 15–32 (2010).
- [133] D. J. Scalapino, *Science* **284**, 1282–1283 (1999).
- [134] P. Anderson, *Advances in Physics* **46**, 3–11 (1997).
- [135] M. Fujita, H. Hiraka, M. Matsuda, M. Matsuura, J. M. Tranquada, S. Wakimoto, G. Xu, and K. Yamada, *Journal of the Physical Society of Japan* **81**, 011007 (2012).
- [136] V. Thampy, M. P. M. Dean, N. B. Christensen, L. Steinke, Z. Islam, M. Oda, M. Ido, N. Momono, S. B. Wilkins, and J. P. Hill, *Phys. Rev. B* **90**, 100510 (2014).
- [137] T. P. Croft, C. Lester, M. S. Senn, A. Bombardi, and S. M. Hayden, *Phys. Rev. B* **89**, 224513 (2014).
- [138] M. Guarise, B. D. Piazza, H. Berger, E. Giannini, T. Schmitt, H. M. Rønnow, G. A. Sawatzky, J. van den Brink, D. Altenfeld, I. Eremin, and M. Grioni, *Nat Commun* **5**, 5760 (2014).
- [139] M. P. M. Dean, A. J. A. James, A. C. Walters, V. Bisogni, I. Jarrige, M. Hücker, E. Giannini, M. Fujita, J. Pelliciari, Y. B. Huang, R. M. Konik, T. Schmitt, and J. P. Hill, *Phys. Rev. B* **90**, 220506 (2014).

- [140] C. G. Fatuzzo, Y. Sassa, M. Månsson, S. Pailhès, O. J. Lipscombe, S. M. Hayden, L. Patthey, M. Shi, M. Grioni, H. M. Rønnow, J. Mesot, O. Tjernberg, and J. Chang, *Phys. Rev. B* **89**, 205104 (2014).
- [141] J. Chang, M. Månsson, S. Pailhès, T. Claesson, O. J. Lipscombe, S. M. Hayden, L. Patthey, O. Tjernberg, and J. Mesot, *Nature Communications* **4**, 2559 (2013).
- [142] E. Pavarini, I. Dasgupta, T. Saha-Dasgupta, O. Jepsen, and O. K. Andersen, *Phys. Rev. Lett.* **87**, 047003 (2001).
- [143] Peng Y. Y., Dellea G., Minola M., Conni M., Amorese A., Di Castro D., De Luca G. M., Kummer K., Salluzzo M., Sun X., Zhou X. J., Balestrino G., Le Tacon M., Keimer B., Braicovich L., Brookes N. B., and Ghiringhelli G., *Nature Physics* **13**, 1201 (2017).
- [144] H. Sakakibara, K. Suzuki, H. Usui, K. Kuroki, R. Arita, D. Scalapino, and H. Aoki, *Physics Procedia* **45**, 13–16 (2013), proceedings of the 25th International Symposium on Superconductivity (ISS2012).
- [145] B. Keimer, A. Aharony, A. Auerbach, R. J. Birgeneau, A. Cassanho, Y. Endoh, R. W. Erwin, M. A. Kastner, and G. Shirane, *Phys. Rev. B* **45**, 7430 (1992).
- [146] R. Ofer, G. Bazalitsky, A. Kanigel, A. Keren, A. Auerbach, J. S. Lord, and A. Amato, *Phys. Rev. B* **74**, 220508 (2006).
- [147] Curro N. J., Caldwell T., Bauer E. D., Morales L. A., Graf M. J., Bang Y., Balatsky A. V., Thompson J. D., and Sarrao J. L., *Nature* **434**, 622 (2005).
- [148] L. Vasylechko, L. Akselrud, W. Morgenroth, U. Bismayer, A. Matkovskii, and D. Savytskii, *Journal of Alloys and Compounds* **297**, 46–52 (2000).
- [149] M. Vekić and S. R. White, *Phys. Rev. B* **47**, 1160 (1993).
- [150] J. M. Tomczak, T. Miyake, R. Sakuma, and F. Aryasetiawan, *Phys. Rev. B* **79**, 235133 (2009).
- [151] J. M. Tomczak, T. Miyake, and F. Aryasetiawan, *Phys. Rev. B* **81**, 115116 (2010).
- [152] D. Di Sante, A. Hausoel, P. Barone, J. M. Tomczak, G. Sangiovanni, and R. Thomale, *Phys. Rev. B* **96**, 121106 (2017).
- [153] P. Werner, R. Sakuma, F. Nilsson, and F. Aryasetiawan, *Phys. Rev. B* **91**, 125142 (2015).
- [154] J. P. Locquet, J. Perret, J. Fompeyrine, E. Machler, J. W. Seo, and G. Van Tendeloo, *Nature* **394**, 453 (1998).

- [155] H. Takagi, T. Ido, S. Ishibashi, M. Uota, S. Uchida, and Y. Tokura, Phys. Rev. B **40**, 2254 (1989).
- [156] D. S. Ellis, Y.-B. Huang, P. Olalde-Velasco, M. Dantz, J. Pelliciari, G. Drachuck, R. Ofer, G. Bazalitsky, J. Berger, T. Schmitt, and A. Keren, Phys. Rev. B **92**, 104507 (2015).
- [157] Fratino L., Sémon P., Sordi G., and Tremblay A.-M. S., Scientific Reports **6**, 22715 (2016).
- [158] S. Katrych, K. Rogacki, A. Pisoni, S. Bosma, S. Weyeneth, R. Gaal, N. D. Zhigadlo, J. Karpinski, and L. Forró, Phys. Rev. B **87**, 180508 (2013).
- [159] S. Katrych, A. Pisoni, S. Bosma, S. Weyeneth, N. D. Zhigadlo, R. Gaal, J. Karpinski, and L. Forró, Phys. Rev. B **89**, 024518 (2014).
- [160] C. Matt, O. Ivashko, M. Horio, D. Sutter, N. Dennler, J. Choi, J. Mesot, M. Shi, J. Chang, M. Hücker, S. Katrych, L. Forró, N. C. Plumb, M. v. Zimmermann, and T. K. Kim, *in preparation*.
- [161] Tonegawa S., Kasahara S., Fukuda T., Sugimoto K., Yasuda N., Tsuruhara Y., Watanabe D., Mizukami Y., Haga Y., Matsuda T. D., Yamamoto E., Onuki Y., Ikeda H., Matsuda Y., and Shibauchi T., Nature Communications **5**, 4188 (2014).
- [162] G. N. Tam, B. D. Faeth, J. S. Kim, and G. R. Stewart, Phys. Rev. B **88**, 134503 (2013).
- [163] F. Nitsche, T. Doert, and M. Ruck, Solid State Sciences **19**, 162–166 (2013).
- [164] F. Rullier-Albenque, D. Colson, A. Forget, and H. Alloul, Phys. Rev. Lett. **103**, 057001 (2009).

List of Publications

First authorship publications, on which this thesis is based:

1 – O. Ivashko, L. Yang, D. Destraz, E. Martino, Y. Chen, C. Y. Guo, H. Q. Yuan, A. Pisoni, P. Matus, S. Pyon, K. Kudo, M. Nohara, L. Forró, H. M. Rønnow, M. Hückler, M. v. Zimmermann, and J. Chang

“Charge-Stripe Order and Superconductivity in $\text{Ir}_{1-x}\text{Pt}_x\text{Te}_2$ ”

Scientific Reports **7**, 17157 (2017)

personal contribution: carried out the XRD experiments, analyzed the XRD data, prepared all the figures, leaded the preparation and submission of the manuscript

2 – O. Ivashko, N. E. Shaik, X. Lu, C. G. Fatuzzo, M. Dantz, P. G. Freeman, D. E. McNally, D. Destraz, N. B. Christensen, T. Kurosawa, N. Momono, M. Oda, C. E. Matt, C. Monney, H. M. Rønnow, T. Schmitt, and J. Chang

“Damped spin excitations in a doped cuprate superconductor with orbital hybridization”

Physical Review B **95**, 214508 (2017)

personal contribution: carried out the RIXS experiments, analyzed the RIXS data, prepared all the figures, leaded the preparation and submission of the manuscript

3 – O. Ivashko, M. Horio, W. Wan, N. B. Christensen, D. E. McNally, E. Paris, Y. Tseng, N. E. Shaik, H. M. Rønnow, H. I. Wei, C. Adamo, C. Lichtensteiger, M. Gibert, M. R. Beasley, K. M. Shen, J. M. Tomczak, T. Schmitt, J. Chang

“Engineering the Mott State of Cuprates for High-Temperature Superconductivity”

ArXiv e-prints, arXiv:1805.07173 (2018)

personal contribution: carried out the RIXS experiments, analyzed the RIXS data, prepared all the figures and leaded the preparation and submission of the manuscript

Publications during the Ph.D. period:

4 – L. Das, F. Forte, R. Fittipaldi, C. G. Fatuzzo, V. Granata, O. Ivashko, M. Horio, F. Schindler, M. Dantz, Yi Tseng, D. E. McNally, H. M. Rønnow, W. Wan, N. B. Christensen, J. Pelliciani, P. Olalde-Velasco, N. Kikugawa, T. Neupert, A. Vecchione, T. Schmitt, M. Cuoco, and J. Chang

“Spin-Orbital Excitations in Ca_2RuO_4 Revealed by Resonant Inelastic X-Ray Scattering”

Physical Review X **8**, 11048 (2018)

personal contribution: carried out the RIXS experiments, prepared the schematics in Fig.1 and actively participated in the preparation of the manuscript

5 – J. Chang, E. Blackburn, O. Ivashko, A. T. Holmes, N. B. Christensen, M. Hücker, Ruixing Liang, D. A. Bonn, W. N. Hardy, U. Rütt, M. v. Zimmermann, E. M. Forgan and S. M. Hayden

“Magnetic field controlled charge density wave coupling in underdoped $\text{YBa}_2\text{Cu}_3\text{O}_{6+x}$ ”

Nature Communications **7**, 11494 (2016)

personal contribution: carried out the XRD experiments and participated in the preparation of the manuscript

Publication related to the master thesis:

6 – A. Picone, M. Riva, A. Brambilla, D. Giannotti, O. Ivashko, G. Bussetti, M. Finazzi, F. Ciccacci, and L. Duò

“Atomic Scale Insights into the Early Stages of Metal Oxidation: A Scanning Tunneling Microscopy and Spectroscopy Study of Cobalt Oxidation”

The Journal of Physical Chemistry C **120**, 5233 (2016)

personal contribution: carried out the STM/S experiments, analyzed STM/S data and participated in the preparation of the manuscript

Publications in preparation:

7 – C.E. Matt, O. Ivashko, M. Horio, D. Sutter, N. Dennler, J. Choi, J. Mesot, M. Shi, J. Chang, M. Hücker, S. Katrych, L. Forró, N. C. Plumb, M. v. Zimmermann, and T. K. Kim

“Novel Electronic Pnictide Phenomenology found in Superconducting $\text{Pr}_4\text{Fe}_2\text{As}_2\text{Te}_{0.88}\text{O}_4$ ”

personal contribution: carried out the XRD experiments, analyzed XRD data and prepared two figures

8 – J. Choi, O. Ivashko, N. Dennler, M. Hücker, D. Aoki, S. Gerber, O. Gutowski, U. Rütt, M. Fischer, J. Strempfer, M. v. Zimmermann, and J. Chang

“Pressure-Induced Rotational Symmetry Breaking in URu₂Si₂”

personal contribution: carried out the XRD experiments and participated in the preparation of the manuscript

9 – J. Choi, E. Blackburn, O. Ivashko, Ruixing Liang, D. A. Bonn, W. N. Hardy, A. T. Holmes, N. B. Christensen, E. M. Forgan, O. Gutowski, U. Rütt, M. v. Zimmermann, S. M. Hayden, and J. Chang

“Three-Dimensional Competition between Superconductivity and Charge-Order in YBa₂Cu₃O_{6.67}”

personal contribution: carried out the XRD experiments and actively participated in the preparation of the manuscript

10 – F. A. Garcia, O. Ivashko, D. E. McNally, L. Das, M. M. Piva, P. G. Pagliuso, J. Chang, T. Schmitt and C. Monney

“Anisotropic magnetic excitations and incipient Néel order in Ba(Fe_{1-x}Mn_x)₂As₂”

personal contribution: carried out the RIXS experiments and actively participated in the preparation of the manuscript

Acknowledgements

I would like to express my very great appreciation to Prof. Johan Chang for the given opportunity and guidance during my PhD research.

I would also like to offer my special thanks to all the collaborators. In particular, I would like to thank Dr. Thorsten Schmitt for introducing me to the RIXS technique and for interesting discussions during the experiments. Many thanks to Dr. Martin von Zimmermann for teaching me on how to conduct XRD experiments and interpret correctly the obtained data. Special thanks go to all the staff at the ADRESS beamline in SLS and at the P07 beamline in PETRA III.

A special thank goes for all the group members (+ Alsu) for the great time spent together, in particular Claudia for her patience during the beginning of my studies, Denys and Christian for the funny stories and Lakshmi for that little Malayalam and craziness.

Finally, I would like to thank my family for their support during these many years of studies.

Oleh Ivashko

DATA OF BIRTH	March 18, 1989
COUNTRY OF ORIGIN	Ukraine
CONTACT INFORMATION	Winterthurerstrasse 190 Zürich, CH 8057 oleh.ivashko@physik.uzh.ch
EDUCATION	University of Zurich , Zurich, Switzerland Ph.D. in Condensed Matter Physics November 2018 Politecnico di Milano , Milan, Italy Master in Engineering Physics December 2014 Bachelor in Engineering Physics September 2012
CONFERENCES	ICM 2018 “International Conference on Magnetism”, San Francisco, USA CMPC 2017 “Bulk scattering in Condensed Matter Physics and Chemistry Workshop at DESY”, Hamburg, Germany CORPES 2017 “International workshop on strong correlations and angle-resolved photoemission spectroscopy”, Hiroshima, Japan MaNEP Workshop “Topological Quantum Phenomena”, Zurich, Switzerland VUVX 2016 “39 th International Conference on Vacuum Ultraviolet and X-ray Physics”, Zurich, Switzerland SNS 2016 “Spectroscopies in Novel Superconductors”, Stuttgart, Germany
SCHOOLS	Hercules Specialized Courses HSC18 “Neutrons and Synchrotron Radiation for Magnetism”, Grenoble, France PSI Summer School “Spectroscopy with Neutrons, Muons and Photons”, Zuz, Switzerland
EXPERIMENTAL TECHNIQUES	Hard X-Ray Diffraction (XRD) in Combination with 10 T Magnet and Pressure Cell Resonant Inelastic X-Ray Scattering (RIXS) Laue Diffraction Inelastic Neutron Scattering (INS) Scanning Tunneling Microscopy/Spectroscopy (STM/S)
LANGUAGES	Ukrainian (Native), Italian (Native), English (C2), Russian (B2), German (A1)